University of Padova

Department of Industrial Engineering

Master Thesis in Aerospace Engineering

Design of freeform optics based instruments for Solar System exploration

Supervisor

Prof. Giampiero Naletto

Master Candidate

Giorgia Milan

Matr. 2020213

Co-supervisor

Dr. Maurizio Pajola

Research Scientist at INAF

October 19, 2023

Ai miei cugini Amanda, Pietro e Matilde...
spero di ispirarvi come voi ispirate me.

Abstract (IT)

Le missioni spaziali verso i corpi planetari del nostro Sistema Solare hanno rivelato realtà singolari, complesse e dinamiche. Oltre ai ben familiari pianeti, le popolazioni dei Near Earth Asteroids e dei Corpi Minori sono di grande interesse per la ricerca moderna, poiché costituiscono i cosiddetti "mattoni primordiali" che tengono traccia delle condizioni fisico-chimiche dell' epoca di origine del Sistema Solare. Le osservazioni in remote sensing effettuate con imager multispettrali e spettrometri ad alta risoluzione possono contribuire in modo significativo alla conoscenza delle caratteristiche fisiche e delle proprietà dinamiche sia dei pianeti che dei Corpi Minori, e sono quindi fondamentali per fornire nuova luce sulla formazione e l'evoluzione del Sistema Solare.
A tal fine, in questo lavoro di tesi, sono stati analizzati due diversi strumenti ottici, il primo dei quali è una camera, basata su un telescopio Three-Mirror-Anastigmatic (TMA), con due diversi piani focali (VIS/IR), mentre il secondo è un sistema di stereo-imaging iperspettrale, sempre alimentato da un telescopio TMA. Entrambi gli strumenti sono stati studiati in precedenza; i layout esistenti sono serviti come punto di partenza per un miglioramento generale delle prestazioni dello strumento o per l'adeguamento a nuovi requisiti attraverso l'inclusione di superfici ottiche freeform negli specchi dei telescopi. Tali ottiche hanno fornito ulteriori gradi di libertà al progetto, consentendo la correzione delle principali aberrazioni limitanti. L'inclusione di queste superfici ha permesso di soddisfare i requisiti imposti per entrambi gli strumenti, ottenendo buone prestazioni. Il design finale della camera è adattabile a missioni spaziali verso corpi asteroidali o verso i pianeti esterni e le loro lune, mentre il sistema di stereo-imaging verrà proposto per una missione di mapping lunare.

Abstract (EN)

Space missions to the planetary bodies of our Solar System have revealed unique, complex and dynamic worlds. In addition to the well-known planets, the populations of Near Earth Asteroids and Minor Bodies are also of great interest to modern research, as they constitute primitive- leftover building blocks of the Solar System formation process, and can provide clues to the chemical mixture from which the planets formed. Remote sensing observations performed by multi-spectral imagers and high-resolution imaging spectrometers on board of spacecrafts may contribute significantly to our knowledge of the physical characteristics and dynamical properties of both Planets and Minor Bodies, and thus are fundamental to provide new insights into the formation and evolution of the Solar System.
To this end, two different optical instruments have been analyzed, the first being a camera, based on a Three-Mirror Anastigmatic (TMA) telescope, with two different focal planes (VIS/IR), and the second a hyperspectral stereo imaging system, still fed by a TMA telescope. Both instruments have been previously investigated, and the existing layouts served as a starting point for a novel improvement through the inclusion of freeform optical surfaces within the telescopes, which provided additional degrees of freedom to the design, allowing correction of the major limiting aberrations.
The inclusion of these surfaces enabled to meet the requirements for both the instruments, while still achieving a good performance. The resulting design for the camera is suitable for space missions to asteroidal bodies or to the Outer Planets and their moons, while the stereo-imaging system will be proposed for a lunar mapping space mission.

Contents

Listing of figures

Listing of tables

Listing of acronyms

DTM . . . . . Digital Terrain Model

ECAS . . . . . Eight-Color Asteroid Survey

EFM . . . . . Entrance Folding Mirror

FFD . . . . . Full Field Display

FM . . . . . Folding Mirror

FoV . . . . . Field of View

HYPSOS . . . . . HYPerspectral Stereo Observing System

IMC . . . . . Intermediate-source Mars-Crossing region

MB . . . . . Main Belt

NAT . . . . . Nodal Aberration Theory

NEO . . . . . Near Earth Object

NEA . . . . . Near Earth Asteroid

NEC . . . . . Near Earth Comet

PSF . . . . . Point Spread Function

RMS . . . . . Root Mean Square

SDTM . . . . . Spectral Digital Terrain Model

SPP . . . . . Schmidt-Pechan Prism

TMA . . . . . Three Mirror Anastigmat

VIS/IR . . . . . Visible and InfraRed

1

Introduction

Mankind's interest in the heavens is universal and enduring. Humans are driven to explore the unknown, to discover new worlds and to push the boundaries of our scientific and technological capabilities. The intangible desire to explore and challenge the limits of what we know and where we have been has benefited our society for centuries. Space missions to the planetary bodies of our Solar System in recent decades have revealed unique, complex and dynamic worlds. In addition to the major planets, the population of Minor Bodies is also of great interest to modern research. These bodies, which include asteroids, comets nuclei and other small objects, are thought to be primitive, leftover building blocks from the Solar System's formation process. Moreover, the pristine nature of most of these objects, with physical properties that have changed only minimally since the epoch of their formation, makes them fundamental to providing new insights into the formation and evolution of the Solar System, and thus to answering fundamental questions about our place in the Universe [13, 14].

Remote sensing from orbiter missions has helped to delineate surface topography and

identify specific morphological features, as well as to map the composition and derive reliable age estimates for various planetary surfaces. In particular, observations made by multispectral imagers and high-resolution imaging spectrometers on board of spacecrafts have significantly contributed to our current understanding of the geological, physical and chemical processes that have led to the divergent evolutionary paths taken by different planetary objects and small Solar System bodies.

In this thesis, two different optical systems, a VIS/IR camera and an imaging spectrometer, have been studied and improved from an existing design. Both instruments were designed to be suitable for different fly-by and/or rendez-vous space missions, either on a planet or on an asteroidal body. The first instrument that has been analyzed is the VIS/IR camera. The initial layout is derived from VICESS (Visible and Infrared Camera for the Exploration of the Solar System), a design discussed in a previous work of thesis [15]. This camera consists of a Three Mirror Anastigmat (TMA) telescope feeding two different focal planes. This design has been conceived to map the surface of an asteroid, or another Minor Body of the Solar System to determine its shape and volume, as well as the local topography and surface geomorphology, and to provide information on the composition via surface reflectance features, thanks to multispectral imaging.

The novelty of this work of thesis is the introduction of freeform mirrors into the existing layout, with the ultimate aim of improving the overall performance of the instrument. A freeform surface might be characterised by many surface descriptors, but for the present work Zernike polynomials have emerged as the most suitable ones, as they are directly correlated with wavefront aberrations. Following the principles of the Nodal Aberration Theory (NAT) applied to freeform optics ([10, 9]), an attempt has been made to introduce the appropriate coefficients as optimisation variables in the OpticStudio Zemax ray-tracing software, allowing the correction of the main aberrations that limit the system performance without making the system unnecessarily complicated. To this end, the Full Field Display tool (FFD) built into the software has been essential in selecting the design variables.
This approach was initially implemented on the original TMA geometry. The optimization

outcome was a system with geometrical aberrations smaller than the diffraction limit, showing the potential of this kind of optics. This new advantage has then been utilised to increase the system's focal length and entrance pupil diameter. This enables a greater throughput and observation of intrinsically darker objects from relatively large distances (e.g a flyby with an Outer Planet), while maintaining a diffraction-limited system relatively compact.

The analysis of the second, more complex optical instrument, which was previously investigated, has been conducted in order to introduce freeform optics to meet the assigned requirements for a lunar mapping mission, while achieving a competitive performance. The starting point was the layout of the HYPSOS (HYPerspectral Stereo Observing System [5]) instrument, a push-broom stereo camera coupled with an imaging spectrograph, allowing simultaneous acquisition of spatial and spectral data of the observed feature. While adapting the system to new constraints, significant focus was placed on streamlining the design while retaining the fundamental concept. In this case, introducing the freeform overlay into the telescope mirrors has been a challenging task, as the system was inherently more complex than the previous one. As a result a different, more practical approach has been followed, introducing the Zernike coefficients without the crucial aid from the FFD, but still having in mind to keep their number minimal. The optimized system is more straightforward and compact than the original one and delivered optical performance which satisfies the scientific requirements.

2

Solar System exploration

Exploration of planetary bodies in the Solar System is essential to understand their formation and decipher evolutionary processes leading to their current physical state. For distant and largely inaccessible bodies, spacecraft observations and remote sensing may significantly contribute to our current understanding of the geological, physical and chemical processes that resulted in divergent paths undertaken by the planets of the Solar System and their moons. Rocky Inner Planets, Giant Planets and, as well, the Minor Bodies of the Solar System are all very interesting targets for astrophysical studies because they can provide clues to the nature of the Solar System, the physical environment that characterized different regions at the epoch of planetary formation and their evolutionary stages, thus enhancing knowledge about our own existence.

2.1 Minor Bodies of the Solar System: discovering the first asteroids

In 1766, German astronomer Johann Daniel Titius noted that the distances of the known planets from the Sun essentially followed a geometric progression, later named the Titius-Bode law, after the contribution of Johann Elert Bode. This progression can be represented by the following equation:

$$r_n = 0.4 + 0.3 \cdot 2^n \tag{2.1}$$

in which r_n is the known distance (in astronomical units) of the n^{th} planet, where Mercury is identified with $n = -\infty$, Venus with $n = 0$, the Earth with $n = 1$, Mars with $n = 2$, Jupiter with $n = 4$ and Saturn with $n = 5$. The progression seemed to be invalid for $n = 3$, since apparently no discovered planet matched it, but in 1781, Sir William Herschel discovered the planet Uranus at a solar distance close to the solution predicted with $n = 6$, so further supporting the fact that the Titius-Bode relation could have been an expression of a true, but still unknown, physical law.

As a follow-up, a lot of observational effort was put searching for the "missing planet", orbiting between Mars and Jupiter, at the distance corresponding to $n = 3$. In 1801, Giuseppe Piazzi discovered the small body *Ceres* at just the right distance and in 1802 another body, *Pallas*, was discovered at the same orbital distance. Instead of a missing planet, astronomers were discovering a new population of minor bodies, later named *asteroids* (from Greek *asteroeides*, "star-like"), which are now known to orbit the so-called *Main Belt*.

2.2 General properties

Asteroids are small rocky bodies without atmosphere that orbit the Sun, having diameters ranging from few meters up to a maximum of 1000 km. Together with comets and Trans-Neptunian objects, they are now collectively known as the Minor Bodies in our Solar System, and they constitute a heterogeneous population of objects with different properties and individual histories [16].

Most of the asteroids currently known orbit between Mars and Jupiter, in the Main Belt (MB), but many other groups of asteroids are present at different distances from the Sun. As these groups are often defined from their dynamic relationships with other bodies in the Solar System, it is necessary to introduce the main mechanisms that drive their orbital motion, which are resonances and the Yarkovski effect.

2.2.1 Resonances

The general structure of the asteroid distribution is related to orbital resonances with a major planet. Resonances are divided in two major classes:

- **mean motion resonances** arise at solar distances where the asteroids orbital periods are some small integer fractions of a planet period. Stabilizing resonances occur mainly with Jupiter and Neptune asteroids, so that their orbits never closely approach the planet one. In the asteroid Main Belt, instead, these resonances have a destabilizing effect on the orbits, producing gaps in the asteroid distribution, called Kirkwood Gaps[1]. A gap is formed when the timescale over which a resonance is replenished with asteroidal material is far longer than the timescale over which resonant asteroids are transported to another region [17];

- **secular resonances** occur when the asteroid and major planet frequencies of precession (usually perihelion or ascending node precession) or variation of eccentricity and inclination are in relation. One of the most significant secular resonances is the ν_6 resonance, which occurs when the precession frequency of the asteroid's longitude of perihelion is equal to the sixth secular frequency of the planetary system, i.e. the mean precession frequency of Saturn's longitude of perihelion. [17].

Since asteroids in resonant positions experience close encounters with a major planet more often than the other asteroids in random location, they experience more frequently the attraction of this planet's gravity. Therefore, resonances provide potential escape route for most of the flux of asteroids [13].

[1] For example, Kirkwood gaps are located at the 4:1, 3:1, 5:2, 7:3 and 2:1 resonances with Jupiter.

2.2.2 The Yarkovsky Effect

The Yarkovsky effect is a consequence of the thermal inertia of a body, and is exhibited by a force experienced by a body due to the anisotropic emission of thermal photons, which carry momentum. Its influence is most significant for small bodies and could lead to large long-term effects in their orbits [13].

2.3 Minor Bodies distribution and classification

Minor Bodies are divided into groups and families based on their orbital characteristics (semi-major axis, perihelion and aphelion distance[2]) and generally named after their first discovered member. Groups are relatively loose dynamical associations, whereas families are tighter and result most probably from the catastrophic breakup of a large parent asteroid. Figure 2.1 displays the distribution of the main asteroidal bodies with respect to planets and the major gaps due to resonances.

2.3.1 Mars Crossers

Objects whose perihelion is located within the apsidal points of Mars' orbit are called *Mars crossers*, as they cross its orbit. It has been shown that this population is predominantly re-supplied by resonances in the Main Belt region called "intermediate-source Mars-crossing region", or IMC for short, which is delimited by the Main Belt, the Near Earth Asteroid (NEA) population and the ν_6 resonance. IMC asteroids can escape the Main Belt via mean motion resonances with Mars, three body mean-motion resonances (Jupiter-Saturn-asteroid) and the ν_6 resonance [13].

[2] In celestial mechanics, the perihelion is defined as the point in the orbit of an object at which it is closest to the Sun. On the other hand, the aphelion is the point at which the object is furthest to the Sun. To better understand the following pages, also the analytical definition is given:

$$\begin{cases} q = a \cdot (1 - e) & \text{(perihelion)} \\ Q = a \cdot (1 + e) & \text{(aphelion)} \end{cases}$$

where a is the semi-major axis and e the eccentricity of the orbit.

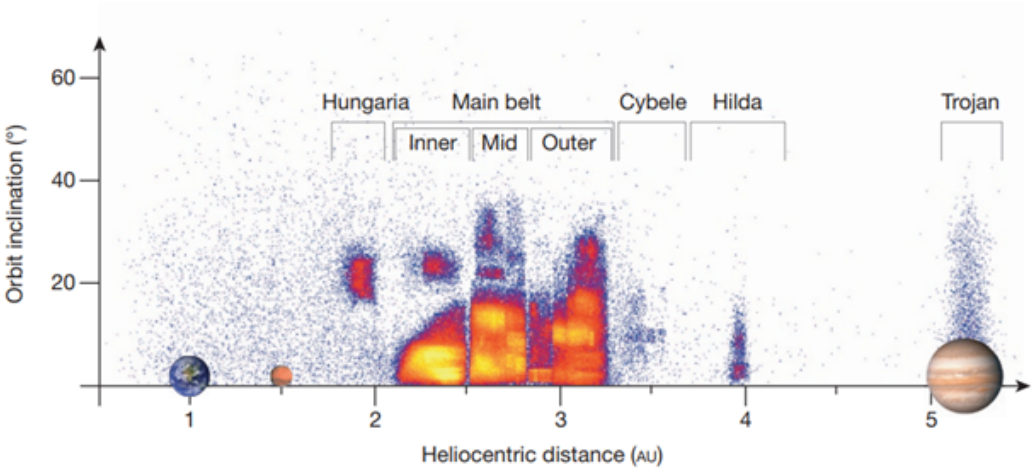

Figure 2.1: Plot of the location of the main asteroidal populations with respect to the planets and number density of objects (yellow represents the highest number density, blue the lowest). Kirkwood gaps are visible at 2.5 AU and 2.85 AU [1].

2.3.2 Main Belt Asteroids

Most of the asteroids are found between the orbits of Mars and Jupiter. The region between 2.0 and 3.3 AU, which experiments the strongest concentration of asteroids, is the *Main Asteroid Belt*. The asteroids in this region are divided into groups and families by the Kirkwood gaps, cleared through Jupiter's orbital resonance. Table 2.1 summarizes the main groups of asteroids and their characteristics.

Group	Semi-major axis	Eccentricity	Inclination
Hungaria	1.78-2.06 AU	< 0.18	16°-34°
Inner Main Belt (Phocaea)	2.06-2.50 AU	> 0.1	18°-32°
Middle Main Belt	2.50-2.82 AU	—	—
Outer Main Belt	2.82-3.28 AU	—	—
Cybele	3.28-3.70 AU	< 0.3	< 25°
Hylda	3.7-4.2 AU	< 0.07	< 20°

Table 2.1: Main Belt principal groups of asteroids.

2.3.3 Jupiter and Neptune Trojans

Another important class of bodies are those lying around the L4 and L5 lagrangian points of a planet[3] (therefore, placed 60° ahead and behind the planet, on the same orbit). Referring to Jupiter, these regions were respectively called the *Greek* and *Trojan* nodes, and objects in each node are therefore named after members of that side of the famous epic conflict. Altogether they are now called *Jupiter Trojans*. Although the existence of trojan-like asteroids is not a dynamical prerogative of Jupiter, for a long time no other planets were observed to have objects like these. Finally, in 1990, the first Mars Trojan was found, (5261) Eureka, together with other five asteroids, but they are now considered as simple Mars Crossers. In 2001, the first Neptune Trojan was also discovered (2001 QR322) and since then other 3 Neptune trojans were found.

2.3.4 Jupiter Family Comets

Comets are frozen leftovers from the formation of the Solar System composed of dust, rock, and ices [19]. They are usually grouped in long period comets and short period ones. Short period comets with orbital periods under 20 years, low inclination and Tisserand Invariant[4] T_j between 2 and 3, are called *Jupiter-family comets* (JFCs) since their orbits are primarly determined by Jupiter's gravitational influence.

Short period comets are believed to originate from the Kuiper Belt, the large reservoir of small icy bodies just beyond Neptune. From collisions between Kuiper Belt objects or grav-

[3] Lagrange Points are five positions in space where the gravitational forces of a two body system like the Sun and the Earth produce enhanced regions of attraction and repulsion.At Lagrange points, the gravitational pull of two large masses precisely equals the centripetal force required for a small object to move with them. Of the five Lagrange points, three are unstable and two are stable. The unstable Lagrange points - labeled L1, L2 and L3 - lie along the line connecting the two large masses. The stable Lagrange points - labeled L4 and L5 - form the apex of two equilateral triangles that have the large masses at their vertices [18].

[4] The Tisserand Invariant is a parameter related to the three-body problem, and it was used to classify different comet populations. It is defined as:

$$T_j = \frac{a_j}{a} + 2\cos i \cdot \sqrt{\frac{a_j}{a} \cdot (1 - e^2)} \tag{2.2}$$

where a_j ad a are, respectively, Jupiter's and the object's orbit semi-major axis, i the inclination and e the eccentricity of the comet's orbit

itational perturbations, some of these objects can escape the Kuiper Belt and be gravitationally perturbed by Neptune into highly elliptical orbits around the Sun. As they approach Jupiter, the orbits of these small bodies may be perturbed further, reaching the Earth's orbit.

2.3.5 Centaurs

Centaurs are small bodies, orbiting between Jupiter and Neptune (i.e. semi-major axis, a, 5.4 AU $\leq a \leq$ 30 AU), not yet clearly defined from a dynamical point of view. Centaurs probably represent objects in an intermediate orbital state that are transitioning from the Kuiper Belt to the Jupiter Family comets. As the Centaurs might be dimensionally and compositionally representative of the Kuiper disk population, their physical properties are of interest and, because they are closer to the Earth, they are more easily observed than the distant and faint Kuiper belt objects [20]. They are probably much closer to comets than asteroids, and one of these (Chiron) has shown episodic cometary activity.

2.3.6 Trans Neptunian Objects

Objects with orbit's semi-major axis $a \geq 30$ AU are defined as *Trans-Neptunian Objects* (TNOs), and are then divided in other distinct dynamical populations.

- **Kuiper Belt Objects**: they include the majority of the objects discovered to date and are located in near circular orbits with semi-major axis 41 AU $\leq a \leq$ 47 AU [20]. Some objects, orbiting beyond $\sim$ 41 AU, are not controlled by resonances with the outer planets and are called *Cubewanos*, from the first trans-Neptunian object found, 1992 QB1.

- **Plutinos**: they are objects, like Pluto, in (3:2)[5] resonance with Neptune.

- **Scattered-Disk Objects**: this population consists of objects in highly eccentric orbits ($0.34 \leq e \leq 0.94$) that generally have semi-major axis 50 AU $\leq a \leq$ 675 AU. These are

[5] That means that after these objects and Neptune have completed 3 and 2 orbital revolutions, respectively, they will have the same position, each one in its own orbit.

objects that encountered Neptune and were "scattered" into long-period orbits with perihelion still not too far from Neptune's orbit.

- **Oort Cloud Objects**: the Oort Cloud is a postulated spherical cloud, centered on the Sun, whose outer boundary extends for $\sim$ 100000 AU. The cloud contains about a trillion of icy objects, which could be stable comet nuclei, as the Sun radiation at these distances is faint, and represent a constant supply of new comets.

2.3.7 Near Earth Objects

Near-Earth Objects (NEOs) represent a population of objects very diverse in nature, comprising asteroids (NEAs) and extinct comet nuclei (NECs) in orbits with perihelion distances q $\leq$ 1.3 AU which periodically approach or intersect Earth's orbit. NEOs are believed to be a source for most meteorites which arrive on Earth, given their vicinity to our planet. The proximity of NEOs to Earth also makes them attractive subjects on a practical level, and those having low-inclination and low-eccentricity orbits closest to our planet are among the most accessible spacecraft destinations for remote sensing investigation in the Solar System.

Asteroidal NEOs are traditionally subdivided into groups based on their orbital characteristics (semimajor axis,perihelion distance, aphelion distance) with respect to Earth's: *Atens* and *Apollos* are Earth Crossers ($a \leq 1$ AU) while *Amors* approach the Earth but never intersect its orbit ($a \geq 1$ AU).
The question of NEOs origin is still open. It is well known that present NEOs have typical life-times of 10-100 million years (much shorter than the age of the Solar System), and that over these time scales NEOs either are ejected from the Solar System or collide with the Sun or a planet. Craters on the Moon hold physical evidence of a fairly constant NEO population during the past 2 billion years, so new NEOs must be continuously supplied by the above mentioned sources in order to maintain the present steady state. The principal one is the MB: most asteroidal NEOs are believed to be collisional fragments that were driven out of it by a combination of Yarkovsky thermal forces and resonant phenomena that increased their orbital eccentricity [17], thus allowing them to reach planet-crossing orbits. The second source

is represented by dead or dormant comets, which basically are de-volatilised cometary nuclei and/or comets whose gas emissions is inhibited by a sort of non volatile crust, originally coming from the Kuiper Belt and the Oort Cloud. Other sources of Near Earth asteroids can be the Mars-Crossers Asteroid population and the Outer Main Belt (OB) population.
Among all Minor Bodies present in our Solar System, NEOs are of particular interest for astrophysical studies. These objects are part of the surviving population of planetesimals from the very earliest stages of Solar System formation and thus they provide the primary constraints on the processes and conditions characterizing the late Solar Nebula, the early Solar System, and the subsequent planetary accretion. From detailed knowledge of NEOs compositions, constituent materials and thermal histories of their asteroid and comet parent bodies can be inferred. Further, because meteorites and interplanetary dust particles represent the primary evidence for the environments and mechanisms of the formation of the Solar System, if specific meteorite and dust groups can be compositionally associated with NEOs, and the NEOs related to Main Belt asteroids and comets, the interrelations between all these objects can be tested, providing a context for the laboratory studies of meteorites and dusts [21].

2.4 Spectroscopic analysis and taxonomy of NEOs

Many issues related to the heterogeneous group of NEOs can be addressed by characterising them spectroscopically, in order to derive their mineralogy, and by classifying them taxonomically, attempting to find an order in their physical properties.

2.4.1 Asteroid spectrum

Of the incident solar flux arriving on an asteroid surface, part is diffused and part is absorbed, and the ratio depends on surface albedo. Therefore, the Earth receives both the solar flux diffused by the body surface and its black-body radiation, emitted by the body as a function of its temperature. In asteroid spectra, diffused sunlight dominates the flux from the ultraviolet to the near-infrared (0.35-2.50 μm), while at longer wavelength (2.5-5.0 μm, depending on

the surface temperature) the contribution due to the asteroid black-body emission becames detectable.

Visible and near-infrared reflectance spectroscopy has been widely used to characterise the surface composition of most asteroid types, and diagnostic features in reflectance spectra are detectable in the 0.35-2.50 μm range. The most important mineral species present in asteroid spectra are characterised by unique composition or limited compositional differences, so each of them produces a characteristic reflectance spectrum. Most asteroids are composed of mixture of these minerals, so since the spectral parameters of the different absorption features are related to a specific composition of the individual mineral, spectral analysis of the asteroid surface is able, in most cases, to detect mineralogical signatures characteristic of a particular species, establishing the presence of a specific mineral phase. This is an important step in understanding the asteroid's origin and evolution.

The two most notable surveys in the 1980s to measure the spectral characteristics of a large number of asteroids were the Eight-Color Asteroid Survey and the 52-color survey. ECAS data are the basis for the asteroid taxonomy that is still used today.

2.4.2 Tholen taxonomy

Tholen's taxonomy separates asteroids into different classes with similar reflectivity and albedos, and is the most widely used. In the following, the main characteristics of each class will be described.

- **Taxonomic class A**. A-asteroids show an important decrease in reflectance in proximity of 0.7 μm, related to metal compounds, and a strong absorption feature near 1 μm, but not relatable with pyroxene[6]. The spectrum of olivine [7] is clear, but it is still difficult to specify how much metal is present in the bodies. The albedo coefficient range among the A-type asteroids is wide, so it could be representative of different

[6] Piroxenes are a group of silicate minerals with igneous or metamorphic origin.
[7] Olivine is a magnesium iron silicate.

metal abundances (higher metal content produces a darker surface). These asteroids are assemblages of mono-mineral olivine or olivine-metal from mantle regions of differentiated parent bodies [8];

- **Taxonomic class S**. S-class spectra are characterised by a moderate steep slope at wavelengths shorter than 0.7 μm and by weak absorption features around 1 μm and 2 μm, which indicate the presence of some mixture of olivine, pyroxene and Fe-Ni metal. S-asteroids are moderately bright, with albedos varying from 0.1 to 0.3, and are mostly found in the Inner Asteroid Belt ($\sim$ 2.2 AU) and in the Middle Belt ($\sim$ 3 AU) [22];

- **Taxonomic class Q**. Few asteroids belong to this class, and are all part of the NEO population. A representative member of this class is the NEO 1862 Apollo, which has a spectrum strongly reddened[9] shortward of 0.7 μm and a strong absorption feature at 1 μm, indicating the presence of a mixture of olivine and pyroxene;

- **Taxonomic class R**. This class only comprises the asteroid 349 Dembowska. The reflectance spectrum shows strong absorption feature at 1 μm and 2 μm, indicating a pyroxene-olivine assemblage with little or no metal;

- **Taxonomic class V**. V-class spectra are characterised by two strong, symmetric absorption features centered near 1 μm and 2 μm,due to iron-bearing, low calcium pyroxene, with a fainter feature near 1.2-1.3 μm, probably due to plagioclase feldspar[10]. This class was firstly proposed for the asteroid 4 Vesta, but now it is known that analogous spectra are found for the so-called Vestoids, which are small asteroids near Vesta and the ν_6 and (3:1)[11] resonances. They are thought to be small fragments delivered by Vesta

[8] Differentiation is the process of an asteroid accreting to the point that most of the metal distributed throughout its mass is pulled by gravity to its center to form a core. This leaves the lighter rocky material to float above the iron-nickel core forming a mantle.

[9] When a spectrum is said to be reddish or blueish, it means that it has a stronger irradiance at longer or shorter wavelengths, respectively.

[10] Plagioclase is a series of tectosilicate minerals within the feldspar group, with sodium and calcium atoms that can substitute for each other in the mineral's crystal lattice structure.Plagioclase is a major constituent mineral in Earth's crust.

[11] The 3:1 resonance with Jupiter generates one of the Kirkwood gaps, as asteroids are ejected from this zone.

itself. Among NEOs, bodies having spectra similar to that of Vesta have also been identified, confirming the efficiency of the delivery mechanisms from the Main Belt.

- **Taxonomic class C (B,F,G and P)**. C-group is a wide set of asteroid spectra, representing dark and primitive objects. Asteroids belonging to this group have nearly featurless spectra longward of 0.4 μm, but different UV absorption intensity. Within this set, several subclasses have been distinguished (B,F,G,P). UV absorption features have different intensities among these classes: starting from P-class, which is featureless, the intensity gradually increases with F,B and C classes, up to class G, which has the strongest features. The B-class has flat to slightly bluish ECAS spectra while the C-class has flat to slightly reddish spectra. The B-class also tends to have higher albedos than the C one. B,F and G classes are believed to be the result of metamorphic evolution of C-class parent material. The P-class, found in the Outer Main Belt, is believed to be a transitional primitive class between C and D;

- **Taxonomic class D**. Spectra of the D-asteroids are generally featureless with neutral to slightly red spectra shortward of 0.55 μm, and very red spectra longward of 0.55 μm. These asteroids have low albedo (≤ 0.05) and are mainly found in the Outer Main Belt and between the Trojan asteroids;

- **Taxonomic class E**. E-asteroids exhibit featureless or very weakly featured flat to slightly reddish spectra, and have high albedo (~ 0.44). The nearly absent absorption features indicate the presence of very iron-poor or iron-free silicate. E-type asteroids dominate the Hungaria asteroid region, which is located between 1.79 AU and 1.98 AU: half of all E-type asteroids known in the Main Belt are located here. Among NEOs, E-types asteroids are rare, and the first discovered one was 3103 Eger (roughly 1.5 km size). Its orbit has the aphelion distance within the Hungaria zone, and this fact appears to indicate that Eger was most probably derived from that region;

- **Taxonomic class M**. M-type asteroids have reddened and weakly featured spectral reflectance curves, similar in shape to those of the E and P-asteroids, but have inter-

mediat albedos. Available data are consistent with Fe-Ni metals, so that these asteroids have generally been thought to be exposed metallic cores of differentiated parent bodies which suffered catastrophic disruption. Some M-asteroids show a 3 μm absorption feature, suggesting the presence of clays, which is in partial contrast with a metallic composition;

- **Taxonomic class T**. T-asteroids have low albedos (≤ 0.10) with spectra that are slightly red shortward of 0.85 μm. They are interpreted as made by highly altered carbonaceous material and also as physical mixture of S and C-type material.

Figure 2.2 displays a map of the distribution of mass of the asteroid belt.

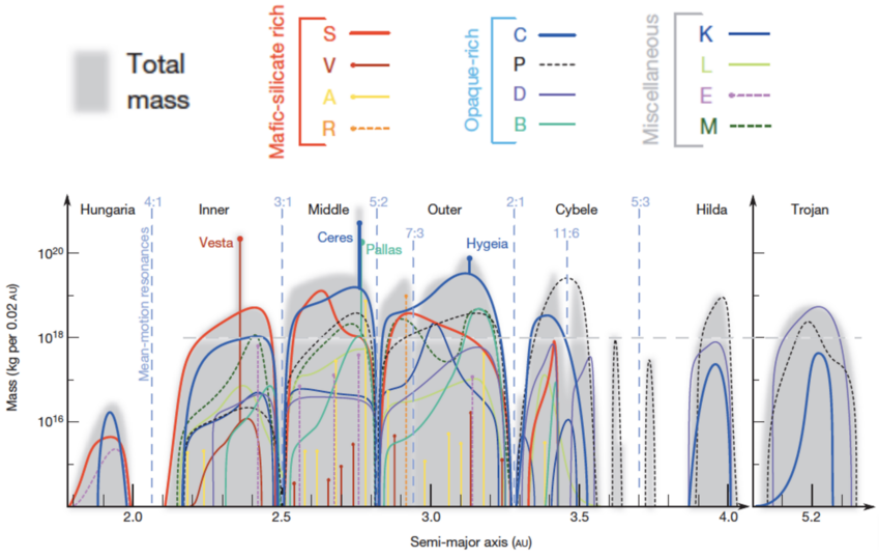

Figure 2.2: The compositional mass distribution throughout the asteroid belt. The grey background represent the total mass within each 0.02-AU bin. Each colour indicates a spectral class of asteroid [1].

2.5 Planetary exploration

The planets in the Solar System can be divided into three major groups: the rocky *Inner Planets*, (Mercury, Venus, Earth and Mars), the gaseous *Giant Planets* (Jupiter and Saturn) and the icy *Outer Planets* (Uranus and Neptune). There are two main goals of planetary exploration:

- understanding the formation of the planetary system from the solar nebula, various stages of their chemical and geological evolution and timescales;
- assessment and exploitation of planetary resources for human exploration and settlement.

In addition to ground-based observations, remote sensing of terrestrial planets has been achieved by many orbiting or flyby spacecraft (Mariner 10 and MESSENGER on Mercury; Mariner 9, Viking, Mars Global Surveyor, Mars Odyssey, Mars Express, Mars Reconnaissance Orbiter on Mars; the Venera spacecraft, Pioneer Venus, Magellan and Venus Express on Venus). Our knowledge of the Giant planets has benefited from the flybys of Voyager 1 and 2, as well as Galileo and Juno on Jupiter and Cassini on Saturn. The next sections will summarize some of the key questions about various planetary bodies that can be resolved by future planetary missions, equipped with remote sensing instruments like imagers and spectrometers, to gather information about the environment and the mineralogical, chemical and geological processes [23].

2.5.1 Moon

This is the one of the most mysterious body in the Solar System, in the sense that its origin is not well understood. How the Earth, of the four Inner Planets, came to have such a large and permanent satellite, with a chemical composition very similar to that of the Earth's mantle, is still a mystery. Mercury and Venus have no satellites, and Mars has only two small and transient satellites (Phobos and Deimos) that will not stay in the Martian orbit for long [23]. For this reason, the existence of the Moon in its orbit has been seriously debated and several hypotheses have been put forward. One of the main objectives of lunar exploration is therefore to understand the mechanism of the formation of the proto-moon and its acquisition by the Earth. The most favoured hypothesis for the origin of the Moon today is the "giant impact hypothesis". This involves the accidental collision of a body with the early Earth and can explain its chemical, isotopic and dynamical characteristics [24]. A global mapping of the Moon to characterise the composition of the lunar surface in the context of its geological evolution may therefore provide some important insights into this topic.

2.5.2 Mercury

As the smallest and least altered of the rocky planets, Mercury holds clues to our understanding of the formation of the Solar System and is considered a test bed for formation theories. Mercury is of particular interest because it has the highest density (5.3 g/cm^3) of all the planets and a global magnetic field [25]. The internal structure of Mercury, as well as its surface mineralogy, composition and topography, are therefore of great scientific interest for understanding its early differentiation history. In addition, Earth-based radar observations indicate the presence of water in its polar regions. Despite its proximity to the Sun, water has survived because some regions at the poles are under permanent shadow, and thus very cold [23].

2.5.3 Venus

Venus is a planet that is similar to Earth in terms of some important planetary parameters (size, mass, position in the Solar System, presence of atmosphere) and different in terms of other, equally important ones (absence of an intrinsic magnetic field, large atmospheric mass, carbon dioxide composition of the atmosphere, lack of water, very high surface pressure and temperature). The high surface temperature (about 470°C) and high CO_2 atmosphere, with a pressure about 90 times that of the Earth's atmosphere, suggest that its evolutionary history has been unique due to an important greenhouse effect [26]. Radar mapping of the surface of Venus has revealed that its surface is covered with mountains, large craters and lava flows, revealing evidence of intense, global volcanic activity that dates back around 500 million years. The important question about the evolution of Venus relates to its interior processes that lead to volcanic eruptions on a global scale, and to the circulation, composition and interaction of its atmosphere with its surface, leading to extremely different rotation rates for the near-surface and upper atmospheric layers [23]. The examination of Venus is specific to its distinctive evolutionary history and may not be crucial regarding the overall progression of the Solar System; however, it offers a unique example of planetary processes that are not found elsewhere.

2.5.4 Mars

Mars is a terrestrial, rock-dominated, Inner Planet. By being smaller and farther away from the Sun, it is characterized by a cold and tenuous atmosphere that has developed differently from that of Earth and Venus. Presently, the atmospheric composition and H_2O and CO_2 cycles are not well comprehended. Multiple pieces of geological evidence suggest that the past climate of this region varied significantly from the present one, with the occurrence of liquid water on the surface [27]. It is believed that this environment could have supported life, therefore Mars is a target for focused exploration. Experiments to detect biological activity on the planet were conducted by the Viking-1 and 2 orbiter-lander pairs in 1975-1976. Although the observations suggest the absence of any biogenic processes, it is important to note that some of these conclusions may not be entirely definitive [23]. Further study of the Martian atmosphere, ionosphere, weather and dust storms, along with complementary imaging spectroscopy for the examination of Martian surface mineralogy, chemistry and records of ancient water, has the potential to provide more comprehensive information compared to what is currently available. An anomalous concentration of methane may be biogenic, thus a dedicated orbiter mission to measure methane in the atmosphere and ground-level sources could help identify areas of biological activity [28].

2.5.5 Giant Planets and their moons

Jupiter and Saturn are called ”Gas Giants” because they are mainly composed of hydrogen and helium [29]. They are thought to consist of an outer layer of compressed molecular hydrogen surrounding a layer of liquid metallic hydrogen, with probably a molten rocky core inside. The atmosphere contains many layers of visible clouds that are mostly composed of water and ammonia. Instead, Uranus and Neptune are called ”icy giants”. They are composed of hydrogen and helium, but also contain heavier elements such as oxygen, carbon, nitrogen and sulphur. Beneath their relatively thin hydrogen and helium shells, these planets’ mantles are largely made up of compressed water and ammonia, also known as ”volatiles” or ”ices” due to their freezing points above -173°C.

These planets have very different histories of formation and evolution.The first close looks at the systems of Jupiter, Saturn, Uranus and Neptune were taken by the Pioneer 10 and 11 spacecraft, followed by the Voyager 1 and 2 flyby missions in the decades after their launch in the 1970s. The Hubble telescope, Galileo, Chandra, Juno and other missions have also observed features in the atmospheres and their satellite systems. The discovery of water ice, sulphur and other volatiles on several of Jupiter's Galilean satellites makes them particularly interesting objects for further exploration. Ganymede is not only Jupiter's largest moon, but the largest moon in the entire Solar System. Data suggest that Ganymede has a three-layer structure: a small, partially molten iron/sulphur core surrounded by a rocky silicate mantle with an icy shell on top, with an ice crust floating above a warmer ice mantle that may contain liquid water. The evidence for water ice on Europa is more compelling. Callisto has the lowest density (1.86 g/cm^3) of the Galilean satellites. Recent observations suggest that Callisto has a crust about 200 km thick, and beneath the crust there may be a salty ocean more than 10 km thick. Their proximity to Jupiter, whose atmosphere contains organic molecules necessary for life, makes the Galilean satellites attractive from the point of view of the possibility of biological activity. Saturn's moons are just as exciting. Images of the moon Enceladus, taken by Cassini, show geysers erupting from its surface, probably generated by an internal heat source. On Titan, liquid ethane and methane have been found, as well as carbon dioxide, cyanogen dioxide[12] and benzene. Titan's atmosphere contains mainly ammonia, nitrogen and methane, similar to Earth's primitive atmosphere when life originated. While several spacecraft have extensively studied Jupiter and Saturn since the early 1970s, much of what we know about the properties of the Icy Giants Uranus and Neptune comes from brief flybys by the Voyager 2 spacecraft and from remote observations. Data on their atmospheric composition, structure, dynamics, magnetic fields, interiors, rings and satellites are still quite limited. A comprehensive study of the icy giant planets is therefore essential to understand their formation and migration scenarios, as well as their role in the formation of the Outer Solar System [30, 23].

[12] A chemical compound with the formula $(CN)_2$

3

Introduction to the Optical Systems

The previous Chapter highlighted how the study of planets, their moons and Minor Bodies is of paramount importance to understand the Solar System and our planet, the Earth. It is now clear that a space mission is the only adequate approach to address and resolve the important planetary science questions associated with Inner and Outer Planets and the Minor Bodies population. Among the various methods, visual and infrared (VIS/IR) imaging and/or spectroscopic remote sensing are key technologies to investigate planetary surfaces, and the adjacent atmosphere, to study their composition, texture, structure and dynamics. In this Chapter, the two most relevant optical systems for space imaging applications, the telescope and the spectrometer, will be introduced. Firstly, their fundamental characteristics will be described, then a specific application will be presented, which will act as a starting point for further enhancements. If the previous pages aimed to address *why* there is a need to observe these bodies, the next few pages will attempt to answer *how* to observe them in the most effective way.

3.1 Introduction to telescopes

A telescope is an optical system consisting of multiple lenses and/or mirrors that gathers the light (or the electromagnetic radiation in general) entering from an aperture and focuses it on the focal plane, forming an image. Considering their constituent elements, telescopes may be divided into three categories: refractive telescopes, which are formed by lenses, reflective telescopes, formed by mirrors, and catadioptric telescopes, which combine both elements. Lenses and mirrors can be arranged in a lot of different ways, resulting in a variety of possible configurations, suited for specific scientific purposes or requirements.
The main parameters that define a telescope are:

- **Focal length**: it is the distance from the center of a lens or a mirror to the focal point. Given the same Focal Plane (detector) size, short focal lengths provide a wide field of view and low magnification, while longer focal lengths produce a narrower field of view and greater magnification.

- **Aperture**: it determines the amount of light gathered by the telescope, the bigger the aperture, the brighter the image.

- **Angular resolution**: it represents the ability of a telescope to separate two point sources into two distinct images. The principal physical limitation to the angular (or spatial) resolution of any optical system is *diffraction*. Diffraction is due to the wave nature of radiation and is defined as the bending of waves around the edges of an obstacle or through an aperture when they are illuminated by a radiation of wavelength λ. So, even in a perfect optical system under ideal conditions[1], the image on the focal plane is never point-like, but has a characteristic pattern. For a circular aperture, the intensity pattern is analitycally described by the so-called Airy disk (see Figure 3.1).

[1] That means:

1. No geometrical aberrations;
2. 100% photo collection efficiency.

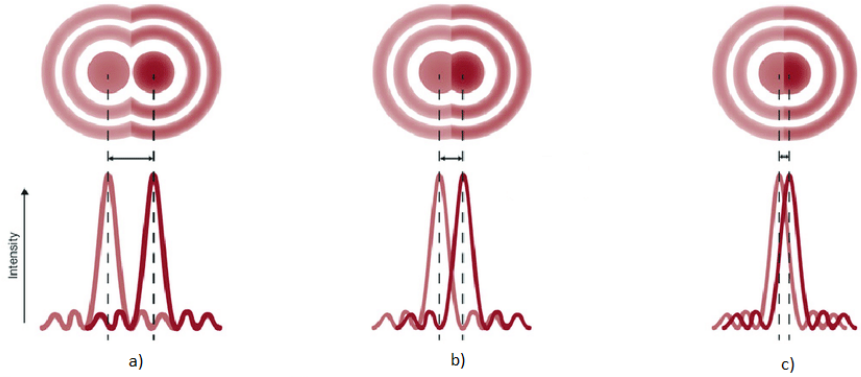

Figure 3.1: From left to right, it is possible to see the Airy disks of two point sources that are: a) resolved, b) just resolved, according to Rayleigh criterion, c) not resolved [2].

From the aperture, the angular width at half maximum of the Airy disk is given by Equation 3.1:

$$\sin\theta_r = 1.22\,\frac{\lambda}{D} \tag{3.1}$$

where:

θ_r is the angular width;

λ is the wavelength of the incoming light;

D is the aperture diameter.

According to Rayleigh criterion, two Airy components are considered as "just" resolved when the principal maximum of one coincides with the first minimum of the other, as can be seen in Figure 3.1.

An optical system whose resolution performance reaches the instrument's theoretical limit is said to be diffraction-limited.

- **Angular magnification**: it is given by the ratio between the angle subtended by the image of an object produced by the telescope and the angle subtended by the object itself.

- **Focal ratio**: it is the ratio between the focal length f and the system aperture d. The

focal ratio, also known as f-number, is usually expressed as $f/\#$, where

$$\# = \frac{f}{d} \tag{3.2}$$

is the value of the focal ratio. The focal ratio is indicative of the image brightness, which can be written as:

$$B_\Sigma \propto \frac{t_{exp}}{\alpha^2 \cdot (f/\#)^2} \tag{3.3}$$

where t_{exp} is the exposure time and α is the source angular size. Thus, given the same t_{exp} and α, if a telescope has a small $f/\#$ the surface brightness is larger, and vice versa.

In the overall analysis and design of an optical system, the Gaussian (or paraxial) optics approximation, which only considers rays that form a small angle to the optical axis of the system, is no longer suitable. In a real optical system, lenses and mirrors usually have some flaws, hence it is essential to introduce in the analysis also oblique and skew rays. These rays can intercept the axis of the optical system, but not necessarily in the object position, or they may not intercept the axis at all. The result is an image that deviates from the ideal point-like distribution obtained with paraxial optics.
The distance on the image plane between the track of a ray and the track of the chief one for the specific field of view is referred to as *ray aberration*.
It is possible to divide aberrations into two main groups: chromatic and monochromatic. The former are relevant only for refractive elements and arise because light of different wavelengths has different refractive indices, therefore the focal length of a given lens varies with the colour of the incident light. The latter are also called primary or Seidel aberrations, and are entirely due to geometry. They can be divided into five main subgroups:

1. **Spherical aberration**: it is an axial-symmetric optical defect for which the focal length varies according to the radial distance of the point of incidence of the rays on the optical elements. The image obtained at the focal plane of an object at infinite distance is equal to a bright central spot surrounded by a symmetrical halo. This is the only monochromatic aberration suffered by an on-axis source, and is more dramatic for

systems with large apertures.

2. **Astigmatism**: it occurs when an object point lies at a certain distance from the optical axis, because the relative cone of rays impinges asymmetrically on the optical system. Therefore, the focal lengths are different if different planes of incidence are considered.

3. **Coma**: it can be defined as the change of magnification of the optical system with the aperture. Tilted rays impinging on edge portions of an optical element are imaged at different heights with respect to that of the rays passing through the center of the optical element.

4. **Petzval field curvature**: in an optical system the image plane is approximately plane only in a small region around the optical axis. For finite apertures, the surface of stigmatic image is, in fact, curved.

5. **Radial distortion**: it occurs when the image of an off-axis point source produced by the optical system is at a distance, from the optical axis, smaller (*barrel distortion*) or larger (*pillow distortion*) than what is expected from paraxial optics.

It is clear, at this point, that the ultimate goal while designing an optical system is to reduce aberrations as much as possible.
Typically, the analysis of the performance of an optical system is carried out via ray-tracing softwares, where many rays from a single source point in object space are directed through a uniform grid of points in the entrance pupil and then imaged by the optical elements. The distribution of rays in the image plane is called *Spot Diagram*, and it enables to immediately see the effect of aberrations on the image produced by the optical system. The Spot Diagram is usually compared to the diffraction-limited response, i.e. the Airy Disk, which represents the smallest spot size assuming a geometrically perfect system. If all the rays lie within the Airy Disk, the system can be said to be diffraction-limited.
In Figure 3.2 the effect of three major aberrations on the Spot Diagram is depicted.

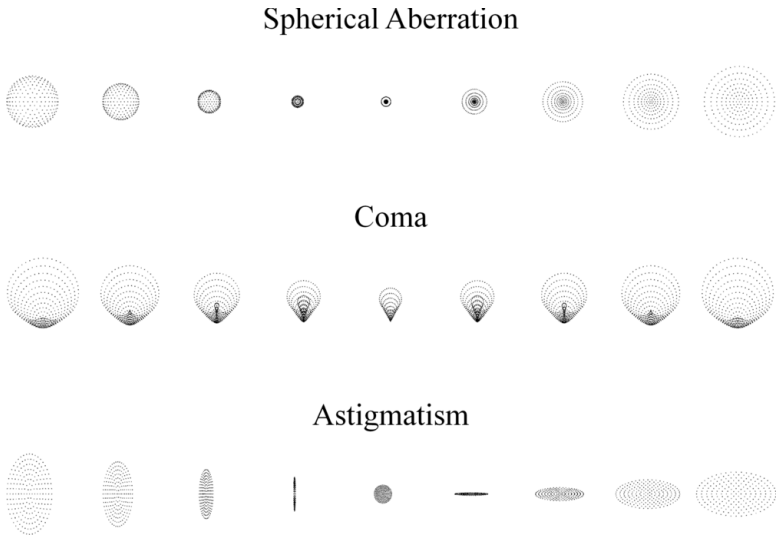

Figure 3.2: Different types of aberrations are characterised by peculiar patterns; in this image they are represented as a function of the longitudinal distance from the optimal focus, set at the center of the range [3].

3.1.1 The Three Mirror Anastigmatic telescope

A Three-Mirror Anastigmatic (TMA) is a particular telescope configuration built with three curved mirrors, first proposed by Dietrich Korsch in 1977. This configuration is quite interesting because it allows to minimize the aberrations of astigmatism, coma, spherical aberration, and Petzval field curvature.
The typical TMA design (see Figure 3.3 (a)) is formed by a primary mirror that converges the light from a source at infinite distance on a secondary one. The reflected light creates an intermediate image before reaching the tertiary, which creates the final image. A flat mirror might be placed at the exit pupil to fold the image away from the axis of telescope for a more convenient configuration.

In another possible configuration, a flat holed mirror is required. In this case, the light reflected by the secondary mirror reaches the holed one, placed diagonally between the primary and the tertiary mirrors, and is then redirected to the tertiary. Light is reflected again and converges to the image plane, passing through the holed mirror. The advantage of this design is the minimization of the obscuration, as it is easier in this case to support the folding

mirror.

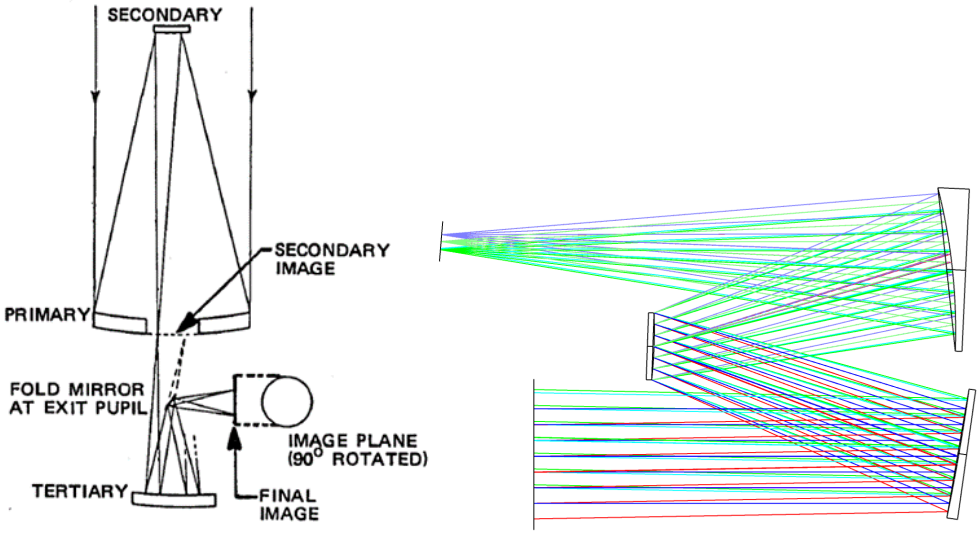

(a) Korsch TMA. **(b)** Off-axis, unobscured TMA.

Figure 3.3: A classical Korsch TMA configuration and an off-axis, unobscured one.

The last significant configuration is the unobscured, off-axis TMA. In this configuration, the three mirrors can be tilted and/or decentered with respect to the optical axis to completely avoid obscuration without the necessity to operate with holed optics.
The advantages deriving from selecting a TMA telescope are a larger field of view, a small occupied volume and, of course, the aberration correction.

3.2 Introduction to spectrometers

Spectrometers are optical instruments widely used to measure the emission of electromagnetic radiation from an object or the interaction of electromagnetic radiation with an object (absorption, scattering). Typically, a spectrometer is formed by an aperture that gathers light from a source, an optical element which disperse the incident radiation as a function of its frequency/wavelengths components, and a detector that collects it. The spectral components are dispersed along different directions depending on the characteristics of the dispersing element and on the system geometry.

The optical element which provides the spectral dispersion can be a prism or a diffraction grating, both shown in Figure 3.4.

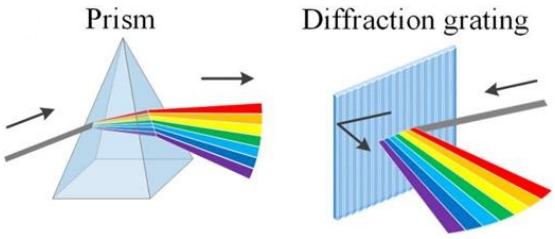

Figure 3.4: A prism and a diffraction grating.

In a prism the radiation beam is dispersed because of the wavelength dependence on the refractive index of the material, which is usually glass. A diffraction grating, instead, exploits a surface with a periodic structure of grooves to provide the spectral dispersion of the incident beam.
The diffraction angles of the diffracted beams depend on the incident angle of light, the groove spacing on the grating and the wavelength of the incoming light, according to Equation:

$$\sin\alpha + \sin\beta = \frac{m \cdot \lambda}{d} \tag{3.4}$$

where:

α is the angle between the normal of the surface and the incoming ray;
β is the angle between the normal of the surface and the diffracted ray;
m is the diffraction order;
λ is the wavelength;
d is the groove spacing.

Diffraction gratings can be classified into two main types based on the manufacturing process. The first type consists of ruled gratings, which are created by ruling parallel grooves on a reflective surface with a diamond-tipped tool. The second one includes the holographic gratings, which are manufactured with a photolithographic process that exploits an interference

pattern. A surface is covered by a photosensitive layer and then exposed to monochromatic and coherent laser beams that interfere and create a sinusoidal pattern of fringes, engraving the grooves.

3.2.1 The Offner configuration

Spectrometers exist in different configurations which may leverage convex or concave gratings. One of these is the classical Offner configuration, where the beam entering from a slit strikes a concave spherical mirror that reflects it onto a spherical convex grating. The latter has a radius of curvature half that of the mirror. The dispersed light beam is then directed towards the same mirror and focused on the detector. In cases where the system is fast and/or high dispersion gratings are utilized, the mirror is usually divided into primary and tertiary components. Radius curvatures and distances must be independently selected for each component to ensure optimal performance. In this instance, the modified Offner spectrometer configuration is obtained, as displayed in Figure 3.5. This configuration can be optimised to decrease spatial and spectral aberrations. Due to its compact size and effective correction of aberrations, this spectrometer has been utilised in push-broom imaging spectrometry.

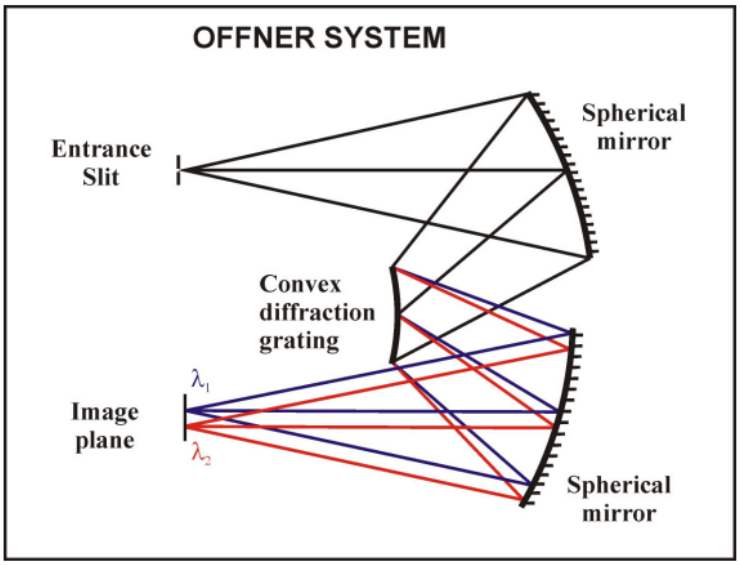

Figure 3.5: The modified Offner configuration [4].

3.3 The starting designs: VICESS and HYPSOS

3.3.1 The Visible and Infrared Camera for the Exploration of the Solar System

The first instrument taken into consideration is the Visible and Infrared Camera for the Exploration of the Solar System (VICESS), a multispectral camera proposed in [15] to study and map a targeted rocky body in the approach and orbit phase, determining its dynamical parameters, surface geomorphology and composition via surface reflectance characteristics, thanks to the multispectral imaging.

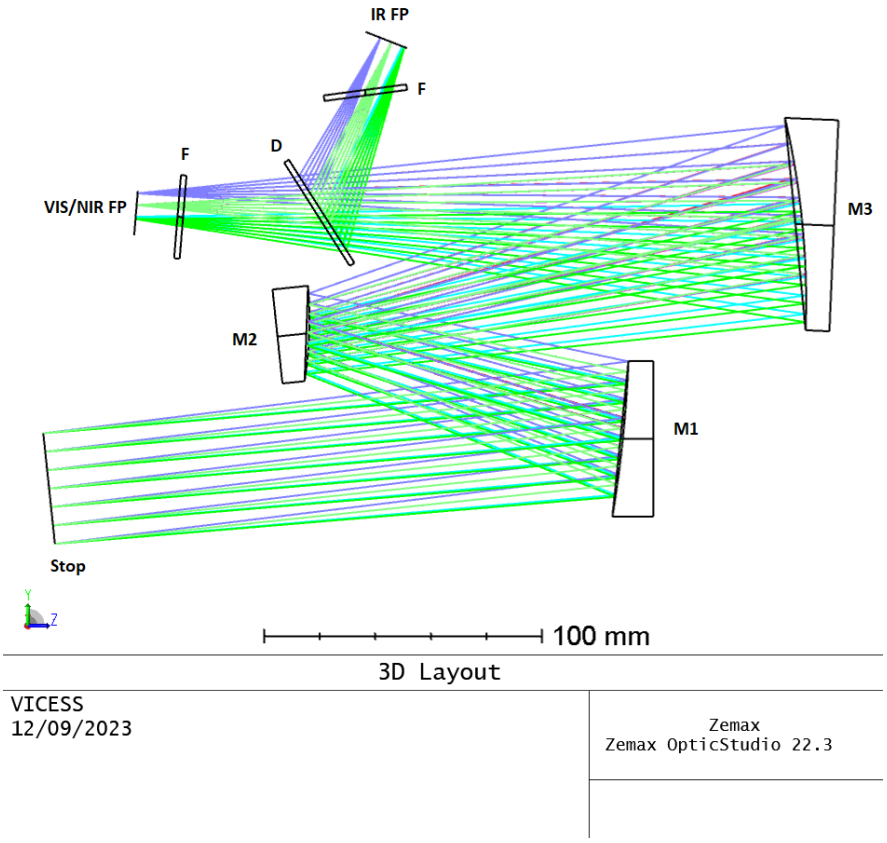

Figure 3.6: VICESS optical layout.

In Figure 3.6 the complete design layout is shown. The instrument is composed by an off-axis, unobscured TMA telescope, where the mirrors (M1, M2 and M3) are off-axis portions of conics. The telescope is able to feed two distinct focal planes (VIS/NIR FP and IR FP) by means of a dichroic filter (D), which is used to selectively pass light of a specific range of wavelengths and reflect another one, while maintaining a nearly zero coefficient of absorption for all wavelengths of interest.
The instrument also comprises two filter-wheel mechanisms (F) to select the band-pass filter most suitable for each observation. The overall envelope of the instrument measures approximately $250 \times 200 \times 100$ mm^3.

Table 3.1 summarises the principal optical parameters required for VICESS to satisfy the assigned scientific mission requirements.

Parameters	Unit	Requirement	Notes
Effective focal length	*mm*	250	-
f/#	-	6.25	-
Aperture	*mm*	40	-
Field of view		3°× 3°	-
Spectral range	*nm*	400-1000	VIS-NIR
		1000-2500	IR
Detector	-	1k × 1k CCD	VIS-NIR
		2k × 1k CCD	IR
Distance	*km*	10	-
Resolution	*m/pixel*	0.5	-

Table 3.1: Main parameters required.

Figures 3.7 and 3.8 show instead the camera performance in terms of Spot Diagram for both the visible and the infrared channel. Spots can be compared to the diffraction limited response, as the Airy disk reference circle is also plotted for each wavelength. The Airy disk radii are reported below the matrix with reference to the first operational wavelength of each configuration. The scale box is set at 13 μm, as the sensor pixel size.

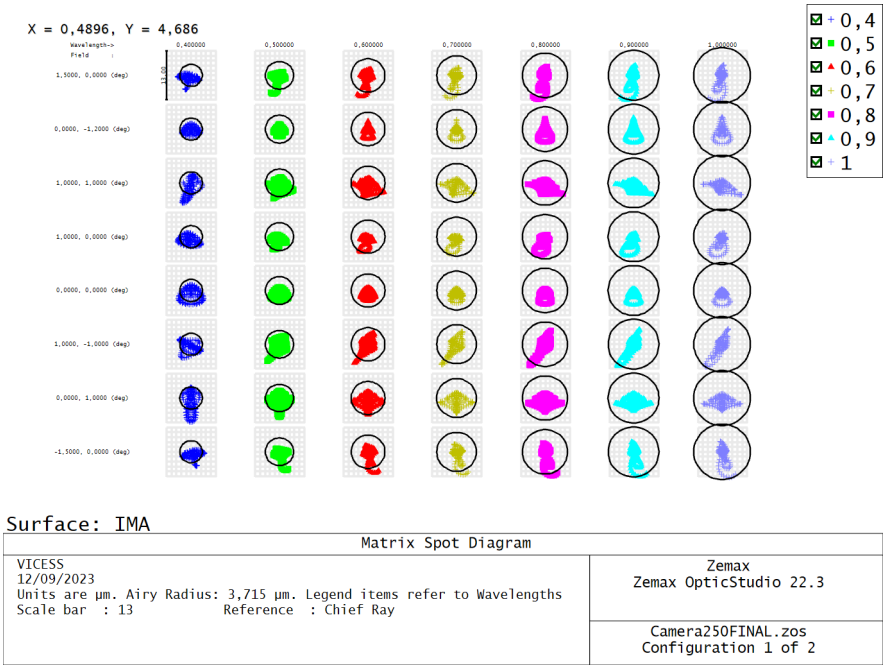

Figure 3.7: Spot Diagram for the VIS/near-IR configuration. The scale bar is set at 13 μm.

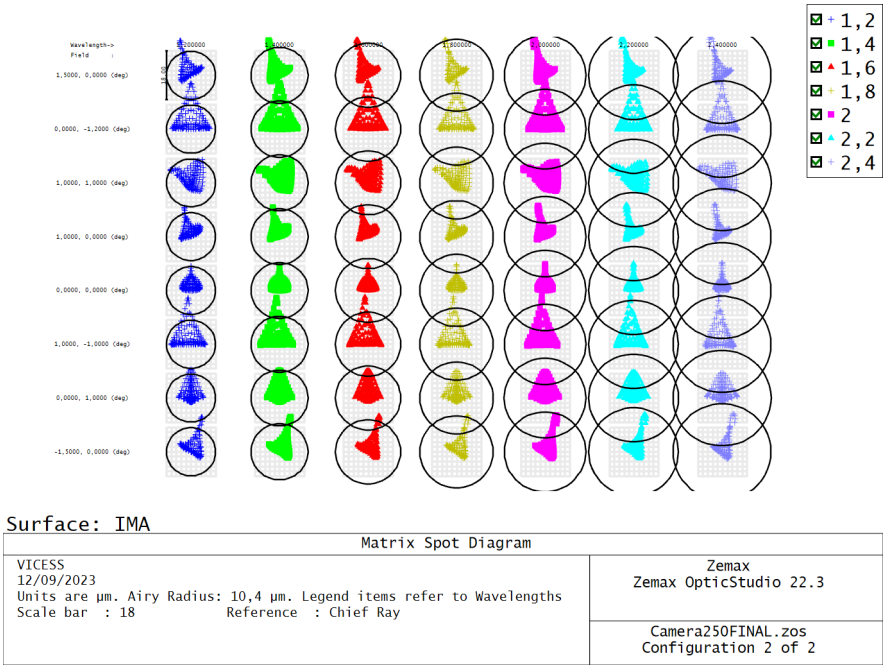

Figure 3.8: Spot Diagram for the IR configuration. The scale bar is set at 18 μm.

3.3.2 The HYPerspectral Stereo Observing System

The second instrument that has been investigated is the HYPerspectral Stereo Observing System (HYPSOS), a small-class instrument compatible with small satellite application and suitable both for planetary or moon exploration or terrestrial environmental monitoring [5]. Remote sensing observations often require to couple the information acquired by an imaging system with the one acquired by a spectroscopic instrument: "patching" the spectral characteristics of an observed region to the corresponding imaging features provides a much larger and more complete set of information than the single instruments themselves. For this reason, it is very common to find both these types of instruments on board of a satellite, in particular for planetary or moon exploration. Often, to get more information, the on-board imaging system has stereoscopic capabilities, that provides data with which is possible to reconstruct a Digital Terrain Model (DTM)[2] of the observed features.

HYPSOS is a novel remote sensing instrument which has simultaneously both stereoscopic and spectroscopic capabilities. It is able to provide a Spectral Digital Terrain Model (SDTM) of the observed region as final product, combining a three dimension spatial information with a spectral one by getting two images of the same target from two different perspectives, and then obtaining the spectrum of each image pixel [5]. The major advantage of HYPSOS is that, being a single optical system, cross-calibration between two different instruments is no longer needed.
In terms of optical design, this translates into having two coupled optical systems: first, the telescope, that is a push-broom[3] stereo-camera, which images the target on the telescope focal plane; then the imaging spectrometer, with its entrance slit located on the telescope focal plane, that provides the spectrum of each projected slit element on a bi-dimensional sensor. A push-broom stereoscopic system can be obtained implementing two push-broom chan-

[2] A Digital Terrain Model is a 3D graphic representation of elevation data to represent the surface of a planet, a moon or an asteroid.

[3] Push-broom is a term related to the possible scanning modes of a spectroscopic sensor. In orbital push-broom sensors, a line of sensitive elements in arranged perpendicularly to the flight direction of the spacecraft, so different areas of the targeted surface are scanned as the spacecraft flies forward

nels instead of one, as can be seen in Figure 3.9. The light beam entering the two channels of the stereo-camera is folded by $\pm 20°$ with respect to nadir by two entrance flat mirrors (EFM) and then rotated by 90° by two 45° tilted Schmidt-Pechan prisms (SPP), in order to obtain a rotated field of view (FoV) at the image plane, as showed in Figure 3.10.

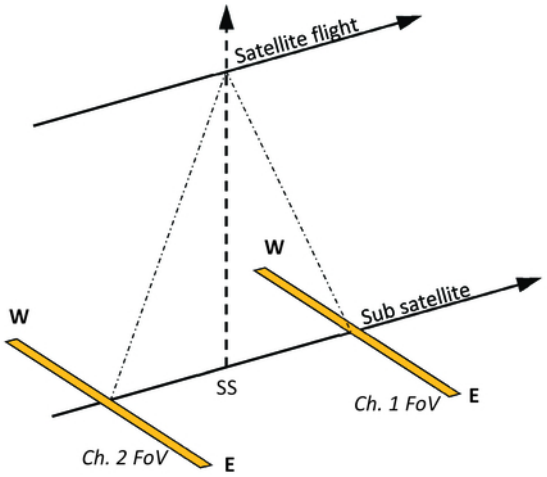

Figure 3.9: Ground projection of the FoVs of a push-broom stereoscopic system [5].

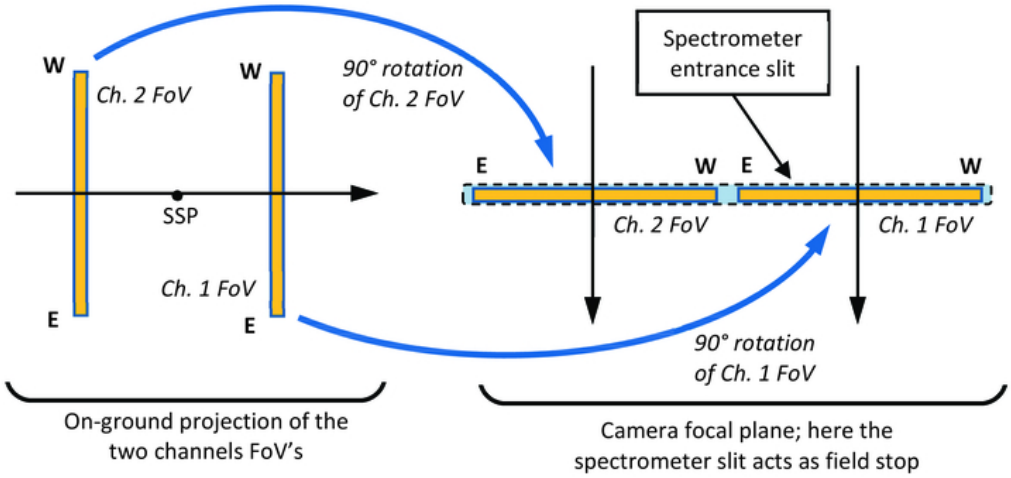

Figure 3.10: On the left, the FoVs on the stereo camera focal plane are shown without the SPP rotators; on the right, the same FoVs are shown when the SPP rotation is considered. Thanks to this rotation, both the channels FoVs are projected on a single entrance slit [5].

The aperture stops of the optical system are two 35 mm diameter circular masks, located at the SPP input faces. The telescope is composed by a TMA, with a 245 mm focal length, and a fourth flat folding mirror (FM). Both channels are imaged onto a double-long slit, located at the telescope focal plane, 22 μm wide and 8 mm long for each channel, with a 1 mm separation between.

Finally, light passing through the slit enters a double-pass imaging spectrometer, composed by four lenses (L1, L2, L3, L4) and a concave, commercial reflection grating (G); the two separate spectra are collected by a bi-dimensional detector (D). Figure 3.11 shows the complete layout of the HYPSOS instrument, while Table 3.2 summarizes the main characteristics of the instrument. The performance, in terms of Spot Diagram, is displayed in Figure 3.12: the nominal spot size at the telescope focus is well below 10 μm over all the useful FoV.

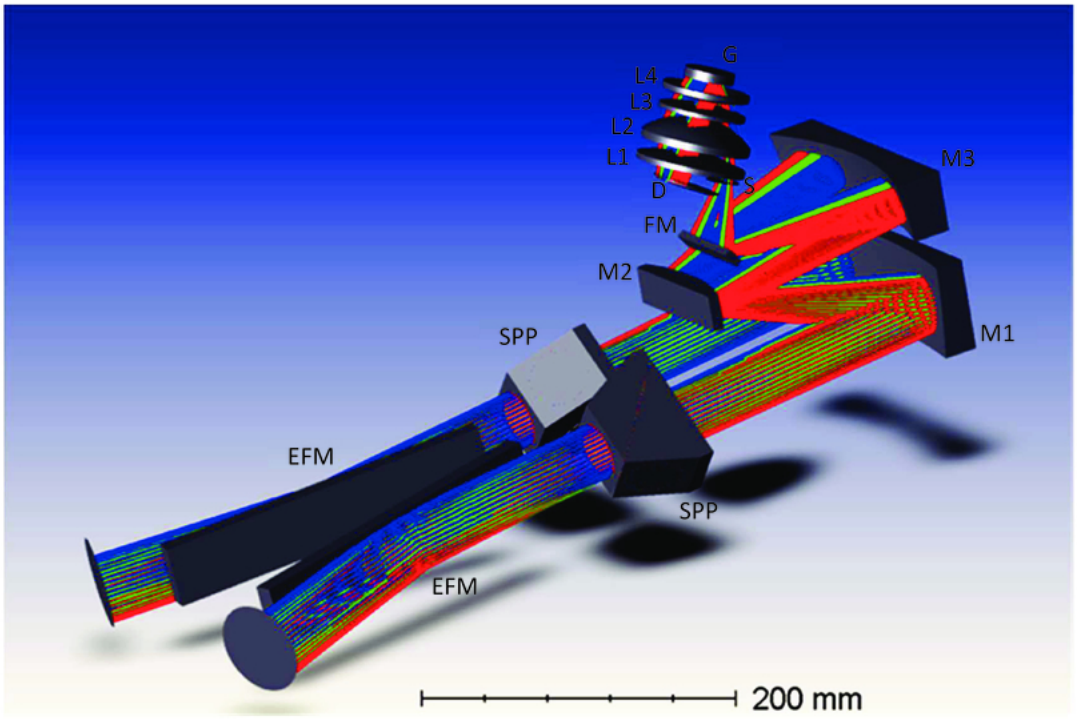

Figure 3.11: Optical layout of the HYPSOS instrument [5].

Parameters	Unit	Requirement	Notes
Effective focal length	mm	245	-
f/#	-	7	-
Aperture	mm	35	-
Field of view		0.00513°× 1.87°	-
Folding angle		± 20°	From Nadir
Spectral range	mm	400-1000	VIS-NIR
Spectral resolution	nm	1.53	-
Slit size	mm	0.022 × 8	-

Table 3.2: Main parameters required.

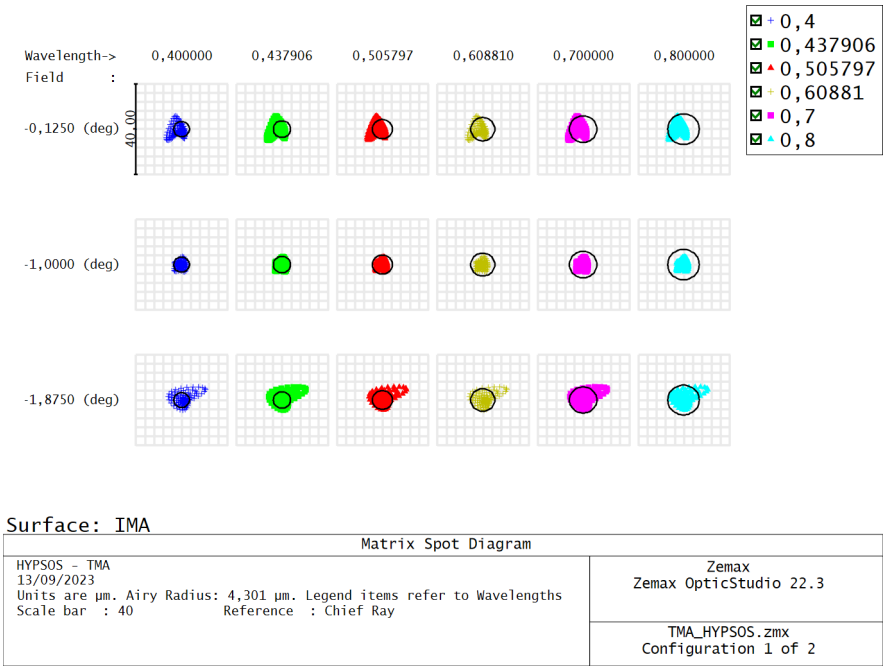

Figure 3.12: Spot Diagram at the entrance slit for one channel. Since the channels are symmetric in their path through the telescope, the Spot Diagram for the other channel is equivalent, but mirrored.

4

Introduction to Freeform Optics

When developing optical systems for space observations, the design is frequently constrained by very stringent requirements on the optical characteristics, the performance of the instrument itself or the overall dimensions. Conventional spherical optics are often no longer sufficient to achieve the desired performance. freeform optical surfaces have the additional degrees of freedom needed to correct the residual aberrations within the optical system, thus pursuing better performances or achieving a more demanding design with regard to specifications, whilst maintaining good performance.

The ultimate goal of this thesis work is therefore to demonstrate how these freeform surfaces might be introduced within the optical systems discussed in Chapter 3 to reach results otherwise inaccessible with traditional optics.

The design of freeform optics is driven by the behaviour of the aberration fields within the system, so the principles of the Nodal Aberration Theory will be firstly introduced for tilted, off-axis systems (such as the TMA telescopes previously discussed) and then extended to freeform surfaces to understand the effect that these surfaces may have on the overall aberration field.

4.1 What is a freeform surface

Freeform surfaces, as their name implies, are free from any constraints of symmetry in their form and shape, as can be seen in Figure 4.1.

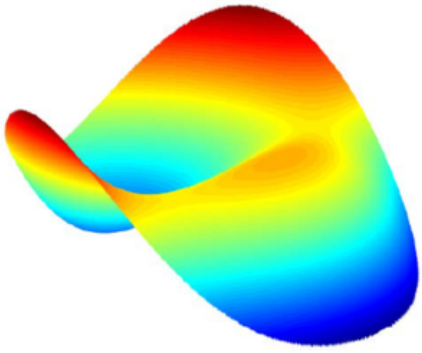

Figure 4.1: A 3D freeform surface [6].

They can be defined as surfaces with no axis of rotational invariance (within or beyond the optical part), as they require and leverage three or more independent axes to create the as-designed asymmetrical features.
One of the most typical examples of a freeform optical surface was used by Maitenaz and Kanolt in progressive multifocal ophthalmic lenses dating back to 1954. It was used to correct presbyopia and offered wearers comfortable, relatively clear vision with no separation between long and short distances. Another example of freeform surfaces used in an off-axis catadioptric Polaroid SX-70 camera was introduced by Plummer; this is believed to be the first commercial product to incorporate optical freeform surfaces [31]. In the last decade, with the development of advanced manufacturing equipment, commercial optical design tools and optical testing technology, the advantages of optical freeform surfaces have been extensively exploited in various applications such as projection optics, illumination systems and off-axis reflective optics. In these applications, the freeform surface used is generally a continuous and smooth surface characterised by various analytical functions. Obviously, the optical freeform surface representation technique adopted in different applications is not

unique and its selection depends on practical considerations. So far, XY-type, Zernike, Q-type, Chebyshev and Legendre polynomials have been used to represent the optical freeform surface in different specific applications [31].

Freeform optics enhances the performance and efficiency of the systems in opto-mechanical and opto-electronic domains. When such surfaces are integrated into the optics, they provide multiple degrees of freedom and the ability to correct off-axis aberrations. The freeform optical component provides advantages over traditional optical components, as follows [32]:

- enhancement of optical performance, such as an expanded field of view and almost aberration-free images;
- quantitative reduction in optical components of systems, leading to a reduction of the overall cost;
- simplified assembly because of few optical components (for example, freeform surfaces fabricated on a single monolithic piece [33]);
- overall reduction of the weight of the optical system and compactness.

4.1.1 Zernike polynomials as surface descriptors

As intuitively displayed in Figure 4.2, a simple way to describe a freeform surface is a decomposition into two major parts: the so called basic shape, that can be a traditional optic surface like a sphere or a conic, and a higher-order polynomial overlay, containing the freeform contribution.

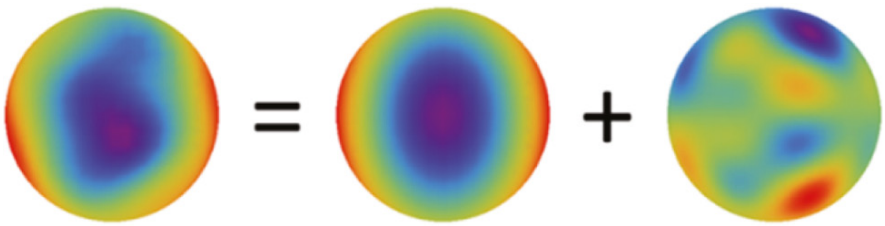

Figure 4.2: Decomposition of sag of a freeform surface into the basic shape plus a higher order deformation [7].

Mathematically, this translates into incorporating a sum of weighted polynomials in the

surface sag equation, as showed in Equation 4.1:

$$z(x,y) = \frac{c\,(x^2+y^2)}{1+\sqrt{1-(1+k)\,c^2(x^2+y^2)}} + \sum_{j=1}^{n} C_j\,P_j(x,y) \tag{4.1}$$

where c is the surface curvature of the basic conical surface, k is its conic constant and C_j and P_j are, respectively, the j^{th} weight factor and the j^{th} polynomial contribution.
For the purpose of this work, the polynomial set that has been chosen to be incorporate as surface descriptor was the Zernike polynomial set.

The Zernike polynomials are a sequence of continuous functions that play important roles in optics, as they are useful for wavefront analysis in optical systems having circular apertures. They were named after the optical physicist Frits Zernike, winner of the 1953 Nobel Prize in Physics and the inventor of phase-contrast microscopy.
The widespread use of these polynomials stems from their unique mathematical properties. First, Zernike polynomials are orthogonal over a unit circle. The orthogonality makes the expansion coefficients of a wavefront function independent of the number of polynomials used in the sequence, meaning that any number of additional terms can be added without impact on those already computed. This also enables convenient mathematical manipulations of wavefronts, such as addition, subtraction, translation, rotation, and scaling. Second, Zernike polynomials have good corresponding relationships with classical aberrations, such as astigmatism, coma, and spherical aberration (see Chapter 7 for further details)[8].

Zernike polynomials over circular pupils are defined over a unit disc and can be most conveniently expressed in polar coordinates (ρ,θ), where ρ is the normalized radial coordinate ($0 \leq \rho \leq 1$) and θ is the polar angle measured counterclockwise from the $+x$ axis ($0 \leq \theta \leq 2\pi$), as shown in Figure 4.3. Polar coordinates ρ and θ can be converted to cartesian coordinates x and y through the trigonometric relations:

$$x = \rho\cos\theta, \quad y = \rho\sin\theta \tag{4.2}$$

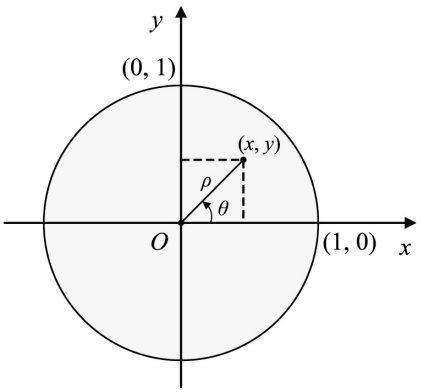

Figure 4.3: Unit circle and polar coordinate system [8].

The polynomial set can be defined and ordered according to different conventions and indexing schemes. For optical design and metrology, the FRINGE indexing is preferred because it groups terms according to optical wavefront aberration order. Under this indices, Zernike polynomials can be defined as:

$$Z_j(\rho,\theta) = Z_n^m(\rho,\theta) = \begin{cases} R_n^{|m|}(\rho)\cos m\theta, & m \geq 0, \\ R_n^{|m|}(\rho)\sin m\theta, & m \leq 0, \end{cases} \tag{4.3}$$

where n is a positive integer, m is an integer, $n - |m| \geq 0$ and even, and j is a mode-ordering number starting from 1. The radial polynomial is expressed as:

$$R_n^{|m|} = \sum_{s=0}^{\frac{n-|m|}{2}} \frac{(-1)^s (n-s)!}{s!\left(\frac{n+|m|}{2}-s\right)!\left(\frac{n-|m|}{2}-s\right)!}\,\rho^n - 2s. \tag{4.4}$$

Defining $N = \frac{n+|m|}{2}$, Zernike FRINGE polynomials can be sorted as follows. First, N is arranged in ascending order from 0 to 6; then, n is sorted in ascending order for a given value of N; finally m is organized in descending order for given values of N and n. Compared with other Zernike sets, the Zernike FRINGE set is unique in the sense that it only has 37 terms ($N \leq 6$). This small polynomial set is useful for interferogram analysis and automatic optical design and is widely adopted in commercial optical software, such as Zemax-OpticStudio. In Table 4.1 the first 16 terms of the FRINGE set, which are the one that has been relevant

j	N	n	m	Z_j	Aberration
1	0	0	0	1	Piston
2	1	1	1	$\rho \sin\theta$	Tilt X
3		1	-1	$\rho \cos\theta$	Tilt Y
4	2	-2		$2\rho^2 - 1$	Defocus
5	2	2	2	$\rho^2 \cos 2\theta$	Astigmatism X
6		2	-2	$\rho^2 \sin 2\theta$	Astigmatism Y
7		3	1	$(3\rho^3 - 2\rho)\cos\theta$	Coma X
8		3	-1	$(3\rho^3 - 2\rho)\sin\theta$	Coma Y
9		4	0	$6\rho^4 - 6\rho^2 + 1$	Primary spherical
10	3	3	3	$\rho^3 \cos 3\theta$	Trefoil X
11		3	-3	$\rho^3 \sin 3\theta$	Trefoil Y
12		4	2	$(4\rho^4 - 3\rho^2)\cos 2\theta$	Secondary X astigmatism
13		4	-2	$(4\rho^4 - 3\rho^2)\sin 2\theta$	Secondary Y astigmatism
14		5	1	$(10\rho^5 - 12\rho^3 + 3\rho)\cos\theta$	Secondary X coma
15		5	-1	$(10\rho^5 - 12\rho^3 + 3\rho)\sin\theta$	Secondary Y coma
16		6	0	$20\rho^6 - 30\rho^4 + 12\rho^2 - 1$	Secondary spherical

Table 4.1: First sixteen Zernike FRINGE polynomial terms.

when optimizing the design, are computed. Figure 4.4 shows instead a 2D plot of the same polynomials.

4.2 The Nodal Aberration Theory for tilted, off-axis systems

The wavefront expansion and surface contributions describing the imaging properties of an optical system have traditionally assumed rotational symmetry. In this case, the third order aberrations are the sum of the individual surface contributions. However, symmetry is dis-

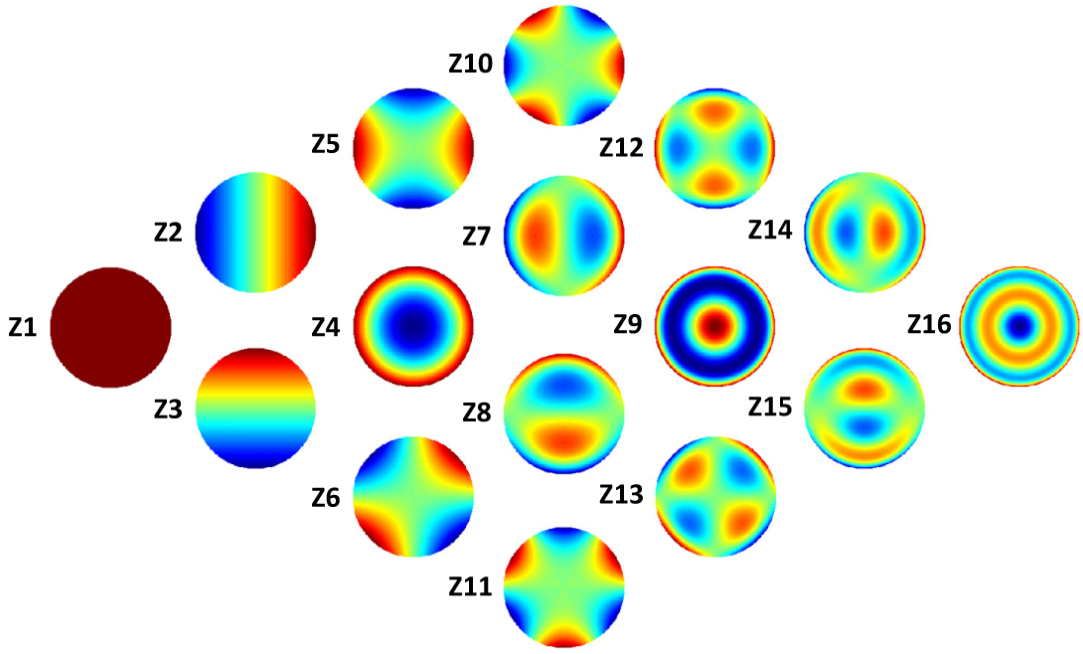

Figure 4.4: 2D plot pf the first sixteen Zernike polynomials according to the FRINGE indexing [9].

rupted in unobscured reflective systems by tilting the optical components or offsetting the aperture. The Nodal Aberration Theory represents the crucial novel framework capable of dealing with the imaging characteristics of non-symmetrical optical systems.

4.2.1 The wavefront aberration expansion

In addition to the diffraction effect caused by a finite aperture, the resolution of an optical systemis limited by the deviation from geometric idealisation. The Gaussian model typically describes the geometric transformation of a point between image and object planes. In this model each ray originating from the object plane passes through the entrance and exit pupil planes, which represent the transformation performed by an optical system, and intersects the image plane at the scaled coordinates [34]. Thus, in a centered, rotationally symmetric system, each ray can be described using two coordinates: the field coordinate H, located at the object or at the image plane, the pupil coordinate ρ and the azimuthal coordinate ϕ, located at the pupil plane. In the approximation of the first order, each ray originating from

a point in the object arrives at a scaled point in the image, travelling an optical path of the same length measured in the exit pupil. The Optical Path Length (OPL) of a ray s, through the arbitrary points P_0 and P_1 in a medium with refractive index n, is defined as:

$$OPL = \int_{P_0}^{P_1} nds. \tag{4.5}$$

The surface of equal OPLs is a wavefront. An ideal wavefront is a spherical or plane surface that converges (diverges) to (from) a point or infinity at the image plane.
However, the real imagery of an optical system deviates from ideal geometric transformation, as aberrations occur. Therefore, an aberrated wavefront deviates from the ideal shape. The measure of this deviation in the image space is the total wave aberration, which can be defined as a function of the field and pupil coordinates: $W = W(H, \rho, \phi)$. A common way to express the wavefront aberration function is through the expansion originally proposed by Hopkins [35], as shown in Equation 4.6:

$$W = \sum_j \sum_p^{\infty} \sum_n^{\infty} \sum_m^{\infty} (W_{klm})_j H^k \rho^l \cos\phi^m \tag{4.6}$$

with $k = 2p + m, l = 2n + m$. W is the total wave aberration, as sum of all the individual surface contributions j, H is the normalized field coordinate, ρ is the normalized pupil coordinate, and ϕ is the azimuthal coordinate in the pupil. The scalar expression assumes rotational symmetry within the optical system, so only terms containing powers of H^2,ρ^2 and $H\rho\cos\phi$ are allowed. If Equation 4.6 is expanded through third order (fourth order in wavefront), W takes the form:

$$\begin{aligned} W = \Delta W_{20}\rho^2 + \Delta W_{11} H\rho\cos\phi + W_{040}\rho^4 + \\ + W_{131} H\rho^3\cos\phi + W_{222} H^2\rho^2\cos\phi^2 + \\ + W_{220} H^2\rho^2 + W_{311} H^3\rho\cos\phi, \end{aligned} \tag{4.7}$$

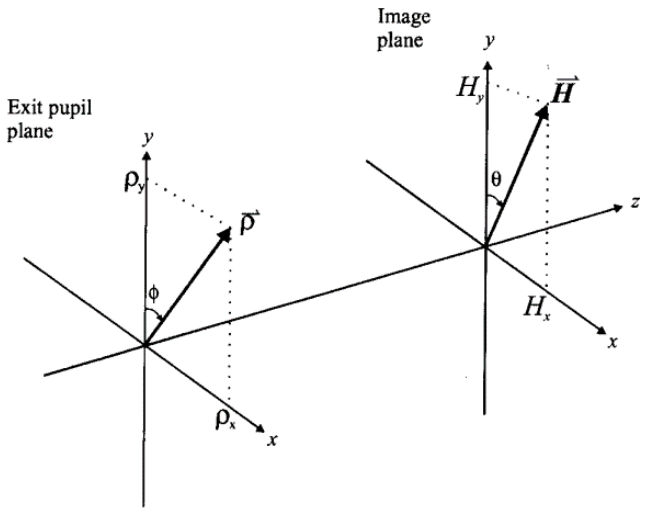

Figure 4.5: Conventions for field vector $\vec{H}$ and pupil vector $\vec{\rho}$ [10].

where

$$W_{klm} = \sum_j (W_{klm})_j. \tag{4.8}$$

The terms in Equation 4.7 are, respectively, defocus, tilt, spherical aberration, coma, astigmatism, sagittal field curvature and distortion. The different notation in the coefficients of defocus and tilt is due to the fact that these aberrations can be balanced by directly shifting or tilting the Focal Plane, hence the notation ΔW. This scalar expression assumes that the aberrations at the image plane are rotationally symmetric with respect to field dependence, and thus can be represented as a height along the y-axis at the image plane.

The initial, fundamental step in formulating an all-encompassing theory on aberration that does not depend on symmetry is to shift both the pupil position and field position coordinates to vectors, in accordance with the conventions provided in Figure 4.5:

$$\vec{H} = He^{i\theta},\ \vec{\rho} = \rho e^{i\phi}. \tag{4.9}$$

Therefore, the resulting expression for the wavefront expansion is:

$$W = \sum_{j} \sum_{p}^{\infty} \sum_{n}^{\infty} \sum_{m}^{\infty} (W_{klm})_j \, (\vec{H} \cdot \vec{H})^p (\vec{\rho} \cdot \vec{\rho})^n (\vec{H} \cdot \vec{\rho})^m. \tag{4.10}$$

4.2.2 Aberration field centers

The behavior of the aberration fields in a misaligned system or a system designed without an axis of symmetry is based on fundamental observations attributed to Buchroeder [36].
As was previously stated in Equation 4.6, the aberrations of an optical system, assumed by Hopkins [35] to be rotationally symmetric, are the sum of the individual surface contributions. Buchroeder demonstrated that in an optically misaligned or asymmetric design, the aberration field at the image plane still results from the sum of individual surface contributions of the conventional, rotationally symmetric form for spherical or aspheric surfaces, but is no longer null in correspondence of the optical axis. Therefore, a perturbed system with a circular pupil will not generate new aberrations, but instead, the aberration field's behavior at the image plane will be altered, revealing a nodal behavior. Precisely, the total exit pupil aberration function at any field point is still given by the sum of all surface contributions, but accounting for the fact that the centers of the aberration field contributions for each surface no longer coincide.

To establish the mathematical theory of aberrations based on this insight, the Nodal Aberration Theory (NAT), Buchroeder [36] introduced a vector $\vec{\sigma}_j$ (see [37] for further details on the computation of the vector), which points from the center of the image plane to the center of the aberration field of a specific surface, projected into the image plane. This vector indicates the displacement of the aberration field W_j of surface j with respect to the unperturbed field center (center of the Gaussian image plane), which is located by the optical axis ray. The latter is a real ray (i.e traced without making the paraxial approximation), dependent on the configuration of the system, that starts from the centre of the object field and passes through the aperture stop centre. This ray links the pupils' centres of all surfaces with

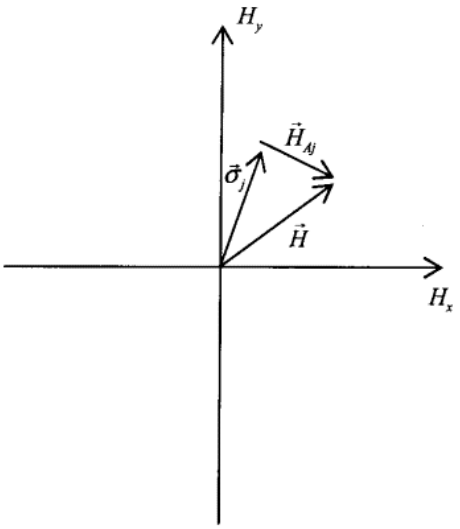

Figure 4.6: Representation of the effective field height vector, $\vec{H}_{Aj}$ [10].

the object and the images produced by all the surfaces.

In a system without symmetry, the aberration field related to each surface is usually centered at a different point in the image, specified by the vector $\vec{\sigma}_j$. This point in the image plane is the projection of a line connecting the center of the pupil (which is influenced by the optical system configuration) for the surface of interest with the center of curvature of that surface to the image plane (which is unaffected by the system but determined by the surface's misalignment and placement).

To calculate the extent to which a surface contributes to the overall aberration field, it is essential to determine the surface's effective height within the aberration field $\vec{H}_{Aj}$, which is represented in Figure 4.6 and given by:

$$\vec{H}_{Aj} = \vec{H} - \vec{\sigma}_j \tag{4.11}$$

With the new concept that every surface of an optical system creates a traditional, rotationally symmetrical aberration field with a unique center of symmetry in the image plane, it is now feasible to formulate a new expression for the wave aberrations of an optical system comprised of displaced and titled surfaces, without restriction. This is accomplished by sim-

ply replacing the rotationally symmetric field vector $\vec{H}$ in Equation 4.10 with the effective aberration field height of each surface, $\vec{H}_{Aj}$:

$$\begin{aligned} W &= \sum_j \sum_p^{\infty} \sum_n^{\infty} \sum_m^{\infty} (W_{klm})_j \, (\vec{H}_{Aj} \cdot \vec{H}_{Aj})^p (\vec{\rho} \cdot \vec{\rho})^n (\vec{H}_{Aj} \cdot \vec{\rho})^m = \\ &= \sum_j \sum_p^{\infty} \sum_n^{\infty} \sum_m^{\infty} (W_{klm})_j \left[(\vec{H} - \vec{\sigma}) \cdot (\vec{H} - \vec{\sigma}) \right]^p (\vec{\rho} \cdot \vec{\rho})^n \left[(\vec{H} - \vec{\sigma}) \cdot \vec{\rho} \right]^m . \end{aligned} \tag{4.12}$$

At this point, it is useful to expand Equation 4.12 through fifth order (see [37]):

$$\begin{aligned} W = {} & \Delta W_{20} (\vec{\rho} \cdot \vec{\rho}) + \Delta W_{11} (\vec{H} \cdot \vec{\rho}) + \sum_j W_{040_j} (\vec{\rho} \cdot \vec{\rho})^2 + \\ & + \sum_j W_{131_j} \left[(\vec{H} - \vec{\sigma}_j) \cdot \vec{\rho} \right] (\vec{\rho} \cdot \vec{\rho}) + \sum_j W_{220M_j} \left[(\vec{H} - \vec{\sigma}_j) \cdot (\vec{H} - \vec{\sigma}_j) \right] (\vec{\rho} \cdot \vec{\rho}) + \\ & + \frac{1}{2} \sum_j W_{222_j} \left[(\vec{H} - \vec{\sigma}_j)^2 \cdot \vec{\rho}^2 \right] + \sum_j W_{311_j} \left[(\vec{H} - \vec{\sigma}_j) \cdot (\vec{H} - \vec{\sigma}_j) \right] \left[(\vec{H} - \vec{\sigma}_j) \cdot \vec{\rho} \right] + \\ & + \sum_j W_{060_j} (\vec{\rho} \cdot \vec{\rho})^3 + \sum_j W_{151_j} \left[(\vec{H} - \vec{\sigma}_j) \cdot \vec{\rho} \right] (\vec{\rho} \cdot \vec{\rho})^2 + \\ & + \sum_j W_{240M_j} \left[(\vec{H} - \vec{\sigma}_j) \cdot (\vec{H} - \vec{\sigma}_j) \right] (\vec{H} \cdot \vec{\rho})^2 + \\ & + \frac{1}{2} \sum_j W_{242_j} \left[(\vec{H} - \vec{\sigma}_j)^2 \cdot \vec{\rho}^2 \right] (\vec{\rho} \cdot \vec{\rho}) + \\ & + \sum_j W_{331M_j} \left[(\vec{H} - \vec{\sigma}_j) \cdot (\vec{H} - \vec{\sigma}_j) \right] \left[(\vec{H} - \vec{\sigma}_j) \cdot \vec{\rho} \right] (\vec{H} \cdot \vec{\rho}) + \\ & + \frac{1}{4} \sum_j W_{333_j} \left[(\vec{H} - \vec{\sigma}_j) \cdot \vec{\rho}^3 \right] + \sum_j W_{420M_j} \left[(\vec{H} - \vec{\sigma}_j) \cdot (\vec{H} - \vec{\sigma}_j) \right]^2 (\vec{\rho} \cdot \vec{\rho}) + \\ & + \frac{1}{2} \sum_j W_{422_j} \left[(\vec{H} - \vec{\sigma}_j) \cdot (\vec{H} - \vec{\sigma}_j) \right] \left[(\vec{H} - \vec{\sigma}_j)^2 \cdot \vec{\rho}^2 \right] + \\ & + \sum_j W_{511_j} \left[(\vec{H} - \vec{\sigma}_j) \cdot (\vec{H} - \vec{\sigma}_j) \right]^2 \left[(\vec{H} - \vec{\sigma}_j) \cdot \vec{\rho} \right] . \end{aligned} \tag{4.13}$$

Subscripts M, in Equation 4.13, and S, which will be found in the next pages, denote the medial and the sagittal focal surfaces (see Chapter 7 for more details).
Table 4.2 displays a set of naming conventions commonly used in optical design to refer to the terms of the wavefront expansion in Equation 4.13.

H^k	ρ^l	$\cos\phi^m$	Coeff.	Aberration name
	2	0	ΔW_{20}	Defocus
	1	1	ΔW_{11}	Tilt
				4^{th} Order Wave Aberration Type
0	4	0	W_{040}	3^{rd} order spherical aberration
1	3	1	W_{131}	3^{rd} order coma
2	2	0	W_{220S}	3^{rd} order sagittal focal surface
2	2	2	W_{222}	3^{rd} order astigmatism
3	1	1	W_{311}	3^{rd} order distortion
				6^{th} Order Wave Aberration Type
0	6	0	W_{060}	5^{th} order spherical aberration
1	5	1	W_{151}	5^{th} order field linear coma
2	4	0	W_{240S}	5^{th} order sagittal focal surface for oblique sph. ab.
2	4	2	W_{242}	5^{th} order oblique spherical aberration
3	3	1	W_{222}	5^{th} order field cubic coma
3	3	3	W_{331}	5^{th} order elliptical coma
4	2	0	W_{420S}	5^{th} order sagittal focal surface
4	2	2	W_{422}	5^{th} order astigmatism
5	1	1	W_{511}	5^{th} order distortion

Table 4.2: Names of the aberration terms from the wavefront expansion up to fifth order (sixth order in wavefront).

Other useful relations are reported in Equation 4.14, where the coefficients related to the sagittal focal surface, in the Hopkins notation, are expressed as a function of other coefficients related to the medial focal surface.

$$
\begin{aligned}
W_{220M} &= W_{220S} + \frac{1}{2} W_{222}, \\
W_{240M} &= W_{240S} + \frac{1}{2} W_{242}, \\
W_{331M} &= W_{331} + \frac{3}{4} W_{333}, \\
W_{420M} &= W_{420S} + \frac{1}{2} W_{422},
\end{aligned}
\tag{4.14}
$$

To simplify the overall notation, the relations in Equation 4.15 are introduced:

$$
\begin{aligned}
\vec{A}_{klm} &= \sum_j W_{klm_j} \vec{\sigma}_j \\
B_{klm} &= \sum_j W_{klm_j} (\vec{\sigma}_j \cdot \vec{\sigma}_j) \\
\vec{B}^2_{klm} &= \sum_j W_{klm_j} \vec{\sigma}_j^2 \\
\vec{C}_{klm} &= \sum_j W_{klm_j} (\vec{\sigma}_j \cdot \vec{\sigma}_j) \vec{\sigma}_j \\
\vec{C}^3_{klm} &= \sum_j W_{klm_j} \vec{\sigma}_j^3 \\
D_{klm} &= \sum_j W_{klm_j} (\vec{\sigma}_j \cdot \vec{\sigma}_j)^2 \\
\vec{D}^2_{klm} &= \sum_j W_{klm_j} (\vec{\sigma}_j \cdot \vec{\sigma}_j) \vec{\sigma}_j^2 \\
\vec{E}_{klm} &= \sum_j W_{klm_j} (\vec{\sigma}_j \cdot \vec{\sigma}_j)^2 \vec{\sigma}_j,
\end{aligned}
\tag{4.15}
$$

and then incorporated in Equation 4.13 as follows:

$$
\begin{aligned}
W = \Delta W_{20}(\vec{\rho}\cdot\vec{\rho}) + \Delta W_{11}(\vec{H}\cdot\vec{\rho}) + W_{040}(\vec{\rho}\cdot\vec{\rho})^2 + \Big[(W_{131}\vec{H} - \vec{A}_{131})\cdot\vec{\rho}\Big](\vec{\rho}\cdot\vec{\rho}) + \\
+\Big[W_{220M}(\vec{H}\cdot\vec{H}) - 2(\vec{H}\cdot\vec{A}_{220M}) + B_{220M}\Big](\vec{\rho}\cdot\vec{\rho}) + \\
+\frac{1}{2}\Big[W_{222}\vec{H^2} - 2\vec{H}\vec{A}_{222} + \vec{B^2}_{222}\Big]\cdot\vec{\rho^2} + \\
+\Big[W_{311}(\vec{H}\cdot\vec{H})\vec{H} - 2(\vec{H}\cdot\vec{A}_{311})\vec{H} + 2B_{311}\vec{H} - (\vec{H}\cdot\vec{H})\vec{A}_{311} + \vec{B^2}_{311}\vec{H}^* - \vec{C}_{311}\Big]\cdot\vec{\rho} + \\
+W_{060_j}(\vec{\rho}\cdot\vec{\rho})^3 + \Big[(W_{151}\vec{H} - \vec{A}_{151}\cdot\vec{\rho})\Big](\vec{\rho}\cdot\vec{\rho})^2 + \\
+\Big[W_{240M}(\vec{H}\cdot\vec{H}) - 2(\vec{H}\cdot\vec{A}_{240M}) + B_{240M}\Big](\vec{\rho}\cdot\vec{\rho})^2 + \\
+\frac{1}{2}\Big[(W_{242}\vec{H^2} - 2\vec{H}\vec{A}_{242} + \vec{B^2}_{242})\cdot\vec{\rho})^2\Big](\vec{\rho}\cdot\vec{\rho}) + \\
+\Bigg(\Big[W_{331M}(\vec{H}\cdot\vec{H})\vec{H} - 2(\vec{H}\cdot\vec{A}_{331M})\vec{H} + 2B_{331M}\vec{H} - (\vec{H}\cdot\vec{H})\vec{A}_{331M} + \\
+\vec{B^2}_{331M}\vec{H}^* - C_{331M}\Big]\cdot\vec{\rho}\Bigg)(\vec{\rho}\cdot\vec{\rho}) + \\
+\frac{1}{4}\Big[W_{333}\vec{H^3} - 3\vec{H^2}\vec{A}_{333} + 3\vec{H}\vec{B^2}_{333} - \vec{C^3}_{333}\Big]\cdot\vec{\rho^3} + \\
+\Big[W_{420M}(\vec{H}\cdot\vec{H})(\vec{H}\cdot\vec{H}) - 4(\vec{H}\cdot\vec{H})(\vec{H}\cdot\vec{A}_{420M}) + 4B_{420M}(\vec{H}\cdot\vec{H}) + \\
+2(\vec{H^2}\cdot\vec{B^2}_{420M}) - 4(\vec{H}\cdot\vec{C}_{420M}) + \vec{D}_{420M}\Big](\vec{\rho}\cdot\vec{\rho}) + \\
+\frac{1}{2}\Big[W_{422}(\vec{H}\cdot\vec{H})\vec{H^2} - 2(\vec{H}\cdot\vec{H})\vec{H}\vec{A}_{422} + 3(\vec{H}\cdot\vec{H})\vec{B^2}_{422} - 2(\vec{H}\cdot\vec{A}_{422})\vec{H^2} - \\
-\vec{C^3}_{422}\vec{H}^* + 3B_{422}\vec{H^2} - 3\vec{H}\vec{C}_{422} + \vec{D^2}_{422}\Big]\cdot\vec{\rho^2} + \\
+\Big[W_{511}(\vec{H}\cdot\vec{H})(\vec{H}\cdot\vec{H})\vec{H} - 4(\vec{H}\cdot\vec{H})\vec{H}\cdot\vec{A}_{511}\vec{H} + 6B_{511}(\vec{H}\cdot\vec{H})\vec{H} + \\
+2(\vec{H^2}\cdot\vec{B^2}_{511})\vec{H} - 4(\vec{H}\cdot\vec{C}_{511})\vec{H} + 3D_{511}\vec{H} - (\vec{H}\cdot\vec{H})(\vec{H}\cdot\vec{H})\vec{A}_{511} + \\
+2(\vec{H}\cdot\vec{H})\vec{B^2}_{511}\vec{H}^* - 4(\vec{H}\cdot\vec{H})\vec{C}_{511} - \vec{H^2}\vec{C^*}_{511} - \vec{C^3}_{511}\vec{H^{2*}} + 2\vec{D^2}_{511}\vec{H}^* - \vec{E}_{511}\Big]\cdot\vec{\rho}.
\end{aligned}
\tag{4.16}
$$

4.2.3 Third order aberrations in optical systems without rotational symmetry

NAT deals with how the shifted, but overlapping, aberration patterns combine to form the resultant aberration field for the entire system. Since the field aberrations are characterised by magnitudes and associated orientations, the shifted contribution must be summed vectorially, and each aberration type should vanish at a number of distinct nodes in the image field, according to the order of the field dependence for the particular aberration [38].

Starting with Equation 4.13 written through third order, the characteristic field behaviour of third order spherical aberration, coma and astigmatism in a system without symmetry can be derived. The result is that each aberration has a unique "signature" field behavior.

- **Spherical aberration**. This aberration is not affected by breaking rotational symmetry, as it does not depend on the field vector $\vec{H}$ and is therefore unaffected by the only substitution required for invoking non-rotational symmetry. As a result, we can simply write that the non-symmetric wave aberration term for third-order spherical aberration is the rotationally symmetric term:

$$W = \sum_j W_{040_j} (\vec{\rho} \cdot \vec{\rho})^2. \tag{4.17}$$

- **Coma**. A misaligned (or non-symmetric) optical system displays on axis coma: it still has a point in the field where coma is null, but this point is no longer at the center of the image field. To demonstrate this by using NAT, the coma term from Equation 4.13 has to be isolated:

$$\begin{aligned} W &= \sum_j W_{131_j} \Big[(\vec{H} - \vec{\sigma}_j) \cdot \vec{\rho} \Big] (\vec{\rho} \cdot \vec{\rho}) = \\ &= \left\{ \left[\left(\sum_j W_{131_j} \vec{H} \right) - \left(\sum_j W_{131_j} \vec{\rho}_j \right) \right] \cdot \vec{\rho} \right\} (\vec{\rho} \cdot \vec{\rho}). \end{aligned} \tag{4.18}$$

The first summation results in simply the contribution of the rotationally symmetric system,

$$\sum_j W_{131_j}\vec{H} = W_{131}\vec{H}. \tag{4.19}$$

The second term is the sum of the various displacement vectors in the image plane, each weighted by the corresponding surface contribution to third order coma. This summation results in a net, un-normalized vector in the image plane:

$$\vec{A}_{131} = \sum_j W_{131}\vec{\sigma}_j. \tag{4.20}$$

Defining a normalized vector,

$$\vec{a}_{131} = \frac{\vec{A}_{131}}{W_{131}}, \tag{4.21}$$

gives the final description of the field dependence of the third order coma:

$$W = W_{131}[(\vec{H} - \vec{a}_{131}) \cdot \vec{\rho}](\vec{\rho} \cdot \vec{\rho}). \tag{4.22}$$

It is clear that for this aberration, which depends linearly on field of view, the aberration field is completely unchanged except that it can become decentered from the center of the image field. The new point of rotational symmetry in the field for the third-order coma in the image field is determined by the coma field displacement vector $\vec{a}_{131}$ as illustrated in Figure 4.7.

In a system that is corrected for third order coma, the introduction of asymmetry will result in an optical system in which the third order coma is constant in both magnitude and direction over the field of view.

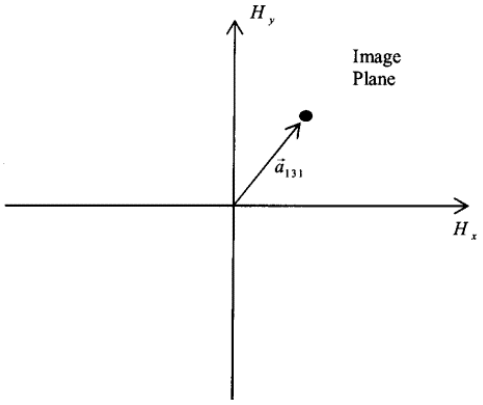

Figure 4.7: Displacement of the node for coma [10].

- **Astigmatism**. The expression for the field behavior of astigmatism with respect to the medial surface in an optical system without symmetry is extrapolated from Equation 4.13:

$$\begin{aligned} W = \frac{1}{2}\sum_j W_{222_j}\left[(\vec{H} - \vec{\sigma^2}_j)\cdot\vec{\rho^2}\right] = \\ = \frac{1}{2}\left[\sum_j W_{222_j}\vec{H^2} - 2\vec{H}\left(\sum_j W_{222_j}\vec{\sigma}_j\right) + \sum_j W_{222_j}\vec{\sigma^2}_j\right]\cdot\vec{\rho^2}. \end{aligned} \tag{4.23}$$

As previously done with coma, two un-normalized displacement vectors are defined:

$$\begin{aligned} \vec{A}_{222} &= \sum_j W_{222_j}\vec{\sigma}_j; \\ \vec{B^2}_{222} &= \sum_j W_{222_j}\vec{\sigma}_j^2. \end{aligned} \tag{4.24}$$

The normalized corresponding set is then:

$$\begin{aligned} \vec{a}_{222} &= \frac{\vec{A}_{222}}{W_{222}}; \\ \vec{b^2}_{222} &= \frac{\vec{B^2}_{222}}{W_{222}} - \vec{a^2}_{222}. \end{aligned} \tag{4.25}$$

which allows to write the characteristic field dependence for astigmatism in optical systems without symmetry:

$$W = \frac{1}{2} W_{222}[(\vec{H} - \vec{a}_{222})^2 + \vec{b^2}_{222}] \cdot \vec{\rho}^2. \tag{4.26}$$

This expression for the field behavior of astigmatism includes terms that are squared vectors. To complete the fundamental understanding of the astigmatic aberration field in optical systems without symmetry, it remains to simply solve Equation 4.26 for locations where the astigmatic terms go to zero. This means solving:

$$0 = (\vec{H} - \vec{a}_{222})^2 + \vec{b}^2_{222} \tag{4.27}$$

for $\vec{H}$. Working directly with complex numbers, this is done as if these were scalar quantities, giving:

$$\vec{H} = \vec{a}_{222} \pm \sqrt{-\vec{b}^2_{222}} = \vec{a}_{222} \pm i\vec{b}_{222} \tag{4.28}$$

The astigmatic aberration field in a system without symmetry will, in the general case, contain two zeros, or nodes, neither of which is necessarily located on the optical axis ray, located as illustrated in Figure 4.8.

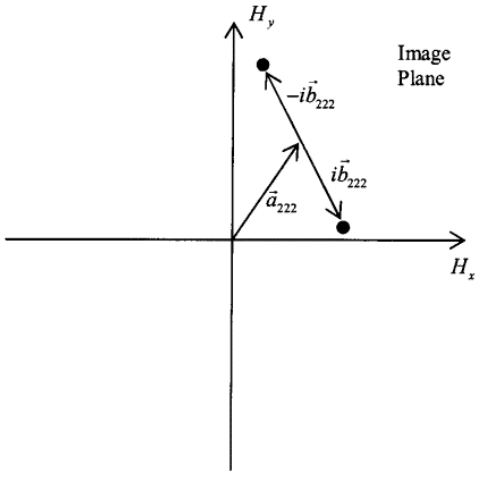

Figure 4.8: Displacement of the nodes for astigmatism [10].

4.2.4 The Full Field Aberration plot

Aberrations only require assessment in one field direction (traditionally, the $+y$ field) in a centred optical system with rotationally symmetric components. Once aberrations are known in this direction, they are known in all other field directions due to their rotational symmetry. However, if the symmetry is disrupted, the plot becomes insufficient as the aberrations are unknown for each field direction. A two-dimensional field plot would be more advantageous in computing aberrations. The Full Field Display (FFD) computes aberrations over a two-dimensional grid of field points by performing a Zernike polynomial fit to the wavefront at the exit pupil. The plot presents these aberrations using symbols to represent their magnitude and orientation at a particular field point. This analysis can be particularly useful on systems containing freeform surfaces to verify aberration correction across the specified field. Given a pair of Zernike coefficient Z_b and Z_k associated to a specific aberration, the magnitude and orientation at each field point can be computed as:

$$\text{Magnitude: } |Z_{b,k}| = \sqrt{Z_b^2 + Z_k^2}$$
$$\text{Angle: } \alpha = \arctan 2\left(\frac{-Z_k}{-Z_b}\right).$$

As an example of the FFD, Figure 4.9 displays the Zernike pair for astigmatism ($Z_{5,6}$), over a Field of View of $1° \times 1°$, for a centered optical system, so only field quadratic astigmatism is present, and for a perturbed system, which gives rise to a binodal response.

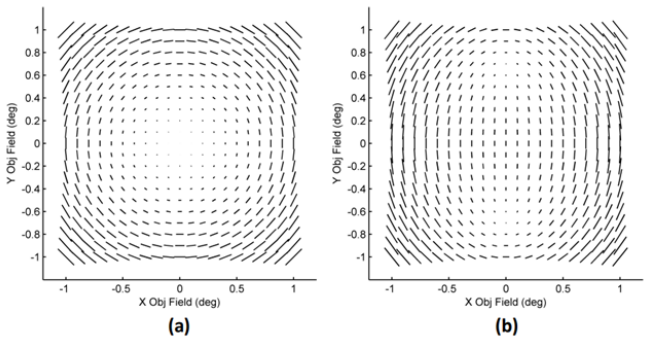

Figure 4.9: Full Field Display showing: a) third order, field quadratic astigmatism, b) binodal astigmatism [11].

4.3 Extending the Nodal Aberration Theory to freeform optics

At this stage, the Nodal Aberration Theory, developed for the aberration fields of non-symmetric optical systems, is extended to freeform surfaces. With this extension, the nodes of the aberration contributions, which are distributed throughout the FoV, can be targeted directly for the correction or control of the aberrations in an optical system with freeform surfaces. The examined freeform surface is defined by a conic plus a Zernike FRINGE polynomial overlay, with the sag that depends on both radial component ρ and azimuthal component ϕ within the aperture of the surface, as previously discussed in Section 4.1.1. Importantly, the freeform overlay placement within the optical imaging system is unrestricted. Under these general conditions, the freeform surface contributes both terms that are field constant and terms that are field dependent to the net aberration field of the optical system. For each term in the Zernike FRINGE set, the aberration behavior throughout the field is examined. Integrating these polynomial freeform overlay into NAT does not introduce new forms of field dependence; rather, the freeform parameters link directly with the terms presented for the generally multinodal field dependence of the sixth order wavefront aberrations derived for tilted and decentered rotationally symmetric surfaces.

4.3.1 Nodal Aberration Theory for freeform surfaces away from the Aperture Stop

To analyze the effect of a freeform optical surface away from the stop on the overall aberration field, a Schmidt telescope set-up is initially considered. The Field of View is restricted to make only third order aberrations significant. The telescope includes a rotationally symmetrical, third order, aspheric corrector plate situated at the mechanical aperture, which acts as the system's stop, at the center of curvature of a spherical mirror (see Figure 4.10).

Placing the stop at the center of curvature of the spherical mirror corrects third order coma and astigmatism. Additionally, by incorporating an aspheric corrector plate at the stop surface, the beam footprint on the plate remains the same for all field points. As a result, the

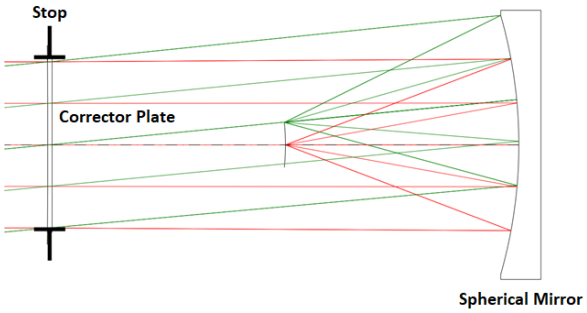

Figure 4.10: Aspheric corrector at the system's stop [11].

plate only introduces third-order spherical aberration that counteracts the spherical aberration from the spherical mirror [9]. The overall third order spherical aberration induced by the plate is given by (see Equation 4.16):

$$W_{Corrector,\ Stop} = W_{040}(\vec{\rho} \cdot \vec{\rho})^2 \tag{4.29}$$

If the aspheric corrector plate is longitudinally shifted along the optical axis with reference to the physical aperture stop, as shown in Figure 4.11, the beam for an off-axis field point will move across the plate. As a result, each field point receives a different contribution from the surface. This displacement of the beam leads to a complete surface aberration contribution that incorporates all the third-order aberrations dependent on the field, alongside third-order spherical aberration.

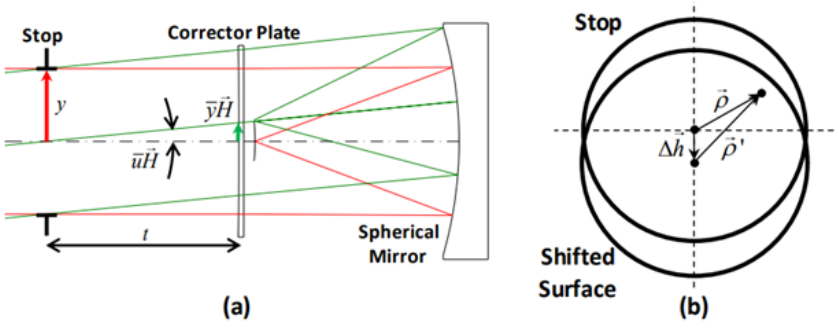

Figure 4.11: a) Displacement of the aspheric corrector plate and consequent displacement of the off-axis beam. b) Beam displacement on the corrector plate as a field dependent decenter of the corrector plate at the stop [9].

To describe the field dependent aberration generation, the amount of relative beam displacement, $\Delta\vec{h}$, is defined:

$$\Delta\vec{h} = \left(\frac{\bar{y}}{y}\right)\vec{H} = \left(\frac{\bar{u}t}{y}\right)\vec{H}, \tag{4.30}$$

where $\bar{y}$ is the paraxial chief ray height on the aspheric plate, y is the paraxial marginal ray height on the aspheric plate, $\bar{u}$ is the paraxial chief ray angle, t is the distance between the aspheric corrector plate and the aperture stop, and $\vec{H}$ is the normalized, two-dimensional field vector that identifies the field point of interest in the image plane, as previously described. Conceptually, the displacement of the beam on the aspheric corrector plate when it is moved away from the stop can be viewed of as a field-dependent offset of the corrector plate when it is located at the stop, as depicted in Figure 4.11. The net aberration contribution of the aspheric corrector plate, $W(\vec{\rho})$, that only depends on the normalized pupil vector $\vec{\rho}$ since the surface is located at the stop, has to be remapped to a modified pupil vector, $\vec{\rho'}$. By replacing $\vec{\rho}$ with $\vec{\rho'}+\Delta\vec{h}$ and expanding the pupil dependence, the modified aberration contribution can be written as:

$$\begin{aligned} W_{\textit{Corrector, Not}-\textit{Stop}} &= W_{040}\left[(\vec{\rho'}+\Delta\vec{h})\cdot(\vec{\rho'}+\Delta\vec{h})\right]^2 = \\ = W_{040}\Big[&(\vec{\rho}\cdot\vec{\rho})^2 + 4(\Delta\vec{h}\cdot\vec{\rho})(\vec{\rho}\cdot\vec{\rho}) + 4(\Delta\vec{h}\cdot\Delta\vec{h})(\vec{\rho}\cdot\vec{\rho}) + \\ &+2(\Delta\vec{h^2}\cdot\vec{\rho^2}) + 4(\Delta\vec{h}\cdot\Delta\vec{h})(\Delta\vec{h}\cdot\vec{\rho}) + (\Delta\vec{h}\cdot\Delta\vec{h})^2\Big], \end{aligned} \tag{4.31}$$

where the primes have been dropped. Since $\Delta\vec{h} \propto \vec{H}$ the modified aberration contribution becomes field dependent when the plate is shifted away from the stop. Therefore, it can be seen that the original spherical aberration contribution from the aspheric plate generates also lower order field dependent aberration components as the plate is moved. The aberration terms that are generated by this expansion are, in the order they appear, the conventional third order spherical aberration, coma, field curvature, astigmatism, distortion and piston. The generation of these field dependent aberration terms is not restricted to rotationally symmetric corrector plates and can be applied to Zernike freeform polynomial surfaces.

4.4 The aberration fields of a Zernike Polynomial surface overlay

To introduce the approach discussed in Section 4.3.1 to Zernike polynomial surfaces, they firstly must be related to the field constant aberration they induce at the stop surface; then, the modified pupil vector $\vec{\rho}'$ has to be introduced, in the same way it has been done in Equation 4.31, to establish what field dependent aberration components are induced when the polynomial surface is displaced longitudinally from the stop surface [9].
For the aspheric corrector plate of the Schmidt telescope, the resulting field constant aberration is third order spherical aberration. Similarly, a plate at the stop, deformed by one of the Zernike terms related to an aberration, will also introduce a field constant aberration. By incorporating the vector pupil dependence of the Zernike overlay terms, the induced field constant aberration, predicted by NAT, can be added to the total aberration field. From this initial field constant aberration, the field dependent nature can then be developed for the case when the plate is positioned away from the stop, as explained in [9].

4.4.1 Astigmatism

In order of increasing radial dependence, the first freeform overlay term to consider is astigmatism, which is given by:

$$\begin{pmatrix} z_5 & z_6 \end{pmatrix} \begin{pmatrix} Z_5 \\ Z_6 \end{pmatrix} = \begin{pmatrix} z_5 & z_6 \end{pmatrix} \begin{pmatrix} \rho^2 \cos 2\phi \\ \rho^2 \sin 2\phi \end{pmatrix} \tag{4.32}$$

where z_5 and z_6 are the coefficient values for the astigmatism term, ρ is the normalized radial coordinate and ϕ is the azimuthal angle on the surface, measured counter-clockwise from the x-axis of a right-handed coordinate system. The magnitude of the overlay is calculated from the coefficients as:

$$\left|z_{5/6}\right|_{FF} = \sqrt{z_5^2 + z_5^2}, \tag{4.33}$$

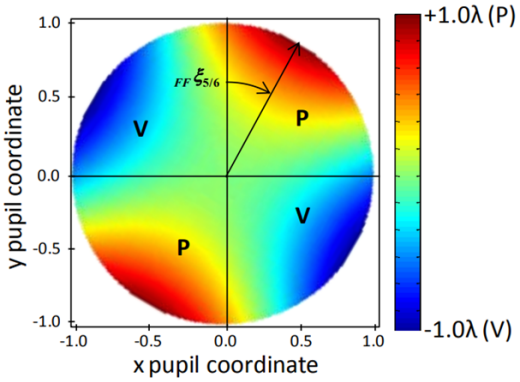

Figure 4.12: Surface map of the astigmatism term. The error in quantified by its magnitude and orientation. P and V denote where the surface error is a peak or a valley [9].

while the orientation of the overlay is defined as:

$$\xi_{5/6_{FF}} = \frac{\pi}{2} - \frac{1}{2}\arctan\left(\frac{z_6}{z_5}\right) \tag{4.34}$$

to be consistent with the conventions of NAT. Figure 4.12 shows a surface map describing the freeform Zernike overlay for astigmatism, over the full aperture, with its magnitude and orientation.

Zernike astigmatism is introduced into the vector multiplication environment of NAT with observing that:

$$if\,\vec{\rho} = \rho\begin{pmatrix}\sin\phi\\ \\ \cos\phi\end{pmatrix}, then\ \vec{\rho^2} = \rho^2\begin{pmatrix}\sin\phi\\ \\ \cos\phi.\end{pmatrix} \tag{4.35}$$

From the pupil dependence in Equation 4.35, it is deduced that the astigmatism overlay will induce field constant astigmatism, predicted by NAT (see Equation 4.23), when placed at the stop or pupil. Based on this observation, it can be added to the total aberration field as (see Equation 4.16):

$$W_{Stop} = \frac{1}{2}(\vec{B^2}_{222_{FF}} \cdot \vec{\rho^2}), \tag{4.36}$$

where $\vec{B^2}_{222_{FF}}$ is a two-dimensional vector that describes the magnitude and orientation of

the astigmatic overlay related to the overall Zernike astigmatism by:

$$\vec{B^2}_{222_{FF}} = -2\left|z_{5/6}\right|e^{i2\xi_{5/6_{FF}}}. \tag{4.37}$$

If a surface with a Zernike astigmatism overlay is now placed away from the stop, the beam footprint for an off-axis field angle will begin to displace across the surface resulting in the creation of a number of field dependent terms. Replacing $\vec{\rho}$ with $\vec{\rho'} + \Delta\vec{h}$, expanding the pupil dependence and dropping the primes, it can be written:

$$\begin{aligned} W_{Not-Stop} &= \frac{1}{2}\left[\vec{B^2}_{222_{FF}} \cdot (\vec{\rho} + \Delta\vec{h})^2\right] = \\ &= \frac{1}{2}\left[\vec{B^2}_{222_{FF}} \cdot \vec{\rho^2} + 2\vec{B^2}_{222_{FF}} \cdot \Delta\vec{h}\vec{\rho} + \vec{B^2}_{222_{FF}} \cdot \Delta\vec{h^2}\right]. \end{aligned} \tag{4.38}$$

To map the impact of these additive terms on the overall field dependent wave aberration expansion of an optical system, the pupil dependence needs to be converted into existing aberration types. To this end, an additional vector operation is introduced:

$$\vec{A} \cdot \vec{B}\vec{C} = \vec{A}\vec{B^*} \cdot \vec{C}, \tag{4.39}$$

where $\vec{B^*}$ is a conjugate vector with the same properties of a conjugate complex variable. By applying the vector operation in Equation 4.39, Equation 4.38 takes the form:

$$W_{Not-Stop} = \frac{1}{2}\left[\vec{B^2}_{222_{FF}} \cdot \vec{\rho^2} + 2\vec{B^2}_{222_{FF}}\Delta\vec{h^*} \cdot \vec{\rho} + \vec{B^2}_{222_{FF}} \cdot \Delta\vec{h^2}\right]. \tag{4.40}$$

Two additional field dependent terms are generated, in addition to the anticipated field constant astigmatism term (first term in the Equation 4.40). However, the second and third term are tilt and piston, which do not affect the image quality. So, these terms will not be addressed, as they are not exactly degrading aberrations. In this case, the only image degrading aberration is field constant astigmatism that is independent of where the Zernike astigmatism overlay is located with respect to the stop. The FFD for field constant astigmatism is displayed in Figure 4.13:

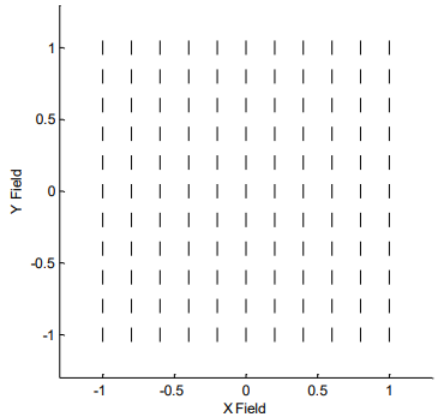

Figure 4.13: FFD of field constant astigmatism generated by a Zernike astigmatism overlay away from the stop [9].

In order to incorporate the new freeform contribution into NAT, the field constant astigmatic term $\vec{B^2}_{222}$ can be rewritten as a sum of the misalignment-induced contribution and a freeform contribution:

$$\vec{B^2}_{222} = \vec{B^2}_{222_{Align.}} + \sum_{j=1}^{N} \vec{B^2}_{222_{FF}}. \tag{4.41}$$

4.4.2 Coma

The next freeform overlay term in order of pupil dependence is Zernike coma. As a property of the Zernike polynomial set, a tilt term is inherently built into Zernike coma to minimize the RMS wavefront error of the aberration over the aperture. As a consequence, to introduce coma in the vectorial environment of NAT, a modified Zernike coma that combines both Zernike coma and tilt is used:

$$\begin{pmatrix} z_7 & z_8 \end{pmatrix} \begin{pmatrix} Z_7^{Adj.} \\ Z_8^{Adj.} \end{pmatrix} = \begin{pmatrix} z_7 & z_8 \end{pmatrix} \begin{pmatrix} Z_7 + 2Z_2 \\ Z_8 + 2Z_3 \end{pmatrix} = \begin{pmatrix} z_7 & z_8 \end{pmatrix} \begin{pmatrix} 3\rho^3 \cos\phi \\ 3\rho^3 \sin\phi \end{pmatrix}. \tag{4.42}$$

The magnitude $\left|z_{7/8_{FF}}\right|$ and orientation $\xi_{7/8_{FF}}$ of the freeform, Zernike coma overlay can

be computed from the coefficients, similarly to Zernike astigmatism. The overlay term in Equation 4.42 is linked to the vectorial environment of NAT observing that:

$$if\ \vec{\rho} = \rho \begin{pmatrix} \sin\phi \\ \\ \cos\phi \end{pmatrix},\ then\ \ (\vec{\rho}\cdot\vec{\rho})\vec{\rho} = \rho^3 \begin{pmatrix} \sin\phi \\ \\ \cos\phi \end{pmatrix}. \tag{4.43}$$

From the vector pupil dependence in Equation 4.43, it is deduced that the overlay will induce field constant coma when located at the stop surface, and is added to the total aberration as (see Equation 4.16):

$$W_{Stop} = (\vec{A}_{131_{FF}}\cdot\vec{\rho})(\vec{\rho}\cdot\vec{\rho}), \tag{4.44}$$

where $\vec{A}_{131_{FF}}$ has the same meaning as the corresponding vector for astigmatism and can be written as:

$$\vec{A}_{131_{FF}} = -3\left|z_{7/8}\right|e^{i2\xi_{7/8_{FF}}}. \tag{4.45}$$

Again replacing $\vec{\rho}$ with $\vec{\rho'} + \Delta\vec{h}$ in Equation 4.44, expanding the pupil dependence and converting it into existing aberration types, the wavefront expansion becomes:

$$\begin{aligned} W_{Not-Stop} = \Big[&(\vec{A}_{131_{FF}}\cdot\vec{\rho})(\vec{\rho}\cdot\vec{\rho}) + \vec{A}_{131_{FF}}\Delta\vec{h}\cdot\vec{\rho^2} + 2(\vec{A}_{131_{FF}}\cdot\Delta\vec{h})(\vec{\rho}\cdot\vec{\rho}) + \\ &+2(\Delta\vec{h}\cdot\Delta\vec{h})(\vec{A}_{131_{FF}}\cdot\vec{\rho}) + \vec{A^*}_{131}\Delta\vec{h^2}\cdot\vec{\rho} + (\vec{A}_{131_{FF}}\cdot\Delta\vec{h})(\Delta\vec{h}\cdot\Delta\vec{h})\Big] \end{aligned} \tag{4.46}$$

The first term is the predicted field constant coma. The second term is a form of field asymmetric, field linear astigmatism based on the $\vec{\rho^2}$ aperture dependence. The third term is a field linear, medial field curvature based on the $\vec{\rho}\cdot\vec{\rho}$ aperture dependence. All these terms can be integrated in NAT and associated to the relative misalignment-generated contribution, as it was previously seen for astigmatism. Figure 4.14 displays the FFD of the different contributions generated by the Zernike coma overlay away from the stop.

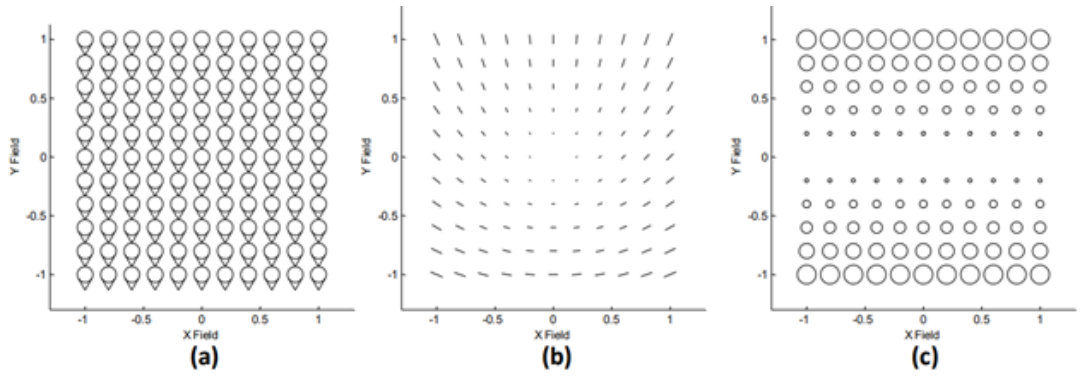

Figure 4.14: FFD of a) field constant coma, b) field asymmetric,field linear astigmatism and c) field linear medial field curvature, generated by a Zernike coma overlay away from the stop [9].

4.4.3 Trefoil

The Zernike trefoil (or elliptical coma) overlay has the same pupil dependence as coma, but a higher order of azimuthal dependence:

$$\begin{pmatrix} z_{10} & z_{11} \end{pmatrix} \begin{pmatrix} Z_{10} \\ \\ Z_{11} \end{pmatrix} = \begin{pmatrix} z_{10} & z_{11} \end{pmatrix} \begin{pmatrix} \rho^3 \cos 3\phi \\ \\ \rho^3 \sin 3\phi \end{pmatrix}. \tag{4.47}$$

The magnitude $\left|z_{10/11_{FF}}\right|$ of the Zernike trefoil overlay is calculated as usual, while the orientation is differently computed:

$$\xi_{10/11_{FF}} = \frac{\pi}{2} - \frac{1}{3} \arctan\left(\frac{z_{11}}{z_{10}}\right). \tag{4.48}$$

The overlay term is linked to the vectorial environment of NAT with the following observation:

$$if\, \vec{\rho} = \rho \begin{pmatrix} \sin\phi \\ \\ \cos\phi \end{pmatrix},\ then\ \vec{\rho^3} = \rho^3 \begin{pmatrix} \sin 3\phi \\ \\ \cos 3\phi. \end{pmatrix} \tag{4.49}$$

As usual, from the vector pupil dependence it is deduced that the trefoil overlay will induce field constant trefoil, when located at the stop surface, and can be added to the total aberra-

tion field as (see Equation 4.16):

$$W_{Stop} = \frac{1}{4}(\vec{C}^{3}{}_{333_{FF}} \cdot \vec{\rho}^{3}), \tag{4.50}$$

where $\vec{C}^{3}{}_{333_{FF}}$ is defined as:

$$\vec{C}_{333_{FF}} = -4\left|z_{10/11}\right| e^{i3\xi_{10/11_{FF}}}. \tag{4.51}$$

Replacing $\vec{\rho}$ with $\vec{\rho}' + \Delta\vec{h}$ in Equation 4.50, expanding the pupil dependence and converting it into existing aberration types, the wavefront expansion becomes:

$$\begin{aligned} W_{Not-Stop} = \frac{1}{4}\Big[& \vec{C}^{3}{}_{333_{FF}} \cdot \vec{\rho}^{3} + 3\vec{C}^{3}{}_{333_{FF}}\Delta\vec{h}^{*} \cdot \vec{\rho}^{2} + \\ & + 3\vec{C}^{3}{}_{333_{FF}}\Delta\vec{h}^{*^2} \cdot \vec{\rho} + \vec{C}^{3}{}_{333_{FF}} \cdot \Delta\vec{h}^{3}\Big]. \end{aligned} \tag{4.52}$$

Other then the expected field constant trefoil, the additional, image degrading term generated by the trefoil overlay away from the stop is a field conjugate, field linear astigmatism, as can be seen from the second term of Equation 4.52, where the conjugate vector $\vec{h}^{*}$ appears. Figure 4.15 shows the FFD of the different contributions generated by the Zernike trefoil overlay placed away from the stop.

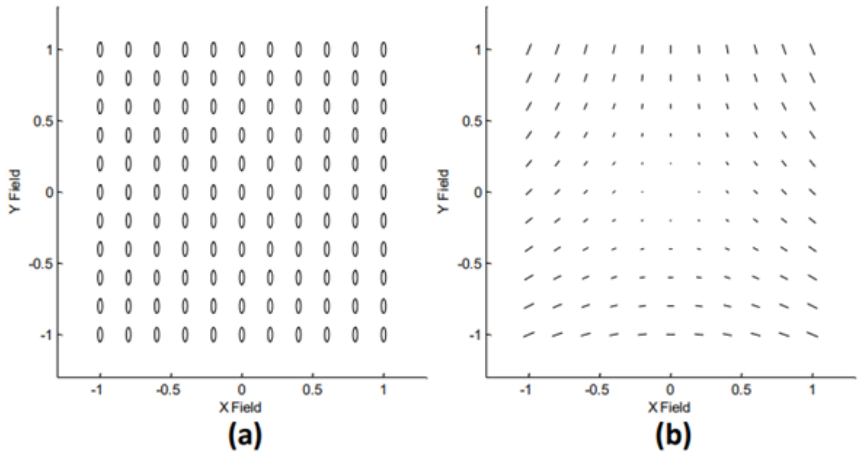

Figure 4.15: FFD of a) field constant trefoil and b) field linear, field conjugate astigmatism [9].

4.4.4 Oblique spherical aberration

Moving to the next pupil order, the next freeform overlay term is Zernike oblique spherical aberration, written as:

$$\begin{pmatrix} z_{12} & z_{13} \end{pmatrix} \begin{pmatrix} Z_{12} \\ \\ Z_{13} \end{pmatrix} = \begin{pmatrix} z_{12} & z_{13} \end{pmatrix} \begin{pmatrix} 4\rho^4 \cos 2\phi - 3\rho^2 \cos 2\phi \\ \\ 4\rho^4 \sin 2\phi - 3\rho^2 \sin 2\phi \end{pmatrix}. \tag{4.53}$$

Similarly to the case of Zernike coma, there is an included astigmatic term to minimize the RMS wavefront error of the oblique spherical aberration term. In order to introduce the overlay in the vectorial environment of NAT, an adjusted Zernike oblique spherical aberration is defined, combining both Zernike oblique spherical aberration and Zernike astigmatism:

$$\begin{aligned} \begin{pmatrix} z_{12} & z_{13} \end{pmatrix} \begin{pmatrix} Z_{12}^{Adj.} \\ \\ Z_{13}^{Adj.} \end{pmatrix} = \begin{pmatrix} z_{12} & z_{13} \end{pmatrix} \begin{pmatrix} Z_{12} + 3Z_5 \\ \\ Z_{13} + 3Z_6 \end{pmatrix} = \\ = \begin{pmatrix} z_{12} & z_{13} \end{pmatrix} \begin{pmatrix} 4\rho^4 \cos 2\phi \\ \\ 4\rho^4 \sin 2\phi \end{pmatrix}. \end{aligned} \tag{4.54}$$

The magnitude $\left|z_{12/13_{FF}}\right|$ and orientation $\xi_{12/13_{FF}}$ of the freeform, Zernike oblique spherical overlay can be computed from the coefficients, in the same way it has been done for Zernike astigmatism and coma. The overlay term in Equation 4.54 is introduced into the NAT environment knowing that:

$$if\ \vec{\rho} = \rho \begin{pmatrix} \sin\phi \\ \\ \cos\phi \end{pmatrix},\ then\ \ (\vec{\rho} \cdot \vec{\rho^2})\vec{\rho} = \rho^4 \begin{pmatrix} \sin 2\phi \\ \\ \cos 2\phi \end{pmatrix}. \tag{4.55}$$

Again, from the vector pupil dependence it is deduced that the oblique spherical overlay will induce field constant, oblique spherical aberration, that can be added to the total aberration field as (see Equation 4.16):

$$W_{Stop} = (\vec{B^2}_{242_{FF}} \cdot \vec{\rho^2})(\vec{\rho} \cdot \vec{\rho}), \tag{4.56}$$

where the vector $\vec{B^2}_{242_{FF}}$ relates to adjusted Zernike oblique spherical aberration by:

$$\vec{B^2}_{242_{FF}} = -8\left|z_{12/13}\right|e^{i2\xi_{12/13_{FF}}}. \tag{4.57}$$

Replacing $\vec{\rho}$ with $\vec{\rho'} + \Delta\vec{h}$ in Equation 4.56, expanding the pupil dependence and converting it into existing aberration types, the wavefront expansion becomes:

$$\begin{aligned} W_{Not-Stop} = \frac{1}{2}\Bigg[&(\vec{B^2}_{242_{FF}} \cdot \vec{\rho}^2)(\vec{\rho} \cdot \vec{\rho}) + 3(\vec{B^2}_{242_{FF}}\Delta\vec{h^*} \cdot \vec{\rho})(\vec{\rho} \cdot \vec{\rho}) + \vec{B^2}_{242_{FF}}\Delta\vec{h} \cdot \vec{\rho}^3 + \\ &+3(\Delta\vec{h} \cdot \Delta\vec{h})(\vec{B^2}_{242_{FF}} \cdot \vec{\rho}^2) + 3(\vec{B^2}_{242_{FF}} \cdot \Delta\vec{h^2})(\vec{\rho} \cdot \vec{\rho}) + \\ &+2(\vec{B^2}_{242_{FF}} \cdot \Delta\vec{h^2})(\Delta\vec{h} \cdot \vec{\rho}) + 2(\Delta\vec{h} \cdot \Delta\vec{h})(\vec{B^2}_{242_{FF}}\Delta\vec{h^*} \cdot \vec{\rho}) + \\ &+(\Delta\vec{h} \cdot \Delta\vec{h})(\vec{B^2}_{242_{FF}} \cdot \Delta\vec{h^2})\Bigg]. \end{aligned} \tag{4.58}$$

The first image degrading term is the anticipated field constant oblique spherical aberration; the second term is field linear, field conjugate coma based on the $(\vec{\rho} \cdot \vec{\rho})\vec{\rho}$ dependence; the third term is identified as field linear trefoil based on the $\vec{\rho^3}$ dependence; the fourth term is a fifth order, field quadratic astigmatism, dependent on $\vec{\rho^2}$, and the final term is a fifth order medial field curvature aberration based on the $(\vec{\rho} \cdot \vec{\rho})$ dependence. Figure 4.16 shows the FFD of the different contributions generated by the Zernike oblique spherical aberration overlay placed away from the stop.

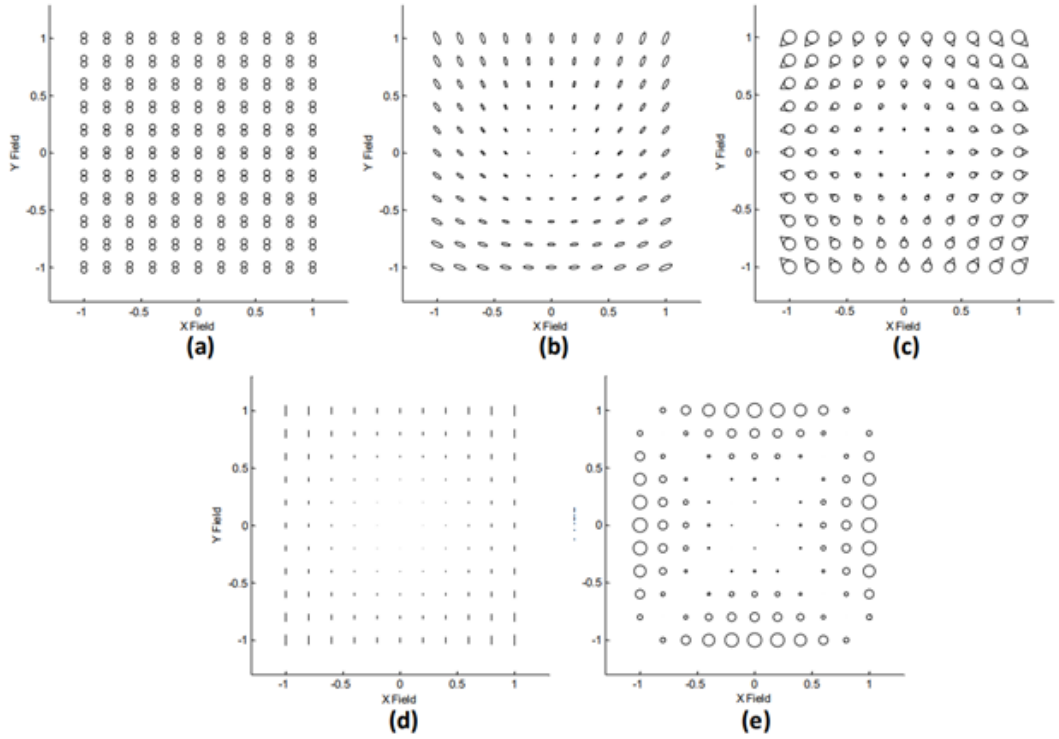

Figure 4.16: FFD of a) field constant oblique spherical aberration, b) field asymmetric, field linear trefoil, c) field conjugate, field linear coma, d) field quadratic astigmatism and e) field quadratic, medial field curvature, generated by a Zernike oblique spherical aberration overlay away from the stop [9].

4.4.5 Fifth order aperture coma

The last freeform overlay term is Zernike fifth order aperture coma, that can be written as:

$$\begin{pmatrix} z_{14} & z_{15} \end{pmatrix} \begin{pmatrix} Z_{14} \\ \\ Z_{15} \end{pmatrix} = \begin{pmatrix} z_{14} & z_{15} \end{pmatrix} \begin{pmatrix} 10\rho^5 \cos\phi - 12\rho^3 \cos\phi + 3\rho\cos\phi \\ \\ 10\rho^5 \sin\phi - 12\rho^3 \sin\phi + 3\rho\sin\phi \end{pmatrix}. \tag{4.59}$$

Within this term there are a fifth-power and a cubic aperture coma term $(\rho^5), (\rho^3)$ and a linear aperture tilt term to minimize the RMS wavefront error. In order to introduce the fifth aperture coma term into the NAT vectorial environment, an adjusted Zernike fifth order

aperture coma is defined, combining Zernike fifth aperture coma, coma and tilt:

$$\begin{pmatrix} z_{14} & z_{15} \end{pmatrix} \begin{pmatrix} Z_{14}^{Adj.} \\ Z_{15}^{Adj.} \end{pmatrix} = \begin{pmatrix} z_{14} & z_{15} \end{pmatrix} \begin{pmatrix} Z_{14} + 4Z_7 + 5Z_2 \\ Z_{15} + 4Z_8 + 5Z_3 \end{pmatrix} = \\ = \begin{pmatrix} z_{14} & z_{15} \end{pmatrix} \begin{pmatrix} 10\rho^5 \cos\phi \\ 10\rho^5 \sin\phi \end{pmatrix}. \tag{4.60}$$

The magnitude $\left|z_{14/15_{FF}}\right|$ of the freeform overlay is computed from the coefficients as previously done, the orientation $\xi_{14/15_{FF}}$ is given by:

$$\xi_{14/15_{FF}} = \frac{\pi}{2} - \arctan\frac{z_{15}}{z_{14}}. \tag{4.61}$$

To introduce the overlay, it has to be observed that:

$$if\ \vec{\rho} = \rho \begin{pmatrix} \sin\phi \\ \cos\phi \end{pmatrix},\ then\ \ (\vec{\rho}\cdot\vec{\rho})^2\vec{\rho} = \rho^5 \begin{pmatrix} \sin\phi \\ \cos\phi \end{pmatrix}. \tag{4.62}$$

When located at the stop, the overlay will induce constant fifth order aperture coma when placed at the stop, that can be added to the total aberration field as:

$$W_{Stop} = (\vec{A}_{151_{FF}} \cdot \vec{\rho})(\vec{\rho}\cdot\vec{\rho})^2, \tag{4.63}$$

where $\vec{A}_{151_{FF}}$ is given by:

$$\vec{A}_{151_{FF}} = -10\left|z_{14/15}\right| e^{i\xi_{14/15_{FF}}}. \tag{4.64}$$

Replacing $\vec{\rho}$ with $\vec{\rho'} + \Delta\vec{h}$ in Equation 4.63, expanding the pupil dependence and converting it into existing aberration types, the wavefront expansion becomes:

$$\begin{aligned} W_{Not-Stop} = (\vec{A}_{151_{FF}} \cdot \vec{\rho})(\vec{\rho} \cdot \vec{\rho})^2 + 3(\vec{A}_{151_{FF}} \cdot \Delta\vec{h})(\vec{\rho} \cdot \vec{\rho})^2 + (\vec{A}_{151_{FF}}\Delta\vec{h}^2 \cdot \vec{\rho}^3) + \\ + \left[6(\vec{A}_{151_{FF}} \cdot \Delta\vec{h})\Delta\vec{h} + 3(\Delta\vec{h} \cdot \Delta\vec{h})\vec{A}_{151_{FF}}\right] \cdot \vec{\rho}(\vec{\rho} \cdot \vec{\rho}) + \\ + \left[2(\vec{A}_{151_{FF}} \cdot \Delta\vec{h}) \cdot \Delta\vec{h}^2 + 2(\Delta\vec{h} \cdot \Delta\vec{h})\vec{A}_{151_{FF}} \cdot \Delta\vec{h}\right] \cdot \vec{\rho}^2 + \\ + 2(\vec{A}_{151_{FF}}\Delta\vec{h} \cdot \vec{\rho}^2)(\vec{\rho} \cdot \vec{\rho}) + 6(\Delta\vec{h} \cdot \Delta\vec{h})(\vec{A}_{151_{FF}} \cdot \Delta\vec{h})(\vec{\rho} \cdot \vec{\rho}) + \\ + \left[(\Delta\vec{h} \cdot \Delta\vec{h})^2\vec{A}_{151_{FF}} + 4(\vec{A}_{151_{FF}} \cdot \Delta\vec{h})(\Delta\vec{h} \cdot \Delta\vec{h})\Delta\vec{h}\right] \cdot \vec{\rho} + \\ + (\Delta\vec{h} \cdot \Delta\vec{h})^2(\vec{A}_{151_{FF}} \cdot \Delta\vec{h}) \end{aligned} \tag{4.65}$$

The first term is field constant, fifth order aperture coma; then, proceeding in order of decreasing pupil dependence, the second term is identified as medial oblique spherical aberration. The sixth term is identified as oblique spherical aberration based on the $(\vec{\rho} \cdot \vec{\rho})\vec{\rho^2}$ dependence, where the aberration is linear throughout the field; The third term is a field quadratic trefoil aberration with a $\vec{\rho}^3$ dependence. The fourth and fifth terms are both identified as a form of fifth order, field cubic coma. Likewise, the sixth and seventh terms are a form of fifth order astigmatism based on the $\vec{\rho^2}$ dependence. Lastly, the ninth term is a fifth order medial field curvature term. Figure 4.17 shows the FFD of the different contributions generated by the Zernike, fifth order aperture, coma overlay, placed away from the stop.

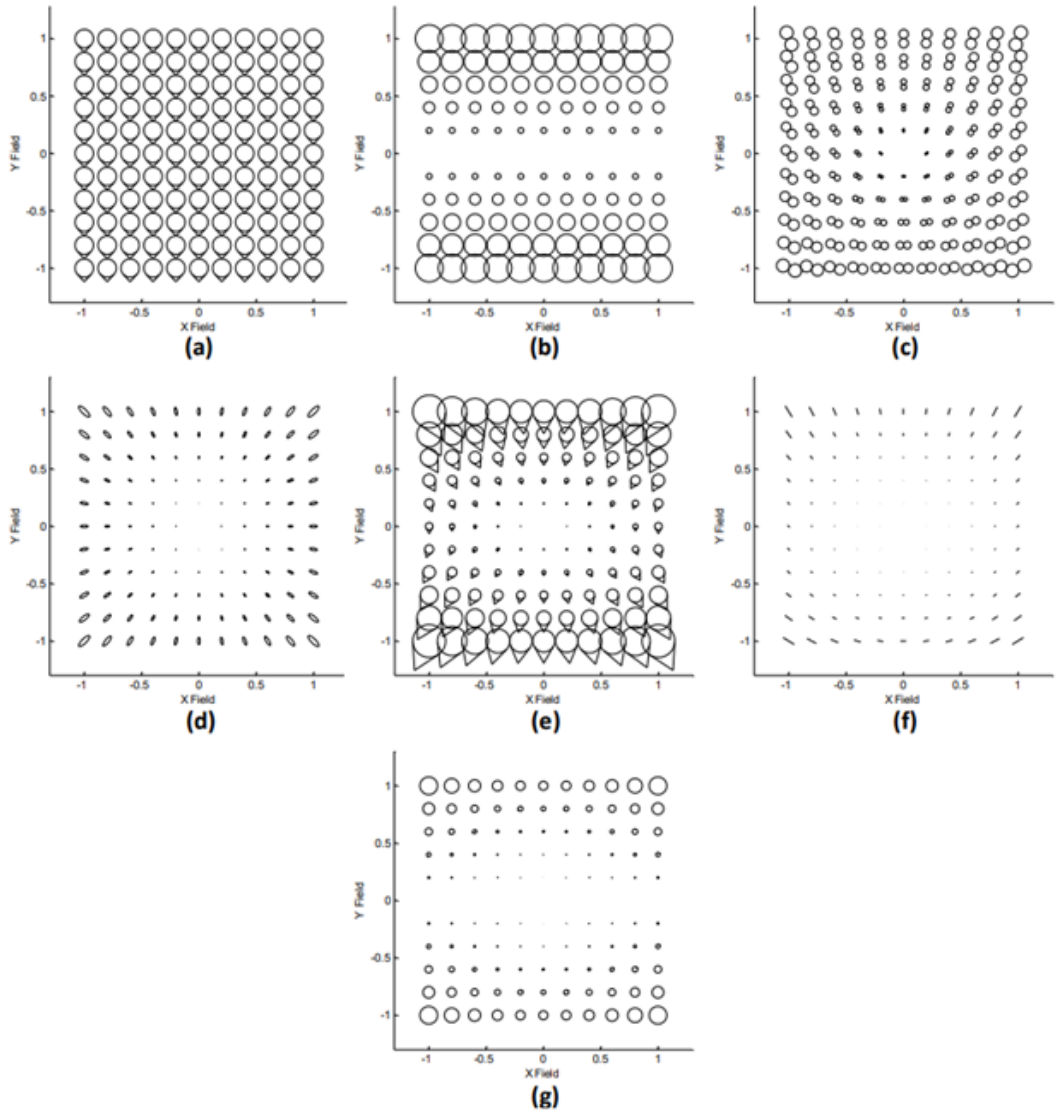

Figure 4.17: FFD of a) field constant, fifth order aperture coma, b) field linear, medial oblique spherical aberration, c) field asymmetric, field linear, oblique spherical aberration, d) field quadratic trefoil, e) field quadratic coma, f) field asymmetric, field cubed astigmatism , and g) field cubic, field curvature, generated by a Zernike fifth order aperture coma overlay away from the stop [9].

5

Freeform Surfaces Integration: results

The analisys of the NAT predicted aberrations will constitute the backbone of the design of the VICESS-like camera and HYPSOS-like imaging spectrograph. In fact, using the Full Field Display tool of the optical design software, it is possible to visualize what are the field aberrations generated by the optical system, and to understand which Zernike terms add to a surface, either at or beyond the aperture stop, to correct an aberration with a specific field dependence [39]. Both the instruments, described as starting configurations in Chapter 3, will be firstly adjusted in their layout to meet new requirements or to further simplify the design; then, the Zernike freeform overlays will be added to the conic mirrors of the TMA telescopes to address the residual aberrations.

5.1 VICESS-like instrument

5.1.1 Preliminary design adjustments

Before introducing the freeform surfaces into the VICESS design, few adjustments were made to create a design that could better accommodate these surfaces. Firstly, the aper-

ture stop has been placed on the secondary mirror to slightly reduce the size of the mirrors. Whereas in the original design it was an aperture placed before the primary mirror that limited the amount of light entering the system, in this case it is the size of the secondary mirror that manages the telescope throughput. This created the conditions for the possible insertion of a freeform surface at the stop to introduce a constant aberration correction with respect to the field, as discussed in Chapter 5. Then, both the focal length and the entrance pupil[1] diameter were increased in order to achieve a greater photonic throughput and thus extend the observing capabilities also to darker environments, such as the Outer Solar System. The focal length has been increased from f = 250 mm to f= 375 mm, while the entrance pupil diameter has been increased from d= 40 mm to d = 60 mm; the $f/\#$ therefore remained the same and equal to 6.5. Finally, an attempt was made to reduce the overall size of the system, the result being a more compact design of approximately 20% in the horizontal direction. The field of view and the working spectral range have remained the same.

The final design, optimized in the ray-tracing software Zemax-OpticStudio, is shown in Figure 5.1. The object is a point source positioned at infinity. The light beam enters the system through a 90 mm diameter aperture, proceeding towards the primary mirror M1, placed at 190 mm from the aperture. The beam then impinges on the secondary mirror M2 and the tertiary, M3, and is then splitted by the dichroic according to the wavelengths. Each channel proceeds independently, and the splitted beams are focused in two different focal planes.

Tables 5.1 and 5.2 summarize the optical parameters of the system, for both the VIS/near-IR and IR configurations. The values given in the Tables result from the optimisation of the system via ray tracing software; they will need to be redefined during the construction phase, in accordance with optical realisation tolerances and system alignment, according to the demanded performance requirements.

[1]The entrance pupil is defined as the image of the aperture stop made by all the optical surfaces preceding the stop itself.

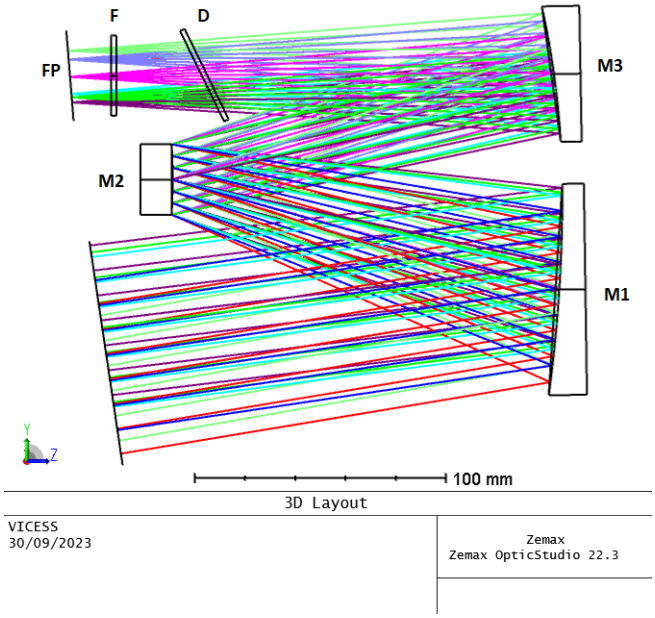

(a) Final layout for the VIS/near-IR configuration.

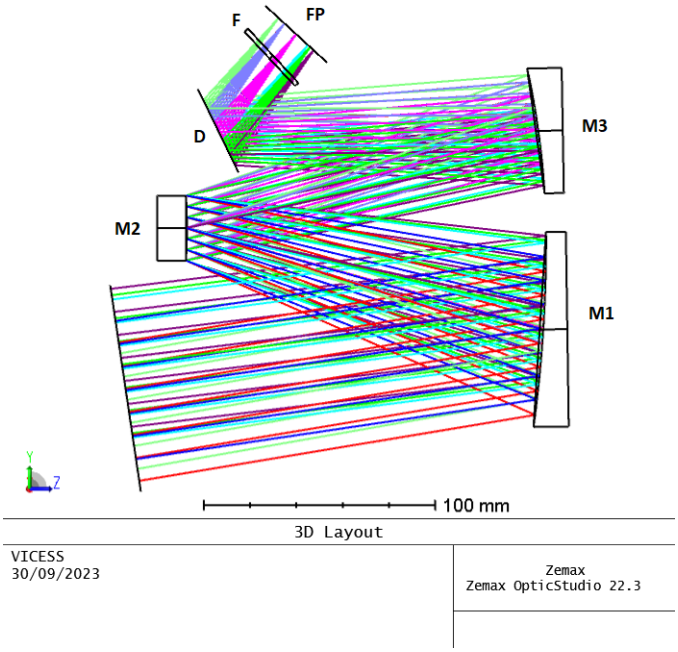

(b) Final layout for the IR configuration.

Figure 5.1: Final layout for a VICESS-like instrument. For both configurations, light is collected by the primary (M1), secondary (M2) and tertiary (M3) mirrors. The beam is split by the dichroic (D) according to the operating spectral range, and each of the two resulting beams passes through a suitable filter (F) and is focused on the focal plane (FP).

Surface	mirror-M1	mirror-M2	mirror-M3
Type	Standard	Standard	Standard
Radius (mm)	−581.2500	−250.1073	−346.0660
Distance to next surface (mm)	−155.0000	155.0000	−120.0000
Parent surface diameter (mm)	86.1866	28.0000	66.2188
Aperture diameter (mm)	84.0000	28.0000	54.0000
Decenter y (mm)	−46.0000	0.0000	42.0000
Conic	−1.8485	−2.1056	−0.5331
Tilt about x (°)	7.6000	0.8423	−1.0000
Coating	Metal	Metal	Metal

Table 5.1: Optical parameters for the three mirrors M1, M2, M3.

Surface	Dichroic	Filter Wheel	Focal Plane
Type	Standard	Standard	Standard
Radius (mm)	Infinity	Infinity	Infinity
Distance to next surface (mm)	−38.2743	−15.0000	-
	39.9711	15.0000	-
Thickness (mm)	2.0000	2.0000	2.0000
Aperture x-half width (mm)	14.5000	14.000	16.0000
	14.5000	14.000	16.0000
Aperture x-half width (mm)	20.0000	14.000	16.0000
	20.0000	14.000	16.0000
Tilt about x (°)	−25.0000	26.000	−5.0484
	−25.0000	−17.0000	−1.7811

Table 5.2: Optical parameters for dichroic, filter Wheels and focal planes. Note that when two values for the same parameter are reported, they respectively refer to the VIS/near-IR configuration (first) and to the IR configuration (second). The dichroic's shape has been assumed to be rectangular, even though in reality it will probably be elliptical. Instead, the single filters in the Filter Wheels, as well as the focal planes, are squared.

Figures 5.2 and 5.3 show instead the performance of the modified design in terms of Spot Diagram, for both channels. The Airy radius reported for both configurations is referred to the shortest operative wavelength within the configuration.
It is evident that in both configurations, the system's performance is not optimal, since it is diffraction-limited only for certain fields and wavelengths. The aberrations in this system are far greater than in the original system due to the larger aperture and longer focal length. The scale bar is set at 30 μm for the VIS/near-IR configuration and at 100 μm for the IR configuration to make the Spot Diagrams clearer. However, the dedicated sensors' pixel size would likely be much smaller, around 10 μm for the VIS/near-IR configuration, and 18-20 μm for the IR configuration.

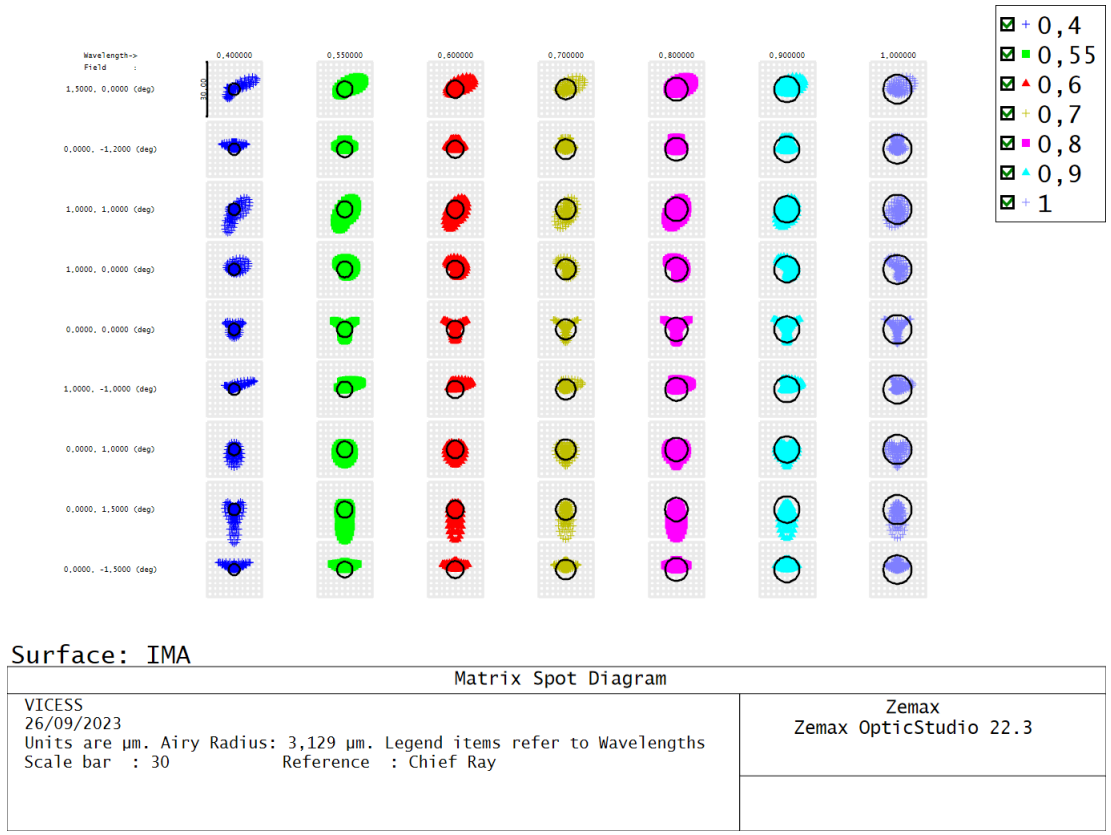

Figure 5.2: Matrix Spot Diagram for the VIS/near-IR configuration. The scale bar is set at 30 μm.

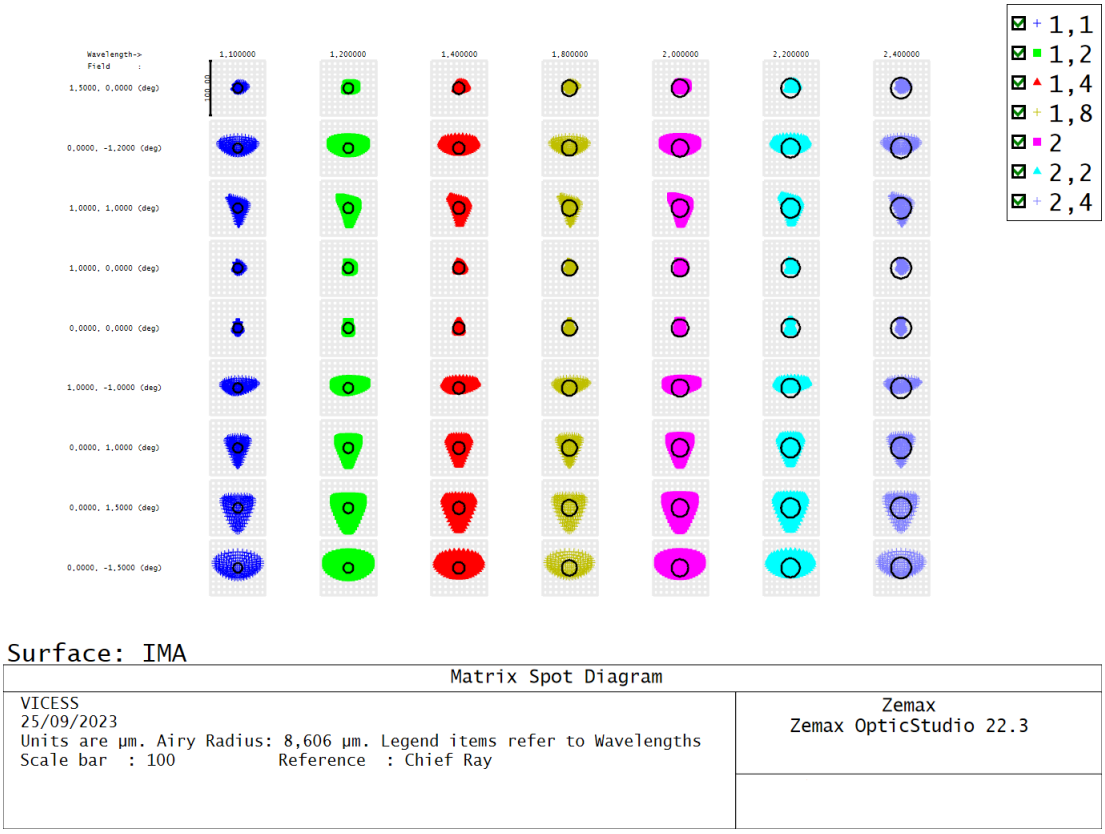

Figure 5.3: Matrix Spot Diagram for the IR configuration. The scale bar is set at 100 μm.

Spot Diagrams can be complemented by Enclosed Energy Diagrams, which are indicative of the percentage of total energy enclosed as a function of distance, from either the chief ray or the image centroid, at the image plane. The enclosed energy is computed by initially calculating the energy, over the entire image plane, of the Point Spread Function (PSF), which is the image obtained on the focal plane by illuminating the system with an ideal monochromatic wavefront. After determining the PSF centroid, a series of circles, each with an increasing radius, are generated around it, and the PSF energy within each circle is calculated and divided by the total energy. As the circle's radius increases, more of the PSF energy is enclosed within, up until the point where the circle is large enough to wholly encompass all the PSF energy. The encircled energy curve therefore ranges from zero to one. The ensquared energy, which will be considered in this context, is a common alternative to encircled energy and is mostly used in digital imaging cameras with pixels, as their shape is squared.

Figure 5.4 displays the enclosed energy for all the analysed field points at the wavelength λ = 0.550 μm for the VIS/near-IR configuration and at the wavelength λ = 1.400 μm for the IR configuration. One can note that the curves never reache the unit value within the 5 μm representative of the pixel half-side, supporting the fact that the system's performance is not optimal and restrained by geometric aberrations.

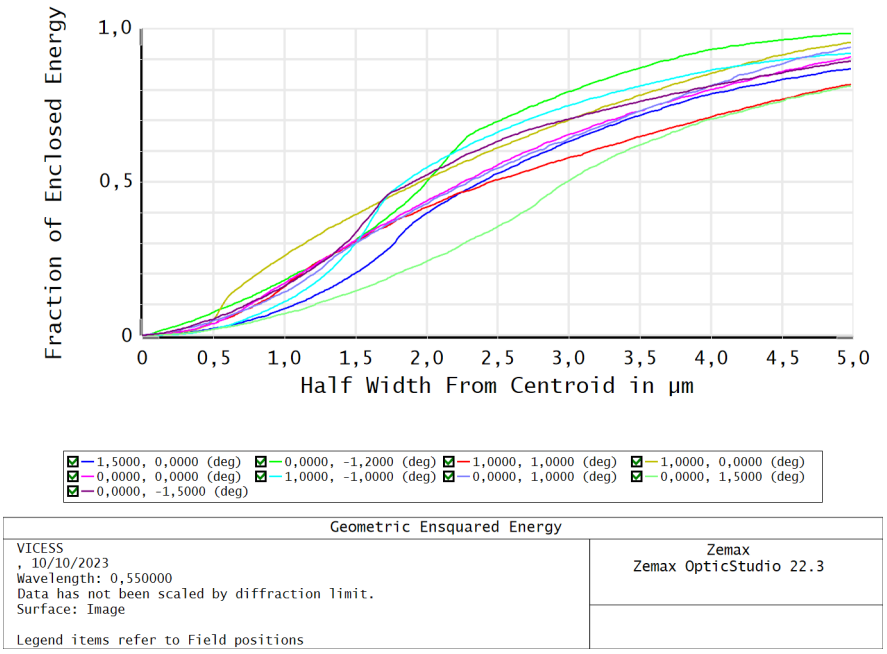

(a) Enclosed Energy Diagram for the VIS/near-IR configuration. The half-distance from centroid is set at 5 μm, as the pixel half-side.

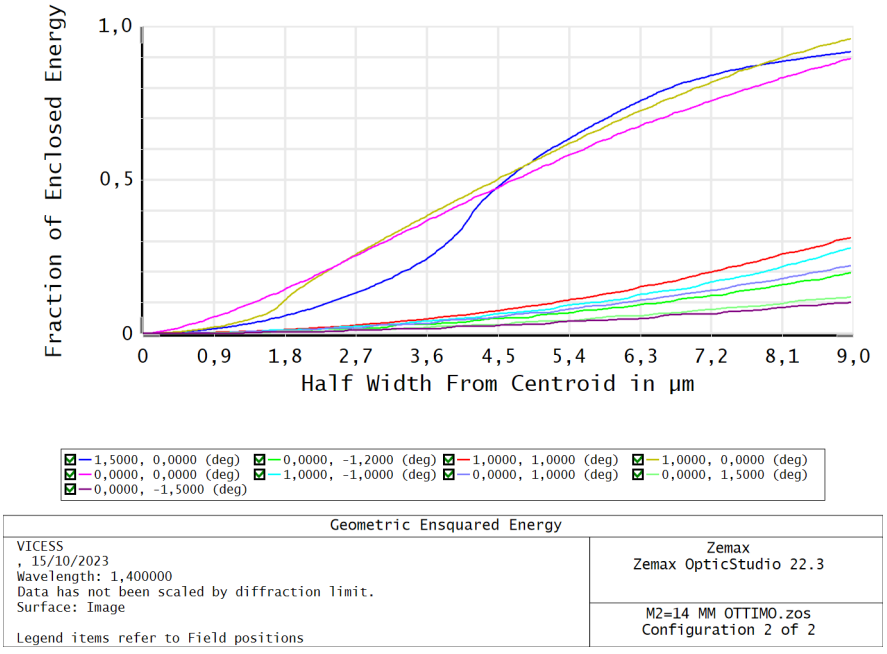

(b) Enclosed Energy Diagram for the IR configuration. The half-distance from centroid is set at 9 μm, as the pixel half-side.

Figure 5.4: Enclosed Energy Diagrams.

5.1.2 Zernike freeform overlay integration

Once the starting geometry has been established, the Zernike polynomial surfaces can be incorporated into the mirrors in order to address the aberration correction. In Chapter 4, the Nodal Aberration Theory has been used to predict the net aberration fields produced by adding each Zernike term to an optical surface anywhere in the system, and then plot these aberrations fields in the Full-Field Displays (FFDs).
Therefore, the integration of the Zernike surfaces has been guided by the visual comparison between the FFDs generated by the software Zemax-OpticStudio[2] for the starting design and the FFDs associated to the specific Zernike overlays, which have been normalized and decentered as the mirrors' apertures. The Zernike terms have been introduced as variable and then optimized by the software; since multiple terms induce also some tilt and defocus, the focal plane position from the dichroic and tilt around the x-axis have also been treated as variables during the optimization, in order to allow some small adjustments as the Zernike terms are added to the surface sag. All Zernike terms introduced at one point in the optimization were kept variable in the subsequent steps. The optimization has been performed considering just the VIS/near-IR configuration, as it is the most critical for what concerns the performance, but the IR configuration benefited from the inclusion of the Zernike terms as well, as both of the channels share the same feeding telescope. The optimization goal is to pursue the smallest geometric size of the spots at the image plane, that reflects in the minimization of the overall aberration.

Firstly, the plots depicting astigmatism, coma and defocus reported in Figure 5.5 were analysed to identify the limiting aberration. Astigmatism seemed to have the greatest impact, as indicated by the average aberration value and the plot scale reported in the plot descriptive captions.

[2]The FFDs in OpticStudio are based on a wavefront fit performed with the Zernike Standard polynomial set, therefore some terms might differ in their order with respect to the FRINGE set, discussed previously. See the Zemax-OpticStudio User Manual for the conversion.

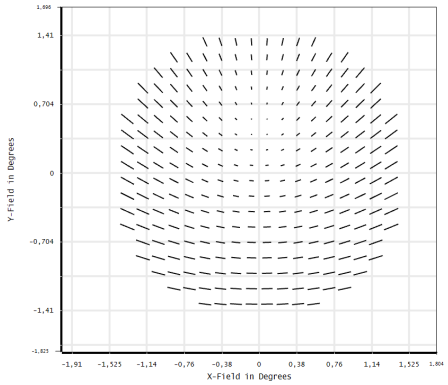

Primary Astigmatism	
VICESS , 26/09/2023 Wavelength: 0,4000 µm Decomposition: Zernike Max Term: 37 Average: 0,0412 waves Display: Absolute Field: Elliptical Plot scale: 0,0000 to 0,1460	Zemax Zemax OpticStudio 22.3

(a) Astigmatism

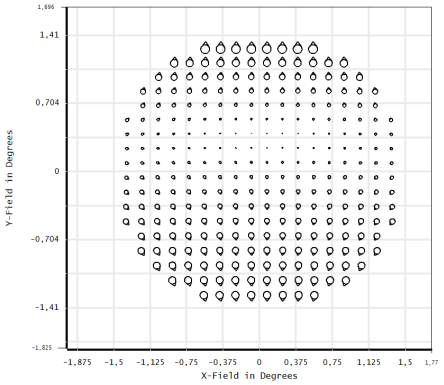

Primary Coma	
VICESS , 26/09/2023 Wavelength: 0,4000 µm Decomposition: Zernike Max Term: 37 Average: 0,0055 waves Display: Absolute Field: Elliptical Plot scale: 0,0000 to 0,0457	Zemax Zemax OpticStudio 22.3

(b) Coma

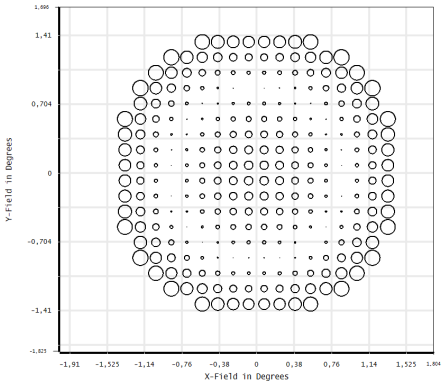

Defocus	
VICESS , 26/09/2023 Wavelength: 0,4000 µm Decomposition: Zernike Max Term: 37 Average: -0,0235 waves Display: Absolute Field: Elliptical Plot scale: 0,0000 to 0,1043	Zemax Zemax OpticStudio 22.3

(c) Defocus

Figure 5.5: Initial aberrations.

The Z_5 term has been introduced as a variable, attempting to subtract a constant contribution in astigmatism, thus reducing a bit the plot scale. The most satisfactory outcome was achieved by incorporating this term into the primary mirror, M1. The resulting astigmatism FFD, Spot Diagram and Ensquared Energy, after the optimization performed by the software, are shown in Figures 5.6, 5.7 and 5.8. The overall improvement in the spots depicted in the Spot Diagram is not so significant, as some show improvement while others worsen slightly. This behaviour is also reflected in the Enclosed Energy Diagram. Unfortunately, deriving an absolute "averaged" information from the FFDs is not feasible, as the average aberration value is calculated considering the various contributions with signs, resulting in a practically null value; nevertheless, the FFD plot scale for astigmatism demonstrates a slight reduction in magnitude, the node is now on axis ant the FFD is more symmetric. Consequently, it has been decided to keep this term into the freeform overlay.

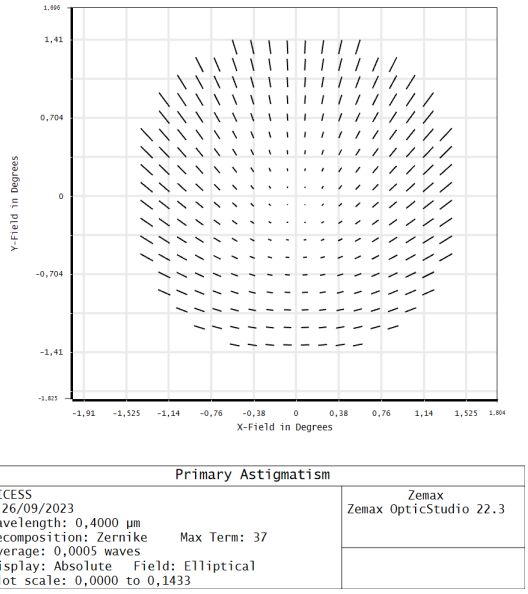

Figure 5.6: FFD of astigmatism after the introduction of a Z_5 Zernike overlay to the primary mirror.

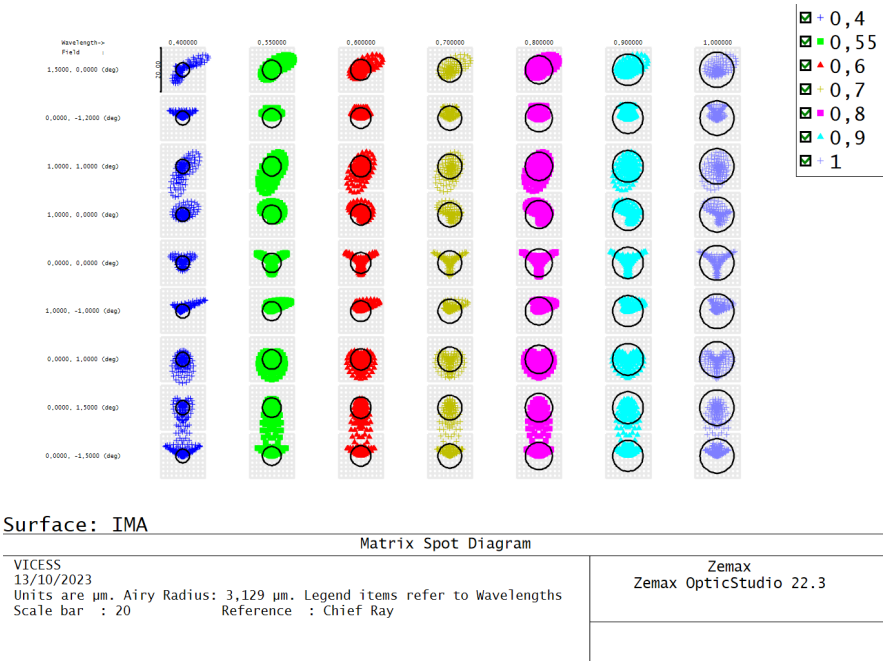

Figure 5.7: Matrix Spot Diagram after the introduction of a Z_5 Zernike overlay to the primary mirror. The scale bar is set at 20 μm.

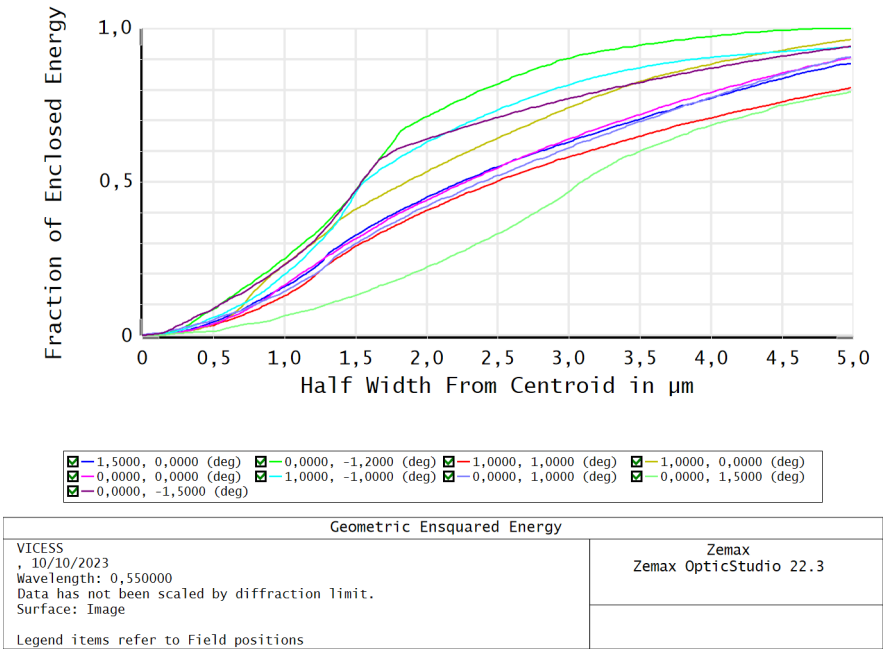

Figure 5.8: Enclosed Energy Diagram after the introduction of a Z_5 Zernike overlay to the primary mirror. The half-distance from centroid is set at 5 μm, as the pixel half-side.

Coma and defocus are not altered by the introducion of a Zernike astigmatism term, so the optimization has proceeded focusing again on astigmatism. The FFD displays a pattern that can be associated with a Zernike coma overlay placed away from the stop. On the basis of the pattern orientation, the term Z_8 has been introduced on both the primary and the tertiary mirrors. The resulting FFDs for astigmatism and coma, the Spot Diagram and the Enclosed Energy Diagram, after the software optimization, are shown in Figures 5.9, 5.10and 5.11. While coma is almost unaffected, in its plot scale, by the optimization, it can be seen that astigmatism underwent an important reduction, and its contribution is small in a good portion of the FoV.

The Spot Diagram has improved as well, even though some fields display a greater progress than others.

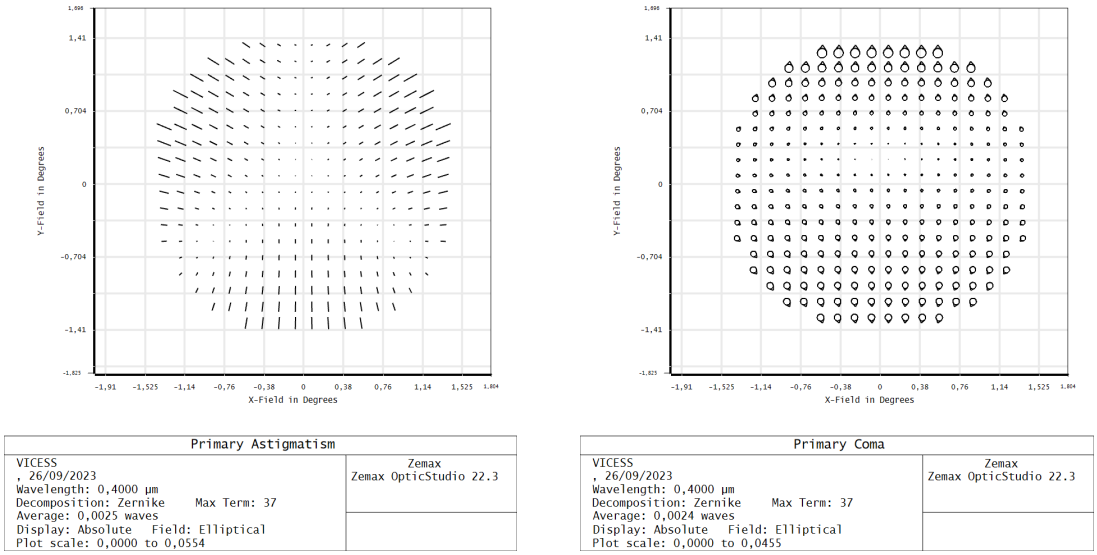

(a) Astigmatism **(b)** Coma

Figure 5.9: Resulting astigmatism and coma after the introduction of a Z_8 Zernike overlay to the primary and tertiary mirrors.

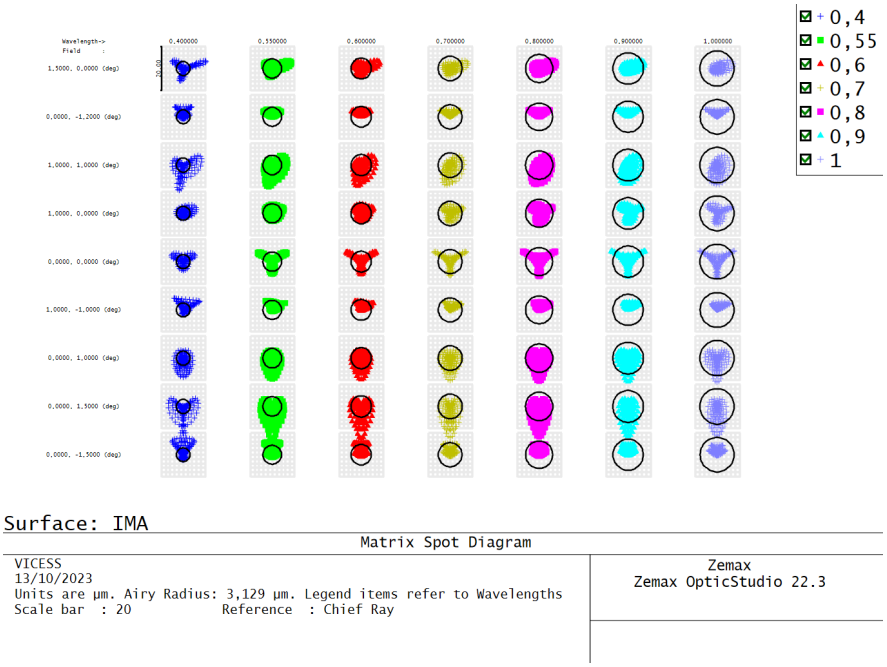

Figure 5.10: Matrix Spot Diagram after the introduction of a Z_8 Zernike overlay to the primary and tertiary mirrors. The scale bar is set at 20 μm.

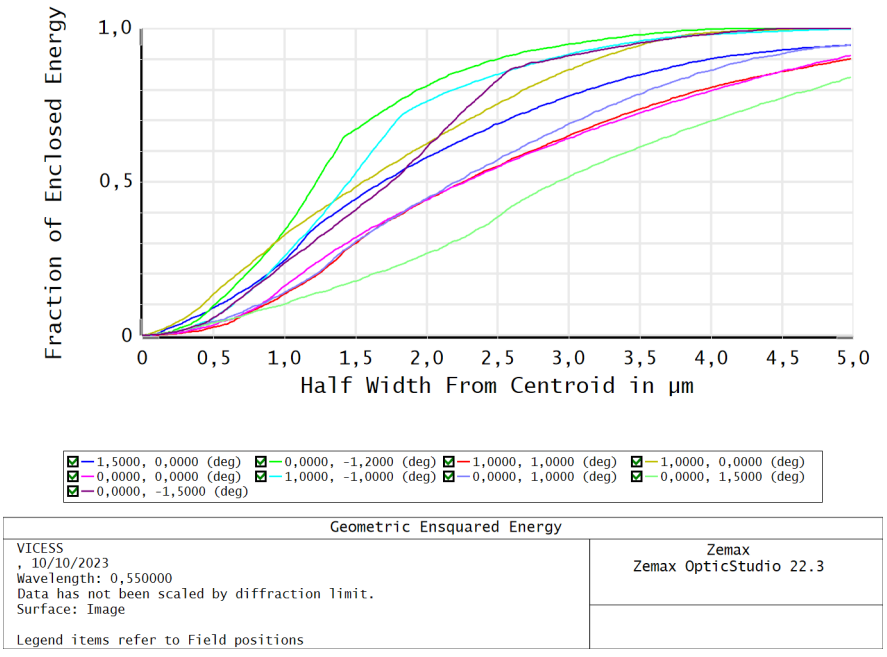

Figure 5.11: Enclosed Energy Diagram after the introduction of a Z_8 Zernike overlay to the primary and tertiary mirrors. The half-distance from centroid is set at 5 μm, as the pixel half-side.

At this point, the FFD pattern for astigmatism hints the introduction of a trefoil overlay away from the stop. Additionally, the FFD for trefoil displays an important contribution of this aberration to the overall aberration field, as can be seen in Figure 5.13 (a).
Therefore, a Z_{11} Zernike overlay has been placed on both the primary and tertiary mirrors, resulting in the plots displayed in Figures 5.12 and 5.13. The plot scale of the FFD for astigmatism has decreased a bit, while the plot scale for coma has slightly increased, even though the pattern has remained unchanged. In Figure 5.13 it can be seen that the introduction of a constant trefoil contribution also helped in reducing the trefoil itself, as the plot scale of the FFD has become a third of the initial one. This probably led to the dramatic improvement in the Spot Diagram in Figure 5.14, where the spots have visibly shrinked for almost all fields and wavelengths.
In the Enclosed Energy Diagram in Figure 5.15, the curves now approach the unit value more rapidly.

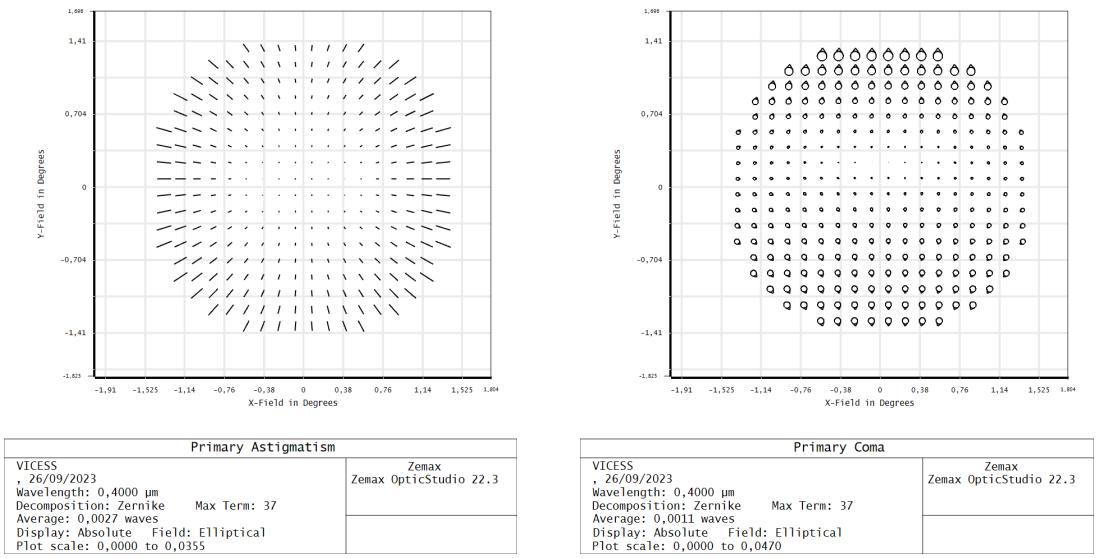

(a) Astigmatism **(b)** Coma

Figure 5.12: Resulting astigmatism and coma after the introduction of a Z_{11} Zernike overlay to the primary and tertiary mirrors.

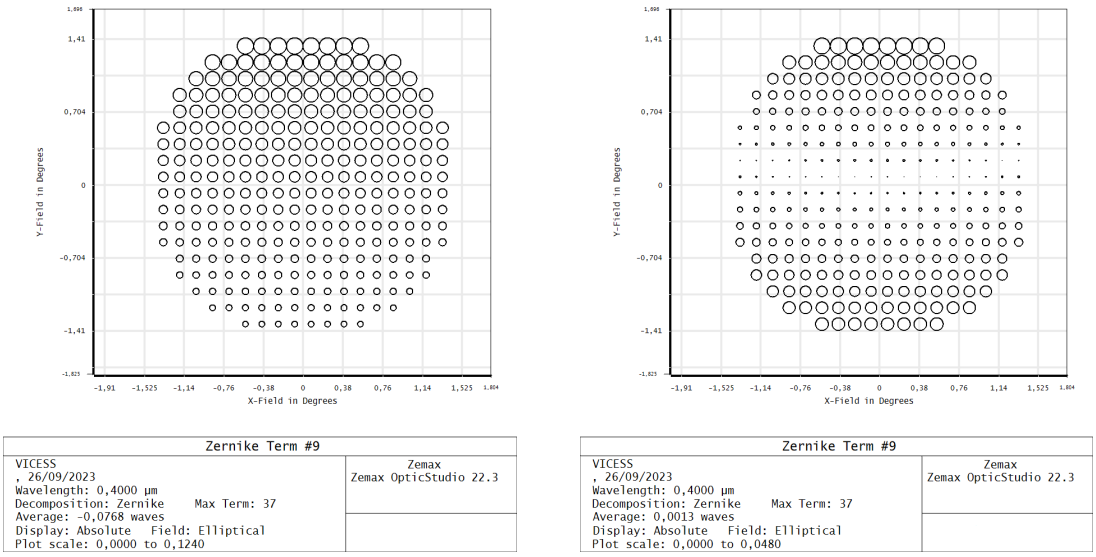

(a) Trefoil before the introduction of a Z_{11} term.

(b) Trefoil after the introduction of a Z_{11} term.

Figure 5.13: Trefoil correction.

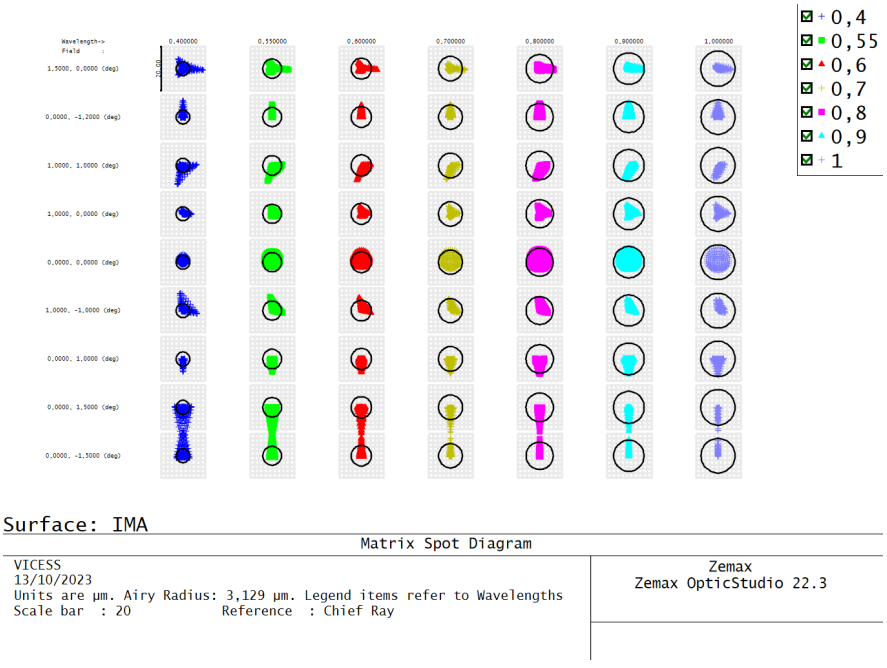

Figure 5.14: Matrix Spot Diagram after the introduction of a Z_{11} Zernike overlay to the primary and tertiary mirrors. The scale bar is set at 20 μm.

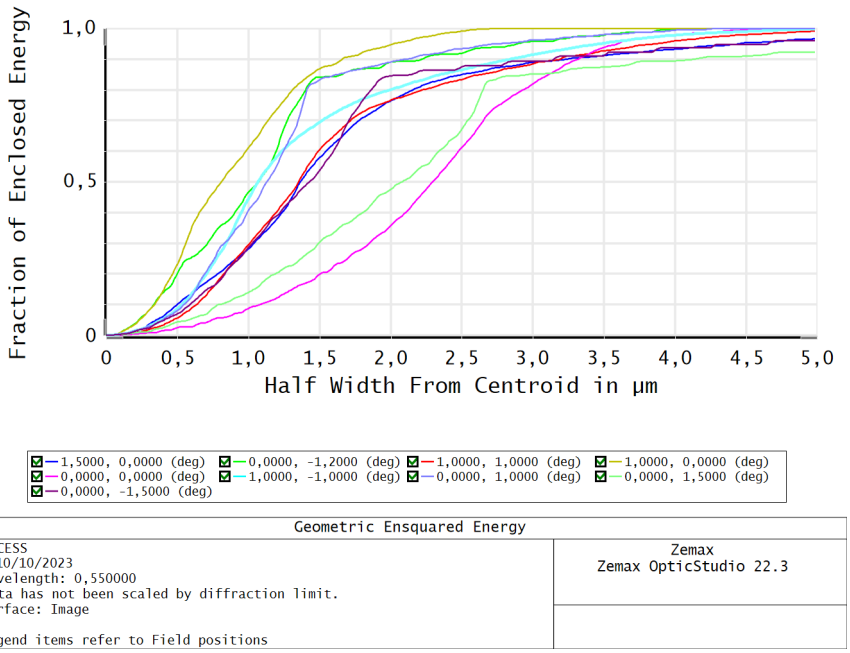

Figure 5.15: Enclosed Energy Diagram after the introduction of a Z_{11} Zernike overlay to the primary and tertiary mirrors. The half-distance from centroid is set at 5 μm, as the pixel half-side.

On the basis of these FFD patterns, it is suggested that a secondary coma overlay away from the stop might be beneficial, therefore a Z_{12} Zernike term has been added to the primary and tertiary mirrors. The induced aberrations and the resulting Spot Diagram are depicted in Figures 5.16 and 5.17. Coma has undergone significant reduction in plot scale, more than halving in size, while Figure 5.17 shows a slight increase in the secondary coma contribution. In the Spot Diagram, in Figure 5.18, the spots now have a mostly circular shape, but the usual coma pattern is still evident in the (0.500, 0.000) and (0.000, 1.000) fields. Astigmatism and defocus, which are the other two aberrations affected by the introduction of a Z_{12} term away from the stop, do not change significantly. The Enclosed Energy Diagram in Figure 5.19 displays a great improvement, except for the on axis field, that seems to remain unchanged.

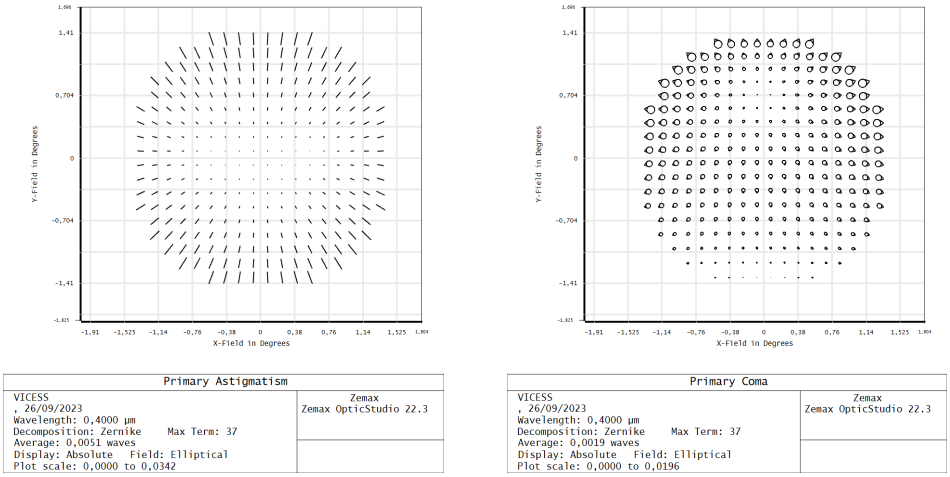

(a) Astigmatism **(b)** Coma

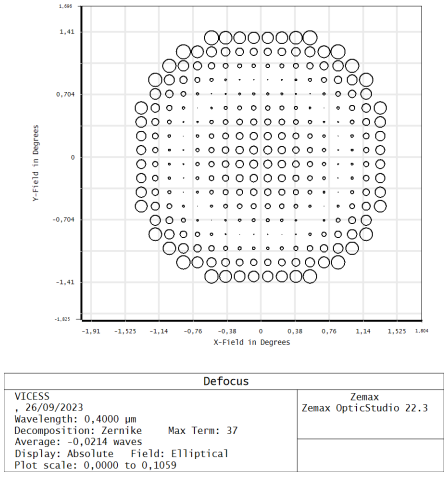

(c) Defocus

Figure 5.16: Resulting astigmatism and coma after the introduction of a Z_{12} Zernike overlay to the primary and tertiary mirrors.

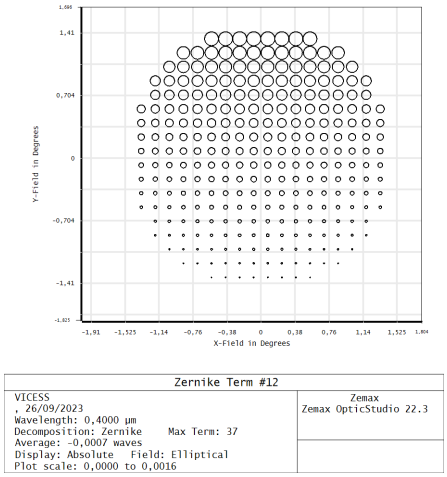

(a) Secondary coma before the introduction of a Z_{12} term.

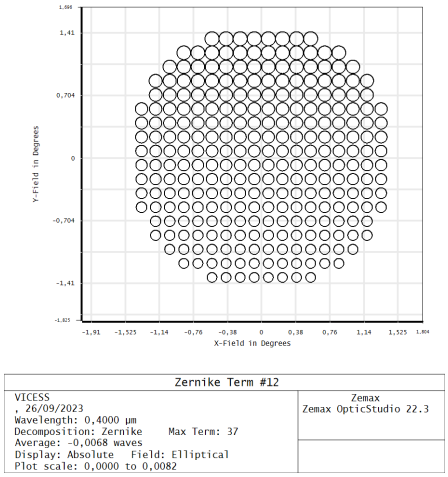

(b) Secondary coma after the introduction of a Z_{12} term.

Figure 5.17: Secondary coma contribution.

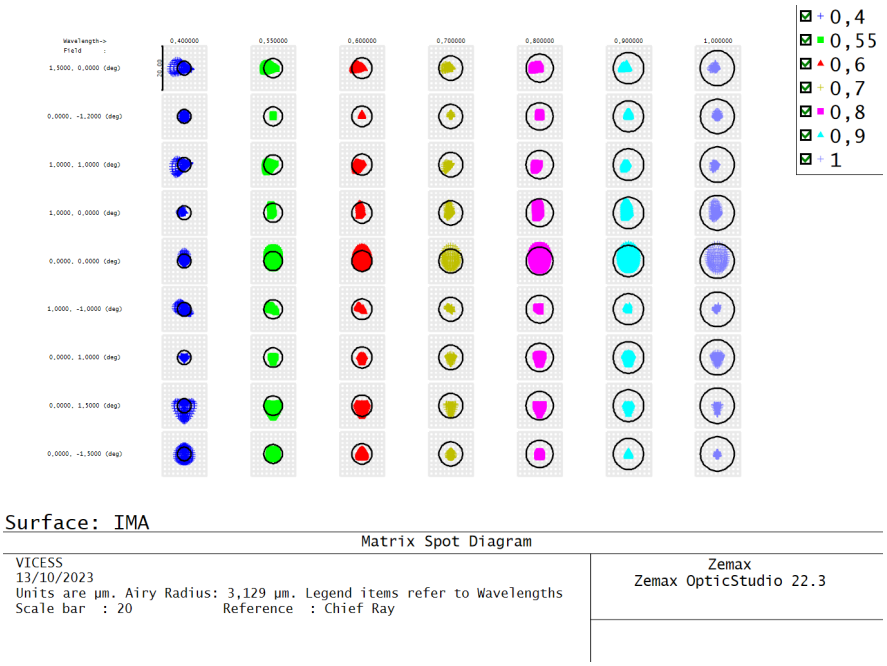

Figure 5.18: Matrix Spot Diagram after the introduction of a Z_{12} Zernike overlay to the primary and tertiary mirrors. The scale bar is set at 20 μm.

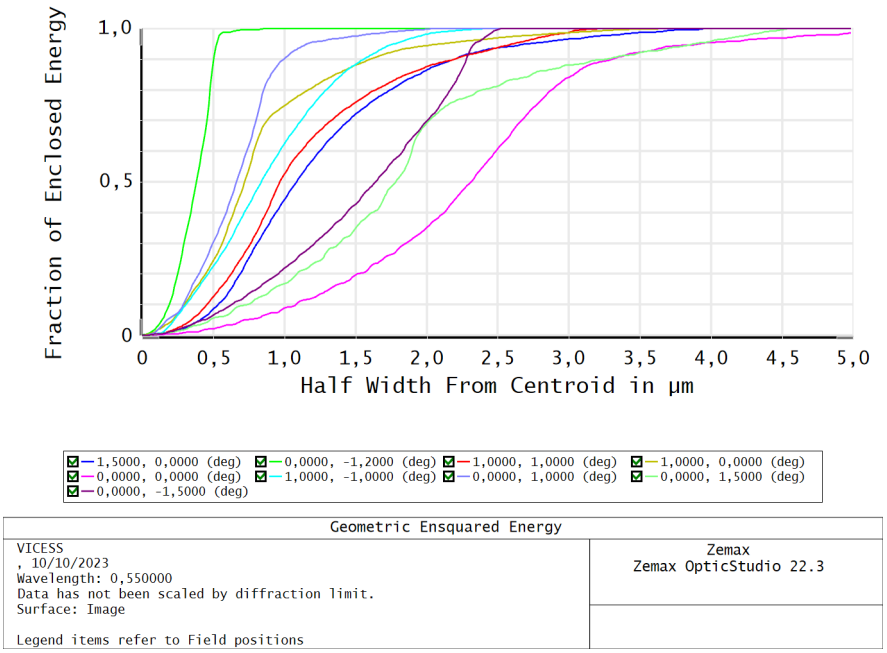

Figure 5.19: Enclosed Energy Diagram after the introduction of a Z_{12} Zernike overlay to the primary and tertiary mirrors. The half-distance from centroid is set at 5 μm, as the pixel half-side.

In the final step, both the residual astigmatism and coma are addressed with a spherical aberration term Z_9, introduced in all the three mirrors. In Figure 5.20 one can see that while the astigmatism increases a bit in its scale, coma and defocus are drammatically reduced, thus leading to the improvement in the Spot Diagram that can be seen in Figure 5.21. The vertical edges of the FoV, corresponding to fields (0.000, 1.500) and (0.000,−1.500) still suffer some of the residual contribution of aberrations, but only at the shortest wavelength (λ = 0.400 μm). In the Enclosed Energy Diagram, the curves are now closer together, suggesting a more homogeneous performance across the various fields. Additionally, each curve reaches the unit value within the space of a single pixel.

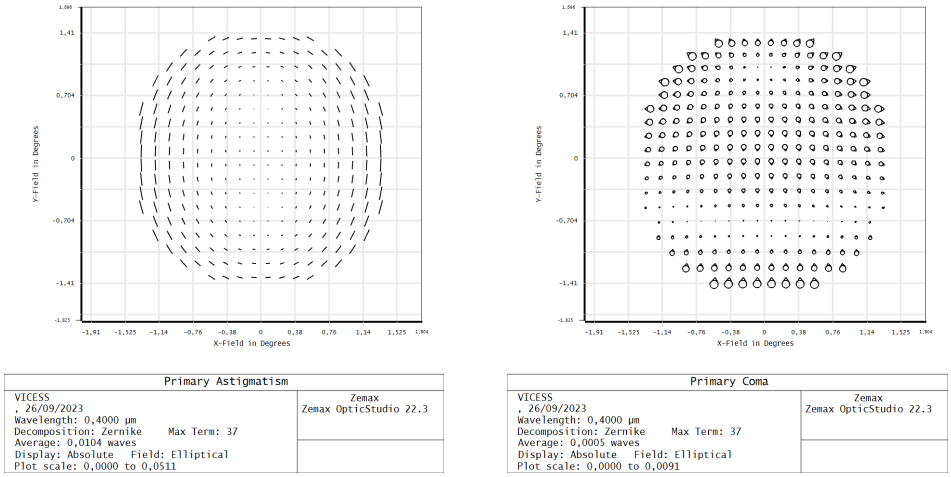

(a) Astigmatism **(b)** Coma

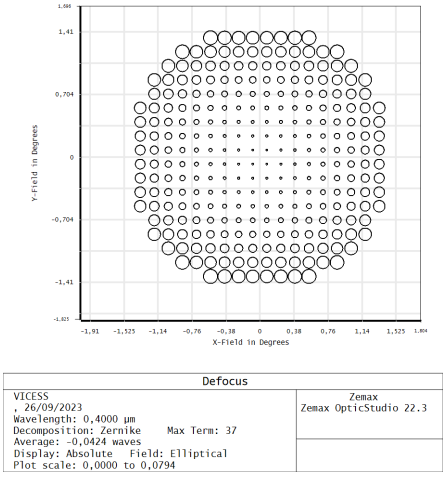

(c) Defocus

Figure 5.20: Resulting astigmatism, coma and Defocus after the introduction of a Z_9 Zernike overlay to all the mirrors.

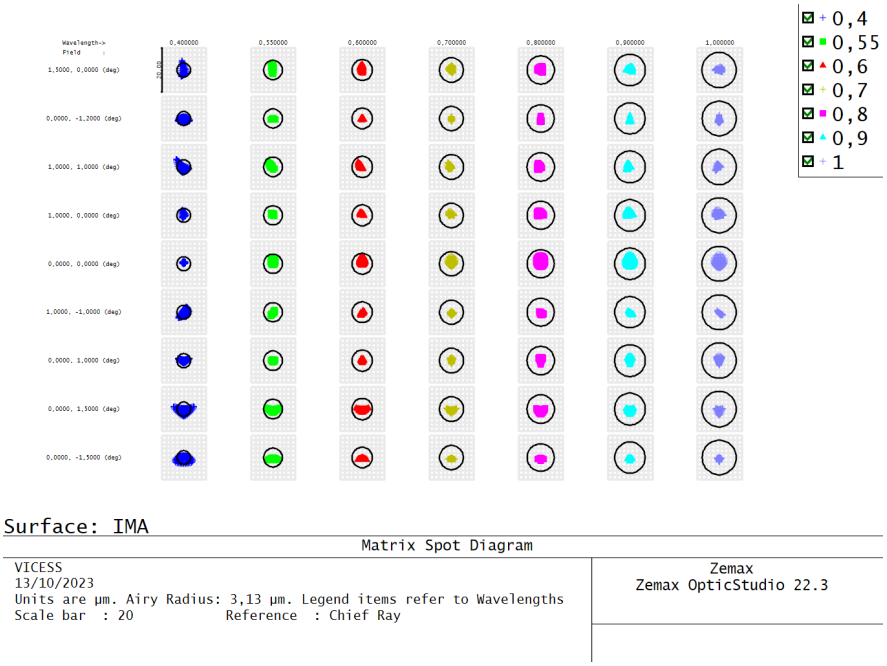

Figure 5.21: Matrix Spot Diagram after the introduction of a Z_9 Zernike overlay to all the mirrors. The scale bar is set at 20 μm.

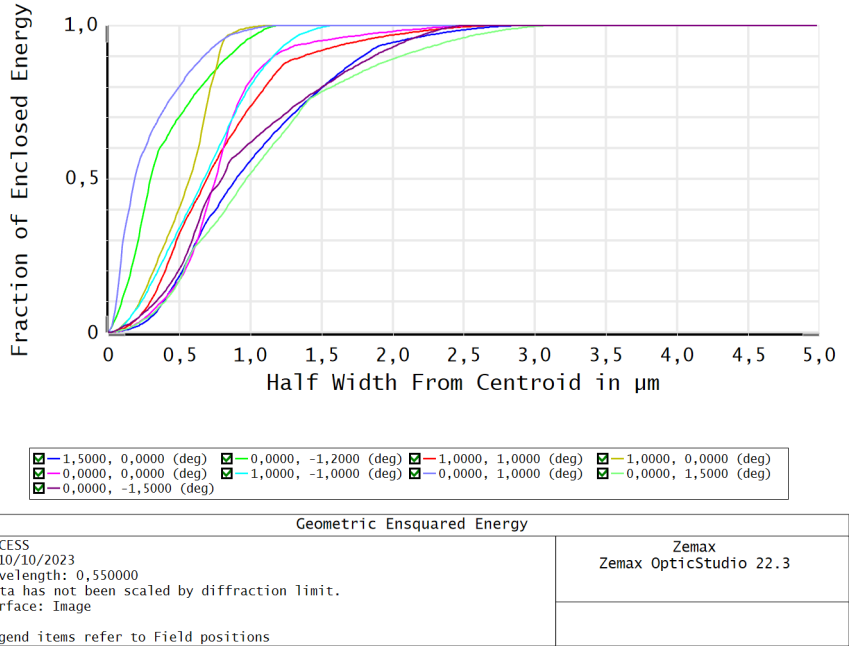

Figure 5.22: Enclosed Energy Diagram after the introduction of a Z_{12} Zernike overlay to all the mirrors. The half-distance from centroid is set at 5 μm, as the pixel half-side.

5.1.3 Final results and comparison

After the final optimisation, the Zernike coefficients describing the freeform overlay on each mirror are summarised in Table 5.3. Following the NAT, only the coefficients that were genuinely suitable for optimising the instrument's performance were introduced to prevent over-complicating the system. The distance of the focal planes from the filter wheels has been kept fixed for both configurations, while the distance of the wheels from the dichroic was free to adjust during optimization, as well as the focal planes tilt. The final parameters are listed in Table 5.4.

Surface	**M1**	**M2**	**M3**
$\mathbf{Z}_5$	$-5.983732\ 10^{-5}$	-	-
$\mathbf{Z}_8$	$5.499856\ 10^{-5}$	-	$-1.325921\ 10^{-5}$
$\mathbf{Z}_9$	$-4.553406\ 10^{-5}$	-1.77835310^{-5}	$-5.351964\ 10^{-5}$
$\mathbf{Z}_{11}$	$-6.920795\ 10^{-5}$	-	$-1.108046\ 10^{-5}$
$\mathbf{Z}_{12}$	$2.082118\ 10^{-5}$	-	$-4.660046\ 10^{-5}$

Table 5.3: Zernike coefficients and final parameters for the VICESS-like instrument.

Surface	**Dichroic**	**Focal Plane**
Distance from the next surface (mm)	-38.4757	-
	40.8493	-
Tilt about x (°)	0.0000	-4.6146
	0.0000	-4.3951

Table 5.4: Zernike coefficients and final parameters for the VICESS-like instrument.

For what concerns the system improvement, the most explicative diagram is certainly the Spot Diagram, reported in its matrix form for both the VIS/near-IR and the IR configurations, in Figures 5.23 and 5.24. To further emphasise the improved performance achieved following the introduction of the freeform optics, the initial and final Spot Diagrams are

presented in sequence and with the same scale bar, for better comparison. The system is diffraction-limited over practically the whole covered spectrum, with the only exception of the outermost fields at the shortest wavelengths, where the geometrical aberrations slightly exceed the diffraction limit. The spots are all included within the Airy Radius, except those associated with the shorter wavelength λ = 0.400 μm, which still suffer a bit of astigmatism, especially at the extreme points of the field of view. Spots for longer wavelengths, for both configurations, are well below the diffraction limit.

The Enclosed Energy Diagrams before and after the introduction of the Zernike overlay are presented, for both configurations, in Figures 5.25 and 5.26. For the VICESS-like instrument, the improvement is evident, and it can be seen that the 100% of the PSF energy falls within the pixel dimension, which is 10 μm for the VIS/near-IR sensor and 18 μm for the IR sensor.

The spatial resolution for both configurations has improved with respect to the resolution of the original instrument, thanks to the longer focal length. Tables 5.5 and 5.6 report the ideal resolution that such instrument can obtain observing a target at a 10 km distance. Since the instrument is diffracion-limited, this value is provided by the projection of the Airy Radius (which is in turn a function of wavelength, as shown in Equation 3.1) on the target, computed according to the following Equation:

$$\frac{\text{Airy Radius}(\lambda)}{\text{focal length}} = \frac{\Delta x}{\text{Distance from the object}} \tag{5.1}$$

In effect this is the resolution limit, which can be achieved with an ideal sensor. However, in practice, Nyquist's theorem must be taken into account. This means that the minimum resolving element that can be obtained is equal to two pixels. Therefore, if the sensor has pixels with 10 μm sides, the minimum resolving element will be 20 μm, which is significantly higher than what is presented in Tables 5.5 and 5.6.

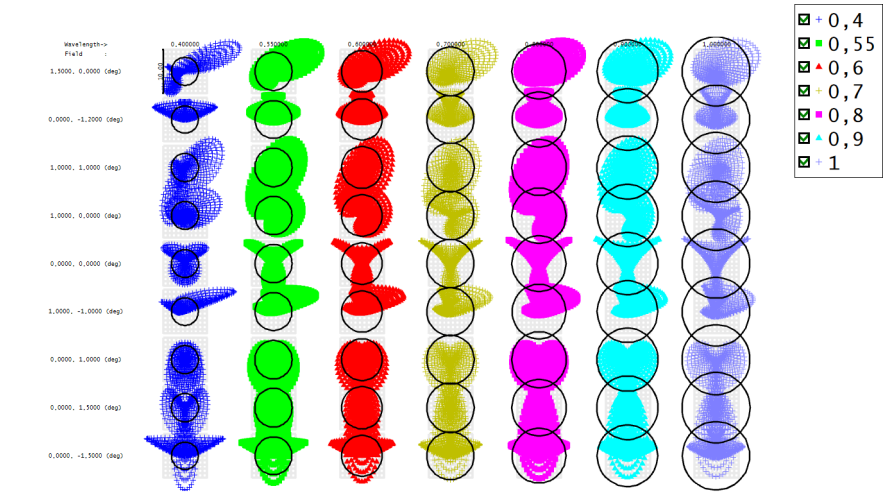

Surface: IMA

Matrix Spot Diagram	
VICESS 01/10/2023 Units are µm. Airy Radius: 3,129 µm. Legend items refer to Wavelengths Scale bar : 10 Reference : Chief Ray	Zemax Zemax OpticStudio 22.3

(a) Matrix Spot Diagram for the VIS/near-IR configuration before introducing the Zernike polynomial terms to the mirrors.

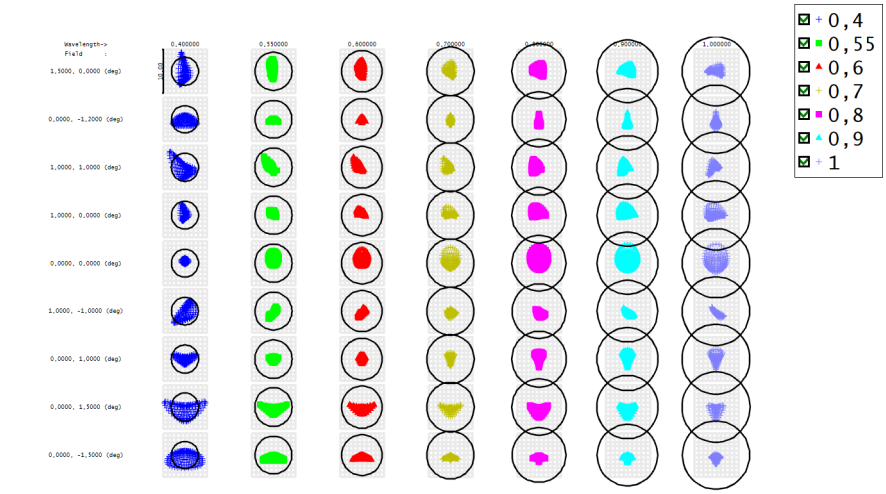

Surface: IMA

Matrix Spot Diagram	
VICESS 30/09/2023 Units are µm. Airy Radius: 3,13 µm. Legend items refer to Wavelengths Scale bar : 10 Reference : Chief Ray	Zemax Zemax OpticStudio 22.3

(b) Matrix Spot Diagram for the VIS/near-IR configuration after introducing the Zernike polynomial terms to the mirrors.

Figure 5.23: Matrix Spot Diagrams for the VIS/near-IR configuration, displayed for eight field points and a wavelength range from 0.400 to 1.000 μm. The scale bars are both set at 10 μm.

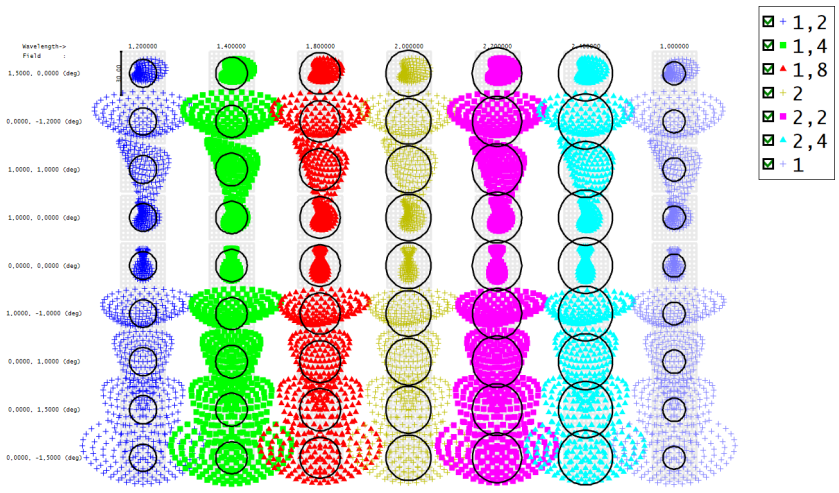

Surface: IMA

Matrix Spot Diagram	
VICESS 01/10/2023 Units are µm. Airy Radius: 9,388 µm. Legend items refer to Wavelengths Scale bar : 30 Reference : Chief Ray	Zemax Zemax OpticStudio 22.3

(a) Matrix Spot Diagram for the IR configuration before introducing the Zernike polynomial terms to the mirrors.

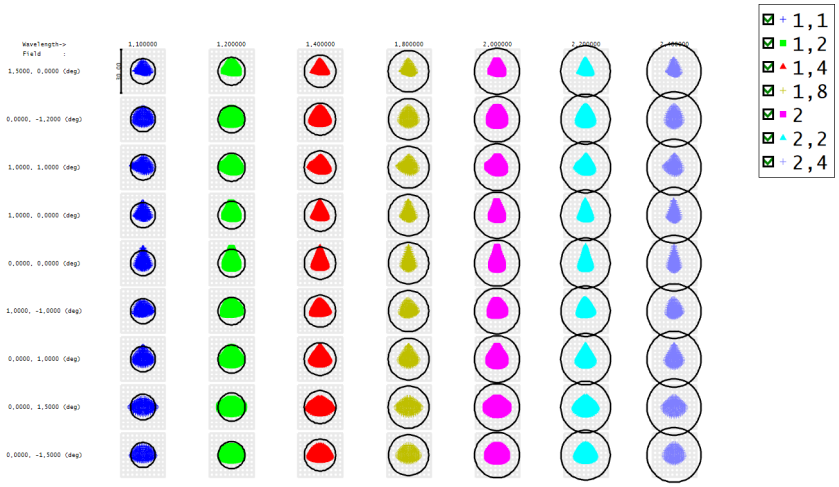

Surface: IMA

Matrix Spot Diagram	
VICESS 30/09/2023 Units are µm. Airy Radius: 8,607 µm. Legend items refer to Wavelengths Scale bar : 30 Reference : Chief Ray	Zemax Zemax OpticStudio 22.3

(b) Matrix Spot Diagram for the IR configuration after introducing the Zernike polynomial terms to the mirrors.

Figure 5.24: Matrix Spot Diagrams for the IR configuration, displayed for eight field points and a wavelength range from 1.100 to 2.400 μm. The scale bars are both set at 30 μm.

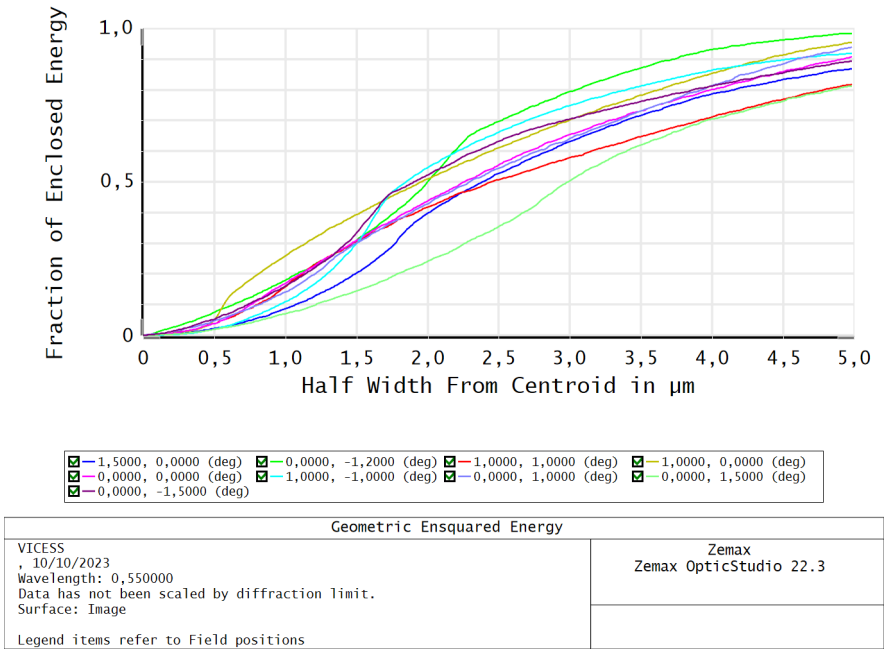

(a) Enclosed Energy Diagram for the VIS/near-IR configuration before introducing the Zernike overlay to the mirrors.

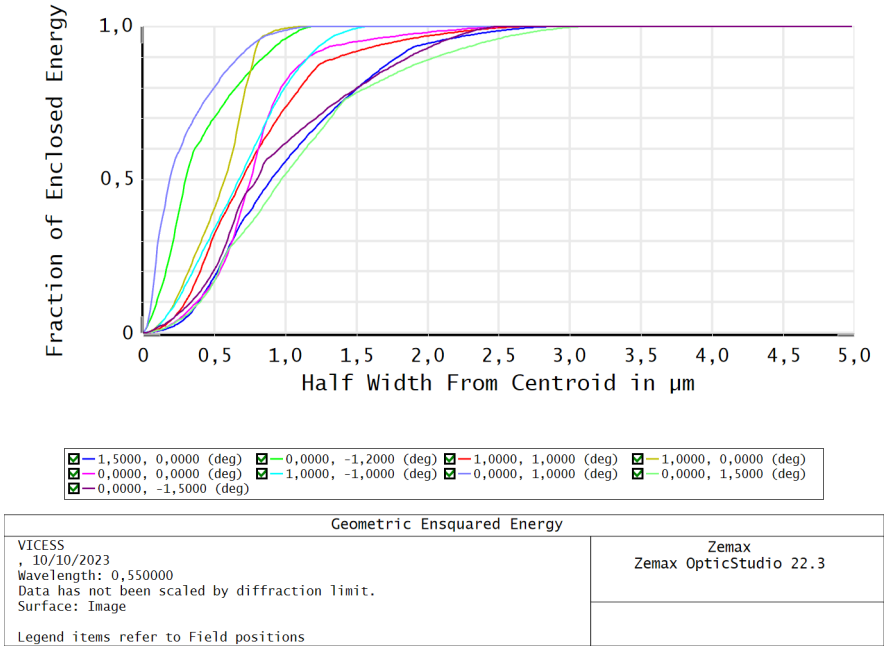

(b) Enclosed Energy Diagram for the VIS/near-IR configuration after introducing the Zernike overlay to the mirrors.

Figure 5.25: Enclosed Energy Diagrams for the VIS/near-IR configuration, plotted for all the analysed field points at the same wavelength λ = 0.550 μm. The half-distance from centroid is set at 5 μm, as the pixel half-side.

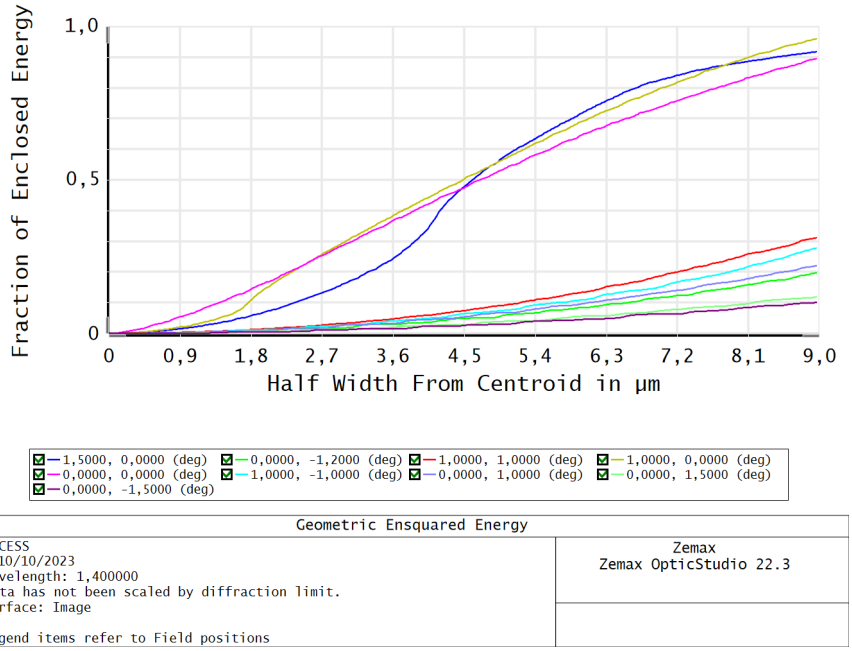

(a) Enclosed Energy Diagram for the IR configuration before introducing the Zernike overlay to the mirrors.

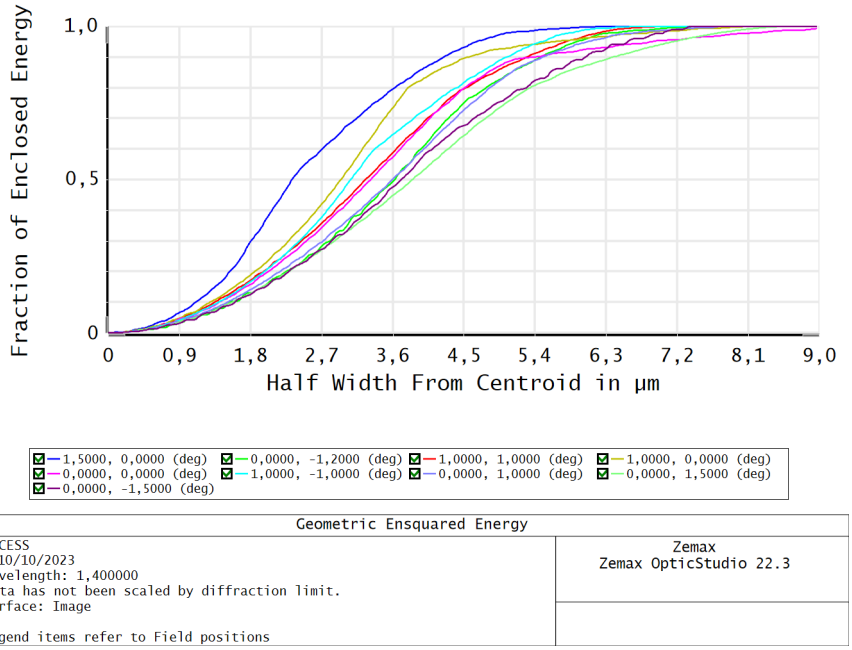

(b) Enclosed Energy Diagram for the IR configuration after introducing the Zernike overlay to the mirrors.

Figure 5.26: Enclosed Energy Diagrams for the IR configuration, plotted for all the analysed field points at the same wavelength $\lambda = 1.400$ μm. The half-distance from centroid is set at 9 μm, as the pixel half-side.

VIS/NIR Conf.	Wavelength (μm)	Airy Radius (μm)	Resolution Δx (m/pixel)
-	0.4000	3.1297	0.0835
-	0.5500	4.3034	0.1148
-	0.6000	4.6946	0.1252
-	0.7000	5.4771	0.1461
-	0.8000	6.2595	0.1669
-	0.9000	7.0419	0.1878
-	1.0000	7.8244	0.2087

Table 5.5: Airy disk radius and ideal resolution as function of wavelength, for the VIS/near-IR configuration, with a focal length of 375 mm and a distance from the object of 10 km.

IR Conf.	Wavelength (μm)	Airy Radius (μm)	Resolution Δx (m/pixel)
-	1.1000	8.6068	0.2295
-	1.2000	9.3892	0.2504
-	1.4000	10.9541	0.2921
-	1.8000	14.0839	0.3756
-	2.0000	15.6487	0.4173
-	2.2000	17.2136	0.4590
-	2.4000	18.7785	0.5008

Table 5.6: Airy disk radius and ideal resolution as function of wavelength, for the IR configuration, with a focal length of 375 mm and a distance from the object of 10 km.

5.2 HYPSOS-like instrument

5.2.1 Preliminary design adjustments

To meet the requirements of a possible lunar mapping mission, the geometry of HYPSOS has needed far more drastic modifications than VICESS. The requirements have been developed assuming to operate in a polar orbit at an altitude of 100 km above the ground. Table 5.7 displays the derived optical parameters for the telescope, the slit geometry and the pixel size at the Focal Plane.

Parameter	Requirement
Focal length	120 (mm)
Aperture diameter	40 (mm)
f/#	3
Field of view per Channel	4°
Spatial sample	30 m
Pixel size	$18 \times 18\ \mu m^2$
Bin size (2×2 binning)	$36 \times 36\ \mu m^2$
Detector	Teledyne, HAWAII 2RG (2048×2048 pixels)

Table 5.7: Optical parameters and requirements.

Firstly, the layout has been re-optimized and adjusted to achieve the required aperture and focal length without vignetting part of the incoming beams. Then, the system has been altered by eliminating one Entrance Folding Mirror and doubling the tilt of the other with respect to the y-axis. In the original configuration the two beams necessary for stereo-imaging were collected at $\pm$ 20° with respect to Nadir, along the flight direction, while in the modified configuration one beam (Channel 1) is collected at + 40° from Nadir and the other one is collected at Nadir (Channel 2). For the stereo-imaging purposes, this is absolutely equivalent. In order to obtain a lighter and simpler system and prevent absorption-related issues, the Schmidt-Pechan field rotators have been removed. However, to combine the fields of view

from both Channels into a single slit, the alignment of the two images to the Focal Plane has been made vertical instead of horizontal, as it was in the original configuration. The Entrance Folding Mirror (EFM) has been tilted of 2° around the local x-axis to slightly offset one entering beam, in order to focus it on top of the other one at the image plane. The two images are separated by a 3 mm distance. Figure 5.27 shows the footprints of the aligned fields at the image plane for the original and the modified configurations.

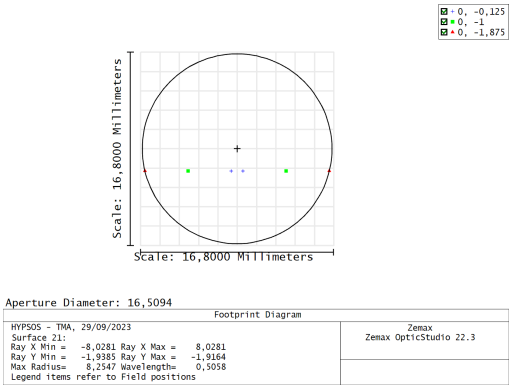

(a) Footprint diagram of the original configuration.

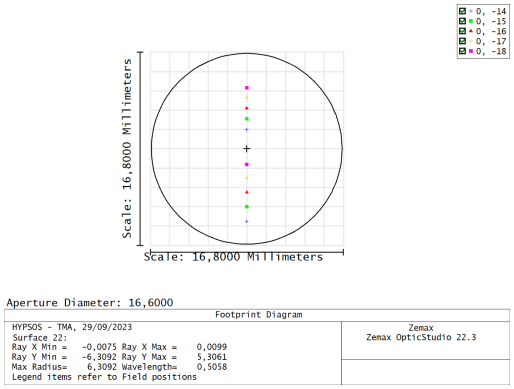

(b) Footprint diagram of the modified configuration.

Figure 5.27: Footprint diagrams at the Focal Plane.

Figure 5.28 displays the final layout of the HYPSOS-like instrument. Both beams associated to the two stereo Channels impinge on the same primary (M1) and tertiary (M3) Mirrors, while the secondary Mirror (M2), which is also shared, presents two different apertures with a 17.20 mm diameter, that are horizontally decentered by 12 mm with respect to the optical axis, to avoid cross-talk between the Channels. Each of these aperture serve as a stop for a Channel. A rectangular Flat Mirror (FM), which will probably be substituted by a dichroic in the future, is then used to fold the image away, almost perpendicularly with respect to the beams incoming direction. A spectrometer in modified Offner configuration will gather the light from the Slit (S), placed at the Focal Plane. Its study and characterization are not part of this work.

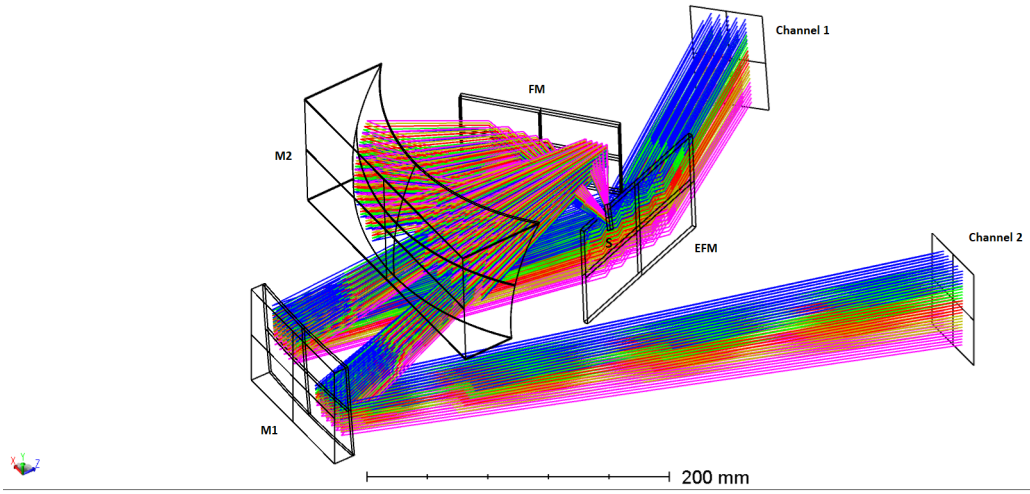

(a) Global view of the final layout of the instrument.

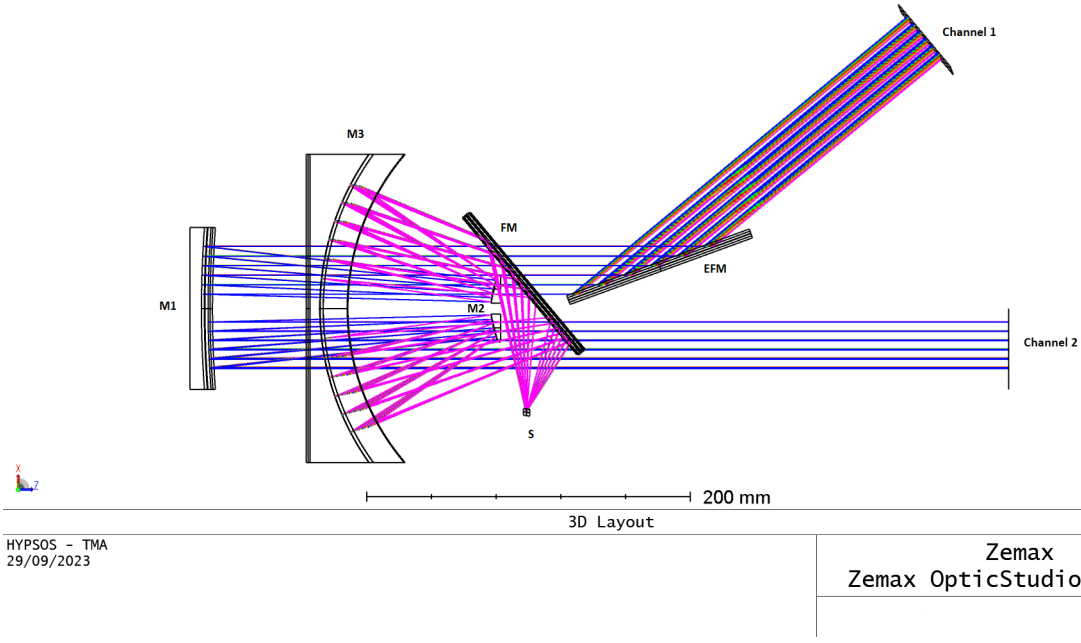

(b) Top view of of the final layout of the instrument.

Figure 5.28: HYPSOS-like intrument layout.

Tables 5.8 and 5.9 summarize the optical parameters of the final system, for both Channels. The values given in the Tables result from the optimisation of the system via ray tracing software; they will need to be redefined during the construction phase, in accordance with optical realisation tolerances and system alignment, according to the demanded performance requirements.

Surface	Entr. Folding Mirror	Mirror-M1	Mirror-M2
Type	Standard	Standard	Standard
Radius (mm)	Infinity	634.0971	55.9655
Distance to next surface (mm)	−200.0000	180.0000	−106.0000
Parent surface diameter (mm)	120.6646	20.0000	118.2796
Aperture x-half width (mm)	60.0000	50.0000	8.6400 (radius)
Aperture y-half width (mm)	40.0000	40.0000	0.0000
Aperture x-decenter (mm)	88.0000	0.0000	12.0000
			−12.0000
Aperture y-decenter (mm)	−90.0000	−60.0000	-
Conic	0.0000	−4.7219	−0.0836
Tilt about x (°)	2.0000	0.0000	0.0000
Tilt about y (°)	70.0000	0.0000	0.0000
Coating	Metal	Metal	Metal

Table 5.8: Optical parameters for the Entrance Folding Mirror, M1 and M2. Note that when two values for the same parameter are reported, they respectively refer to the first and second stereo-Channels.

Surface	Mirror-M3	Folding Mirror	Focal Plane (Slit)
Type	Standard	Standard	Standard
Radius (mm)	168.2666	Infinity	Infinity
Distance to next surface (mm)	140.0000	−70.0000	-
Parent surface diameter (mm)	107.7654	-	-
Aperture x-half width (mm)	95.0000	55.0000	0.01800
Aperture y-half width (mm)	45.0000	30.0000	36.8600
Aperture x-decenter (mm)	0.0000	20.000	-
			-
Aperture y-decenter (mm)	34.0000	30.0000	-
Conic	0.0106	0.0000	-
Tilt about x (°)	−1.5000	0.0000	12.3018
Tilt about y (°)	0.0000	40.0000	79.9996
Coating	Metal	-	-

Table 5.9: Optical parameters for M3, the Folding Mirror and the Focal Plane.

Figure 5.29 displays the Spot Diagram for both Channels. One important thing to note is that spots on the two Channels are different because the instrument configuration is not symmetrical. As the box size measures 1 mm, it is evident that the performance in this configuration is far from acceptable. This fact is also reflected in the enclosed Energy Diagrams, presented in Figure 5.30 for both Channels: for the first Channel, the unit value is reached at a half width from centroid of 300 μm, while for the second Channel it is reached even further, at 450 μm. These values should be comparable to the pixel half-width, which is 9 μm for both Channels.

(a) Spot Diagram for the first Channel.

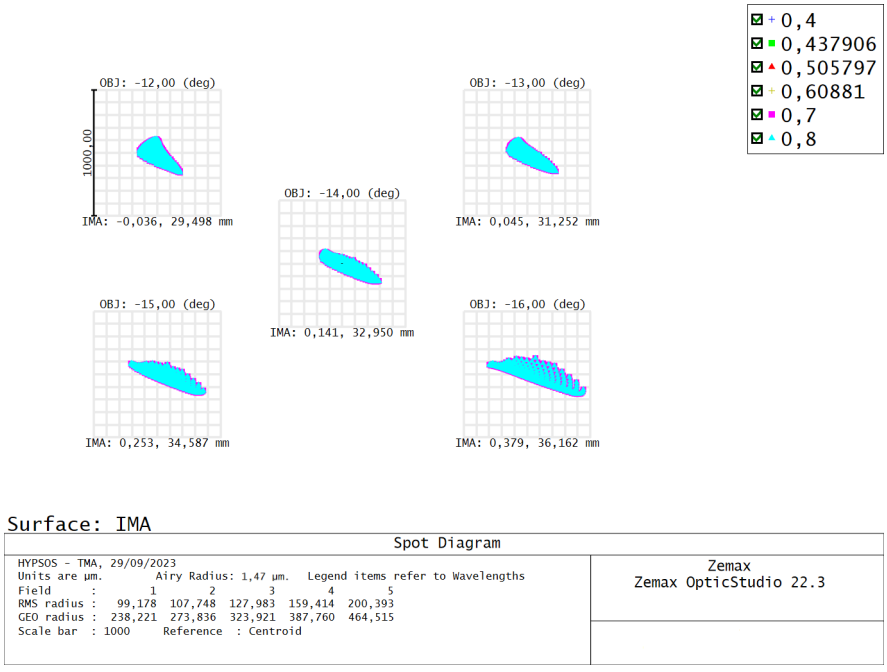

(b) Spot Diagram for the second Channel.

Figure 5.29: Spot Diagrams for both Channels, for the initial configuration. Both scale bars are set at 1000 μm.

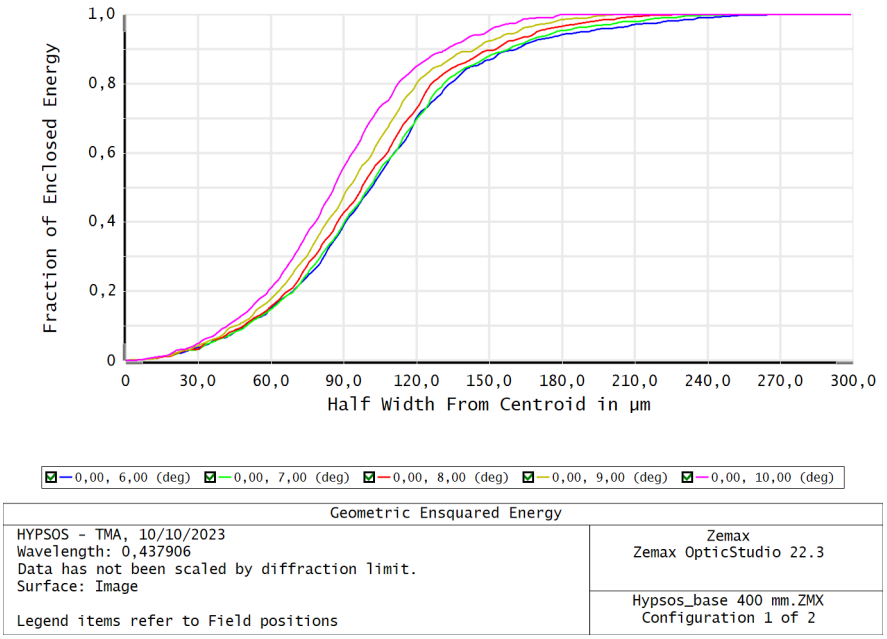

(a) Enclosed Energy Diagram for the first Channel. The half-distance from centroid is set at 300 μm.

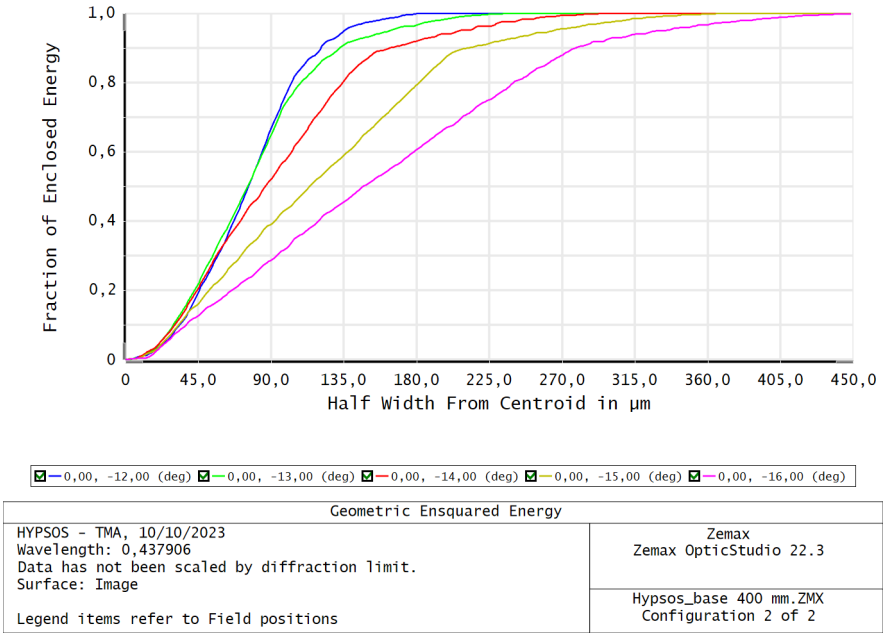

(b) Enclosed Energy Diagram for the second Channel. The half-distance from centroid is set at 450 μm.

Figure 5.30: Enclosed Energy Diagrams for both Channels, plotted for all the analysed field points at the same wavelength λ = 0.437906 μm, for the initial configuration.

5.2.2 Zernike freeform overlay integration

In the preliminary phases of optimisation, an identical process as outlined for VICESS has been followed, examining the FFD for primary aberrations and introducing the comparable Zernike term as a variable. However, this method did not prove to be as accurate, since the FFD was computed and displayed over a much wider range than the HYPSOS operating field, which is in fact vertical and limited by the slit.
Minimisation of aberrations is crucial along the vertical direction, therefore, the Spot Diagram is more useful to verify the effect of introducing various Zernike terms. The two Channels have been optimised independently, and the tilt and distance of the Focal Plane, parameters shared by both, were not introduced as variables.
This time the Zernike overlays have been normalized with the parent surfaces' radii, considering the two Channels separately. The final deformation of the surface of each Mirror, obtained from the optimization of each Channel, can then be considered just in the portion of the Mirror where each of the two light beams impacts.
For each Channel separately, Zernike terms were progressively introduced on all three Mirrors, beginning with Z_4. Only the terms that have significantly contributed to reducing the geometric dimensions of the spots in the Spot Diagrams have been retained.

Figure 5.31 displays the Spot Diagrams obtained for both Channels after adding Zernike terms Z_4, Z_5 and Z_8. The improvement is significant, as it is evident from the reduction of the box scale from 1000 μm to 100 μm for the first Channel and from 1000 μm to 200 μm for the second one. Nonetheless, the performance remains inadequate, as further supported from the Enclosed Energy Diagrams in Figure 5.32.

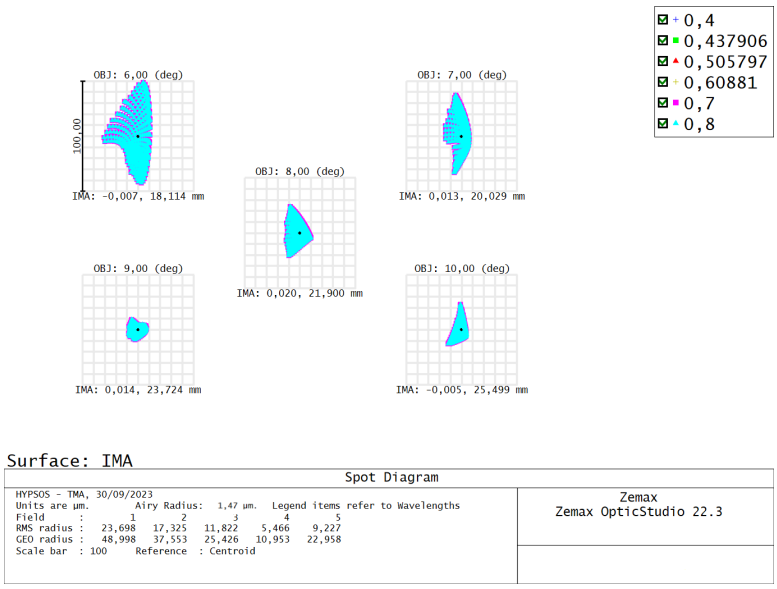

(a) Spot Diagram for the first Channel.

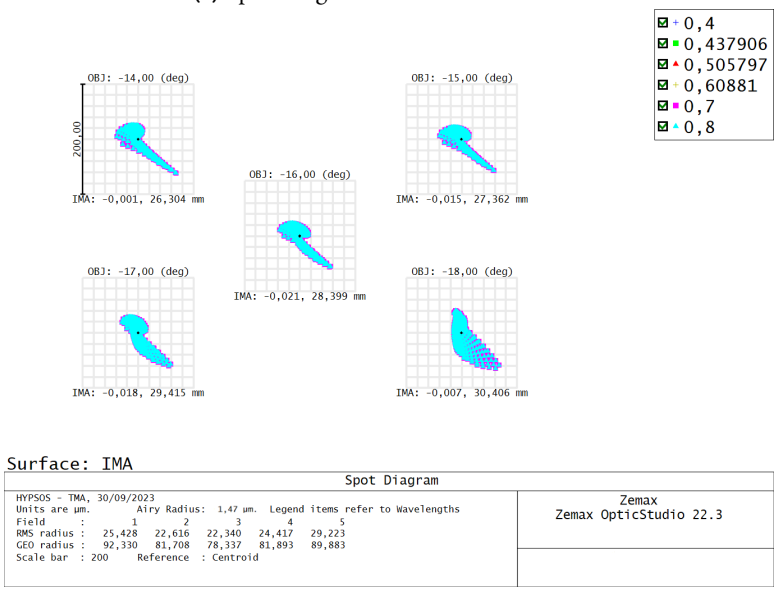

(b) Spot Diagram for the second Channel.

Figure 5.31: Spot Diagrams for both Channels, with Zernike terms up to Z_8. The scale bar is set at 100 μm for the first Channel and at 200 μm for the second.

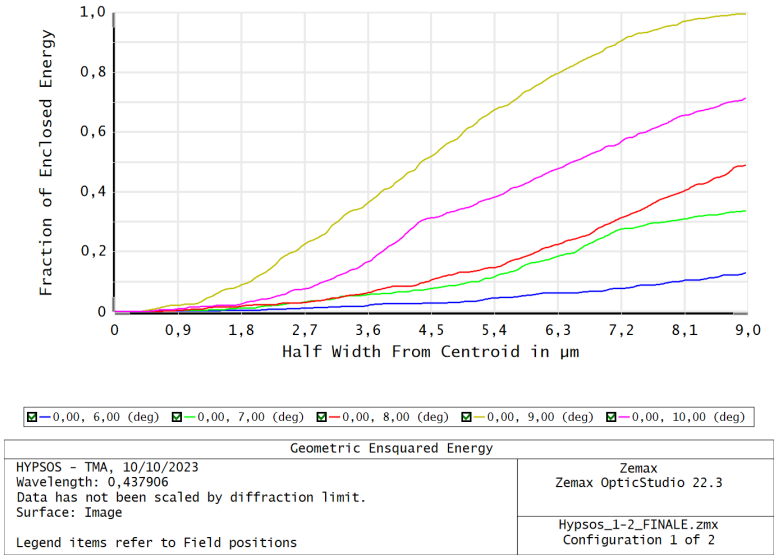

(a) Enclosed Energy Diagram for the first Channel.

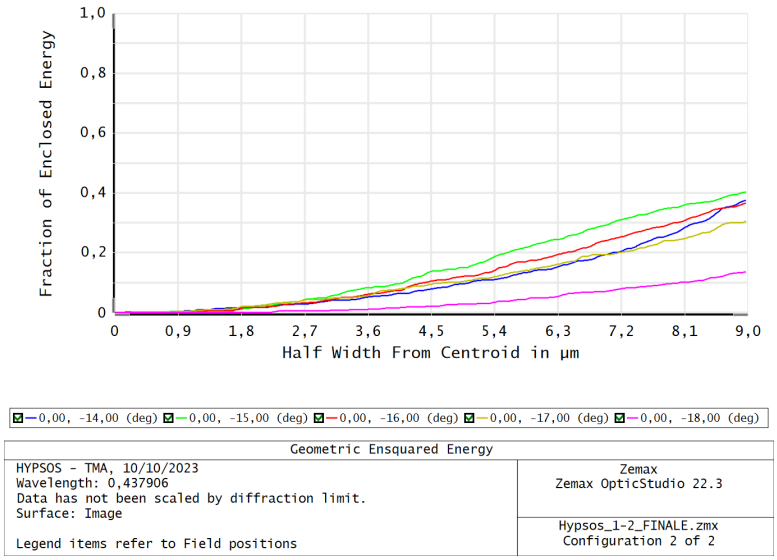

(b) Enclosed Energy Diagram for the second Channel.

Figure 5.32: Enclosed Energy Diagrams for both channels, with Zernike terms up to Z_8, plotted for all the analysed field points at the same wavelength $\lambda = 0.437906$ μm. The pixel side measures 18 μm.

As the previous terms were not sufficient, Zernike terms Z_9, Z_{11} and Z_{12} have been added; this time the improvement is not so drastic, but the box scale of the Spot Diagrams becomes the same for both Channels and the spots are overall visibly smaller, as shown in Figure 5.33.

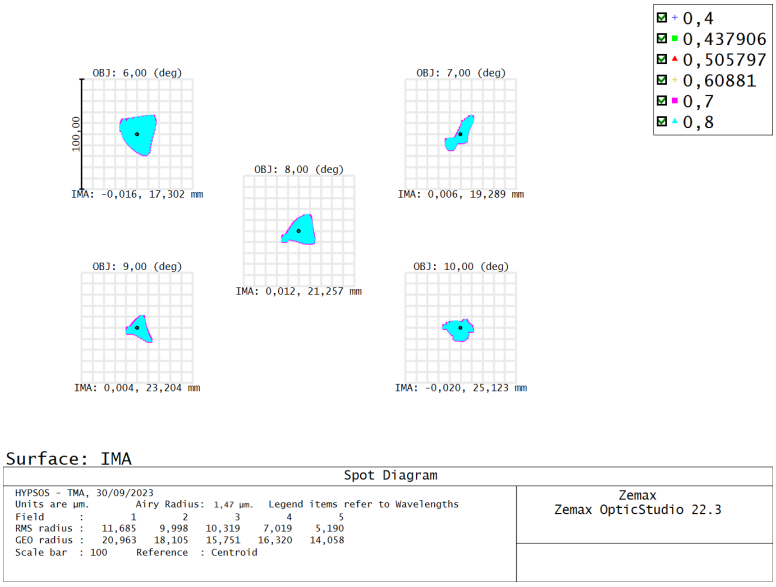

(a) Spot Diagram for the first Channel.

(b) Spot Diagram for the second Channel.

Figure 5.33: Spot Diagrams for both Channels, with Zernike terms up to Z_{12}. The scale bars are set at 100 μm.

The Enclosed Energy Diagrams, reported in Figure 5.34, also display a slight improvement, even though the curve associated with the (0.000,9.000) field momentarily worsens.

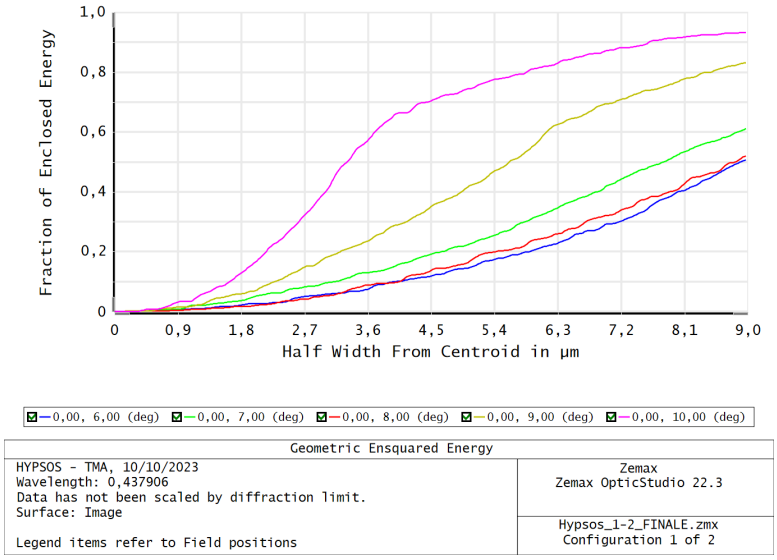

(a) Enclosed Energy Diagram for the first Channel.

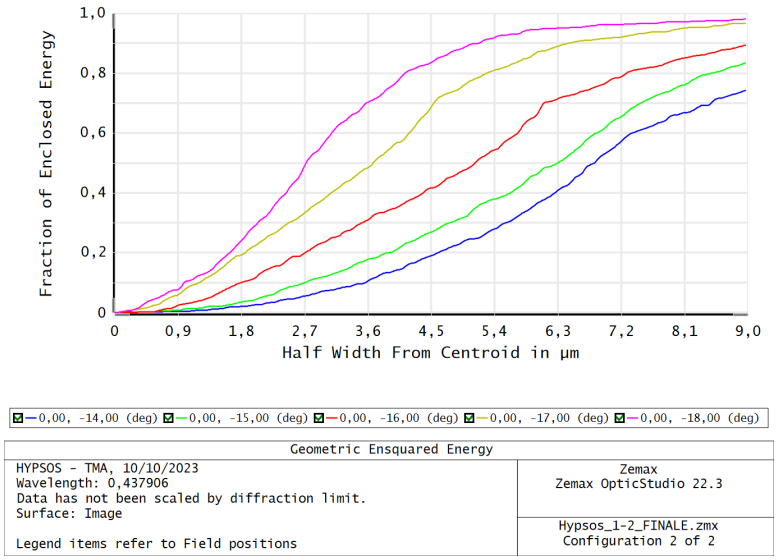

(b) Enclosed Energy Diagram for the second Channel.

Figure 5.34: Enclosed Energy Diagrams for both channels, with Zernike terms up to Z_{12}, plotted for all the analysed field points at the same wavelength λ = 0.437906 μm. The pixel side measures 18 μm.

Finally, Zernike terms Z_{15} and Z_{16} are introduced in the overlay. In Figure 5.35 it can be seen that now the box scale for both Channels is comparable with the pixel size, and the performance is acceptable, although still far from being diffraction-limited.

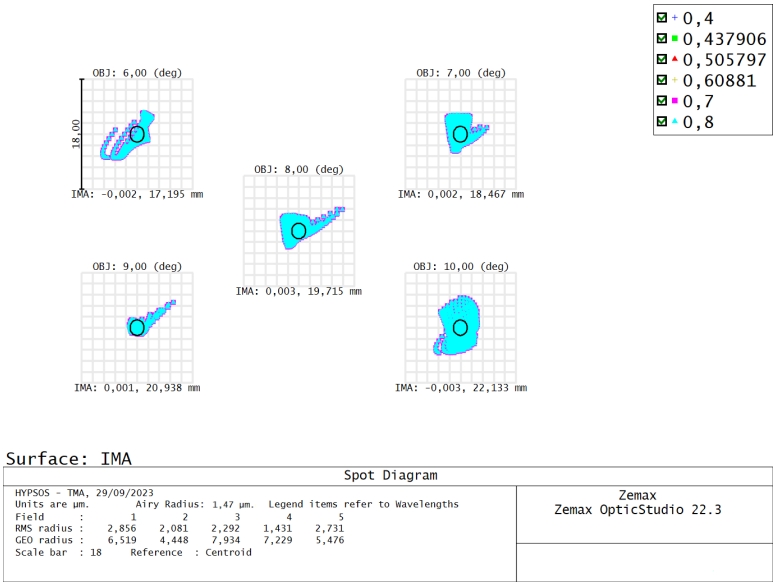

(a) Spot Diagram for the first Channel, Zernike terms up to Z_{16}.

(b) Spot Diagram for the second Channel, Zernike terms up to Z_{16}.

Figure 5.35: Spot Diagrams for both Channels, with Zernike terms up to Z_{16}. The scale bars are set at 18 μm.

Figure 5.36 shows how the Enclosed Energies reach the unit value within the pixel dimensions, indicating that now all the incident radiation can be collected by the sensors.

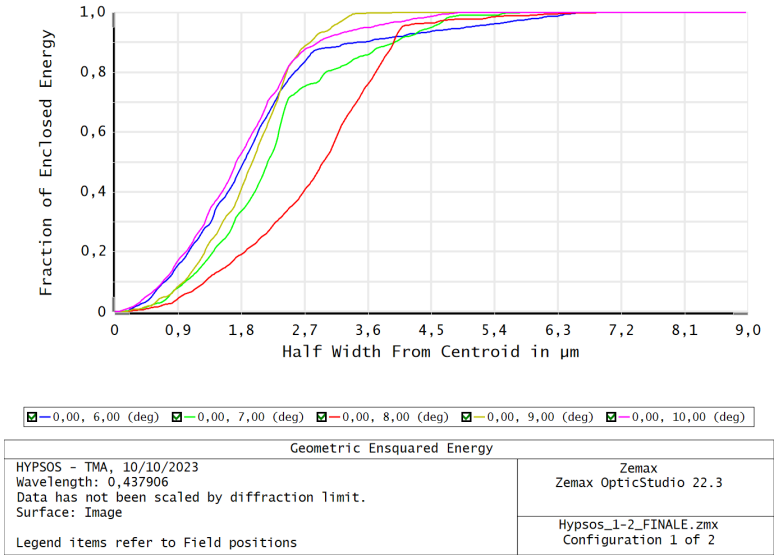

(a) Enclosed Energy Diagram for the first Channel.

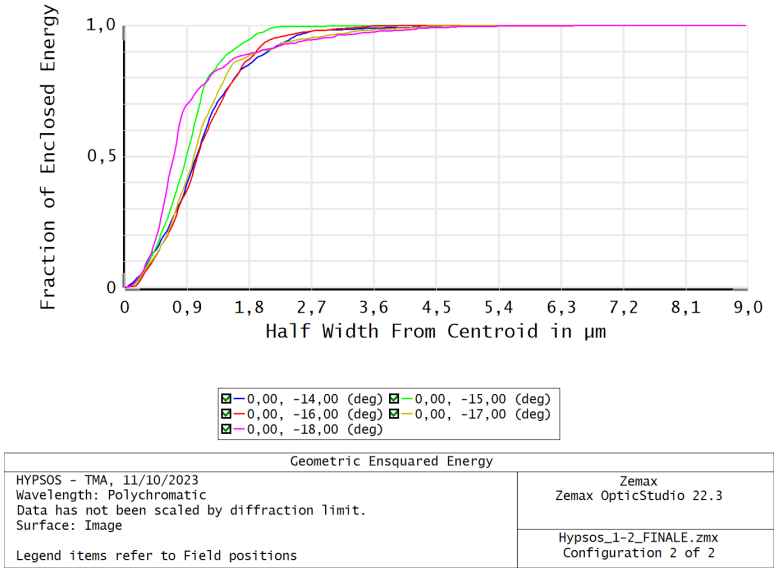

(b) Enclosed Energy Diagram for the second Channel.

Figure 5.36: Enclosed Energy Diagrams for both channels, with Zernike terms up to Z_{16}, plotted for all the analysed field points at the same wavelength $\lambda = 0.437906\ \mu$m. The pixel side measures 18 μm.

5.2.3 Final results and comparison

Also for the HYPSOS-like instrument, the Zernike coefficients describing the freeform overlay on each Mirror are summarised in Tables 5.10 and 5.11.

Surface	M1	M2	M3
$\mathbf{Z}_4$	$1.83223\,10^{-3}$	-0.053583	-0.129309
$\mathbf{Z}_5$	1.100551	0.601919	0.962830
$\mathbf{Z}_8$	1.877234	0.022833	0.058956
$\mathbf{Z}_9$	0.600141	$-8.057887\,10^{-3}$	-0.014553
$\mathbf{Z}_{11}$	-0.606735	$-9.836732\,10^{-3}$	-0.026932
$\mathbf{Z}_{12}$	-0.350398	-1.073994^{-3}	0.036865
$\mathbf{Z}_{15}$	0.368192	1.473756^{-3}	7.377085^{-3}
$\mathbf{Z}_{16}$	0.060923	-7.294116^{-5}	-2.360775^{-4}

Table 5.10: Zernike coefficients for the first Channel of the HYPSOS-like instrument.

Surface	M1	M2	M3
$\mathbf{Z}_4$	$2.552997\,10^{-3}$	-0.079820	0.308449
$\mathbf{Z}_5$	6.978433	0.653533	1.468072
$\mathbf{Z}_8$	5.920631	$2.459135\,10^{-3}$	-0.067187
$\mathbf{Z}_9$	2.273985	$-8.382542\,10^{-3}$	-0.015085
$\mathbf{Z}_{11}$	-0.394690	$4.185422\,10^{-4}$	0.019987
$\mathbf{Z}_{12}$	-0.600725	$-1.575528\,10^{-3}$	0.052362
$\mathbf{Z}_{15}$	1.394230	$4.456292\,10^{-4}$	$-3.670622\,10^{-3}$
$\mathbf{Z}_{16}$	0.262645	$-1.631501\,10^{-4}$	$-3.909159\,10^{-3}$

Table 5.11: Zernike coefficients for the second Channel of the HYPSOS-like instrument.

In this case, more coefficients have been necessary in order to improve the overall performance of the instrument, as the starting configuration was heavily aberrated. Since the focal

plane (or, equivalently, the entrance slit) was quite close to the TMA assembly, its distance from the folding mirror has been kept fixed during the optimization; the focal plane tilt about the x-axis has been kept fixed as well, as it is a parameter shared by both configuration, and its inclusion in the optimization process would have required the simultaneous engagement of variables from both configurations, in a process that would have been difficult to manage.

As previously done, the Spot Diagram for both Channels is reported in Figures 5.37 and 5.38. To further emphasise the improved performance achieved following the introduction of the freeform optics, the initial and final Spot Diagrams are presented in sequence. It can be seen that the scale bar goes from 1000 μm, for the initial configuration, to 18 μm, after the introduction of the Zernike overlay.

The Enclosed Energy Diagram is presented in Figures 5.39 and 5.40, for both Channels, before and after the introduction of the Zernike overlay. In this case, the attention must be focused on the substantial decrease of the half width from centroid, in the x-axis, necessary for the curves to reach the unit value. For the HYPSOS-like instrument, it can be seen that after the optimization of the Zernike overlay, the 100% of the PSF energy falls within the pixel dimension, which is 18 μm for both Channels.

Table 5.12 reports the resolution, obtained with an ideal sensor, as a function of the Airy Radius, according to Equation 5.1. In this case, only the second Channel is diffraction limited, as the RMS radii of the spots are comparable with the Airy radius. Therefore the analysis is significant just for this Channel, with the same premise that has been made for the VICESS-like instrument resolution. The second Channel would require a more complex computation of the resolution, as the RMS radii associated with the more extreme portions of the FoV differ from the Airy radius by a factor 1.5. In practice, this difference is not a problem if the sensor is assumed to have pixels with 18 μm sides, because the resolution limit then becomes 36 μm.

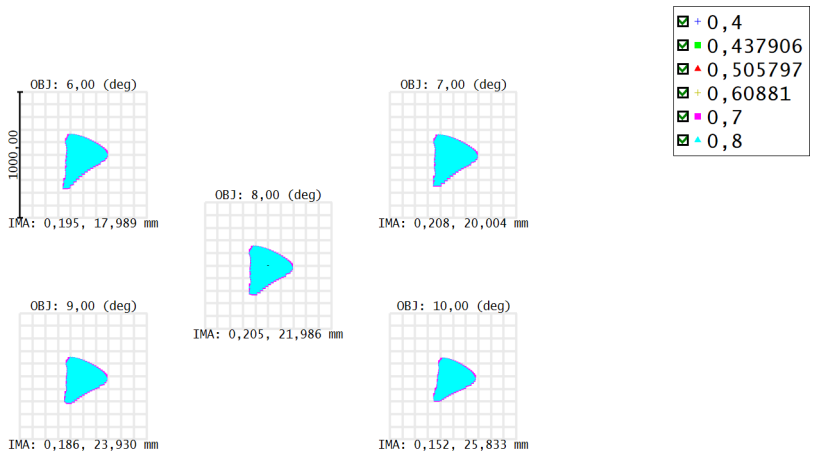

Surface: IMA

Spot Diagram	
HYPSOS - TMA, 29/09/2023 Units are µm. Airy Radius: 1,47 µm. Legend items refer to Wavelengths Field : 1 2 3 4 5 RMS radius : 126,502 123,657 119,105 112,821 105,701 GEO radius : 286,290 264,973 243,900 227,052 220,346 Scale bar : 1000 Reference : Centroid	Zemax Zemax OpticStudio 22.3

(a) Spot Diagram for the first Channel before introducing the Zernike polynomial terms to the Mirrors. The scale bar is set at 1000 μm.

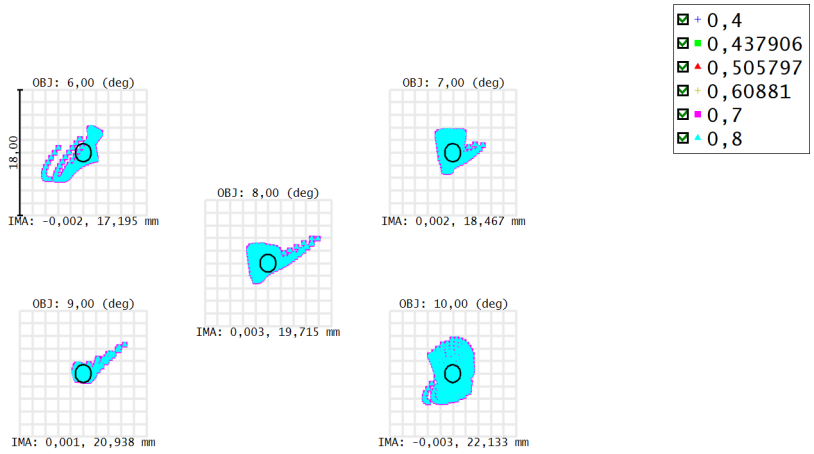

Surface: IMA

Spot Diagram	
HYPSOS - TMA, 29/09/2023 Units are µm. Airy Radius: 1,47 µm. Legend items refer to Wavelengths Field : 1 2 3 4 5 RMS radius : 2,856 2,081 2,292 1,431 2,731 GEO radius : 6,519 4,448 7,934 7,229 5,476 Scale bar : 18 Reference : Centroid	Zemax Zemax OpticStudio 22.3

(b) Spot Diagram for the first Channel after introducing the Zernike polynomial terms to the Mirrors.The scale bar is set at 18 μm.

Figure 5.37: Spot Diagrams for the first Channel, displayed for five field points and a wavelength range from 0.4000 to 0.8000 μm.

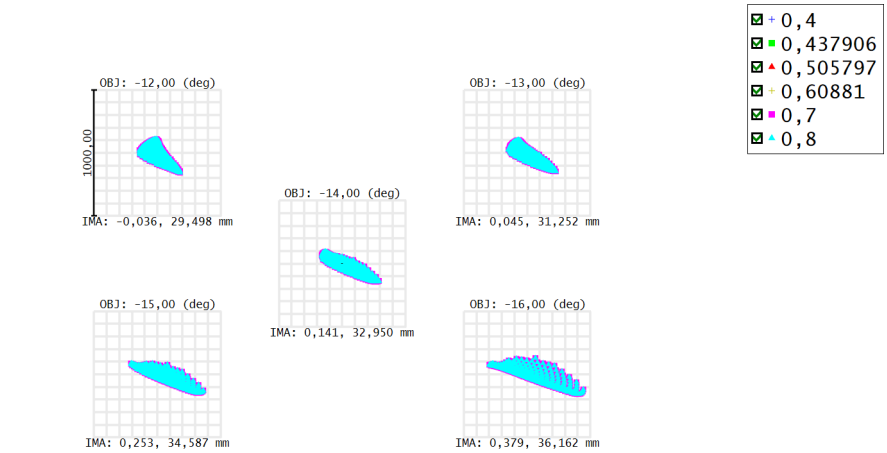

Surface: IMA

Spot Diagram	
HYPSOS - TMA, 29/09/2023 Units are µm. Airy Radius: 1,47 µm. Legend items refer to Wavelengths Field : 1 2 3 4 5 RMS radius : 99,178 107,748 127,983 159,414 200,393 GEO radius : 238,221 273,836 323,921 387,760 464,515 Scale bar : 1000 Reference : Centroid	Zemax Zemax OpticStudio 22.3

(a) Spot Diagram for the second Channel before introducing the Zernike polynomial terms to the Mirrors. The scale bar is set at 1000 μm.

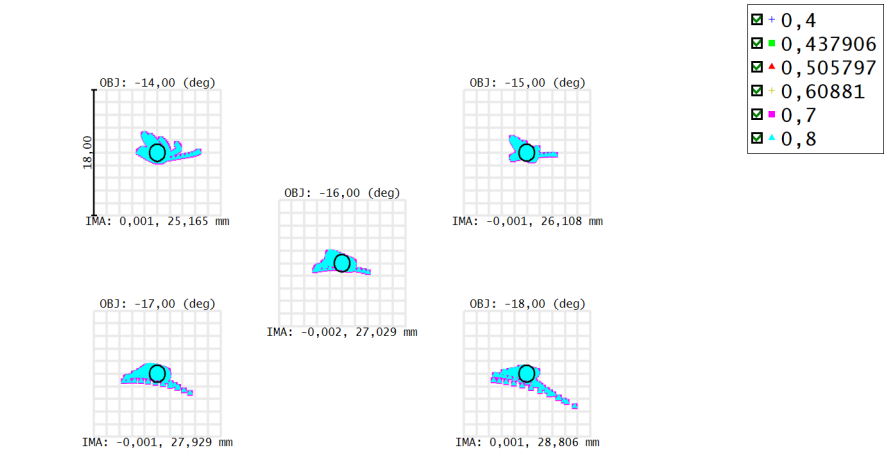

Surface: IMA

Spot Diagram	
HYPSOS - TMA, 29/09/2023 Units are µm. Airy Radius: 1,47 µm. Legend items refer to Wavelengths Field : 1 2 3 4 5 RMS radius : 1,568 1,254 1,462 1,511 1,567 GEO radius : 5,894 4,072 3,975 5,417 8,270 Scale bar : 18 Reference : Centroid	Zemax Zemax OpticStudio 22.3

(b) Spot Diagram for the second Channel after introducing the Zernike polynomial terms to the Mirrors. The scale bar is set at 18 μm.

Figure 5.38: Matrix Spot Diagrams for the second Channel, displayed for five field points and a wavelength range from 0.400 to 0.800 μm.

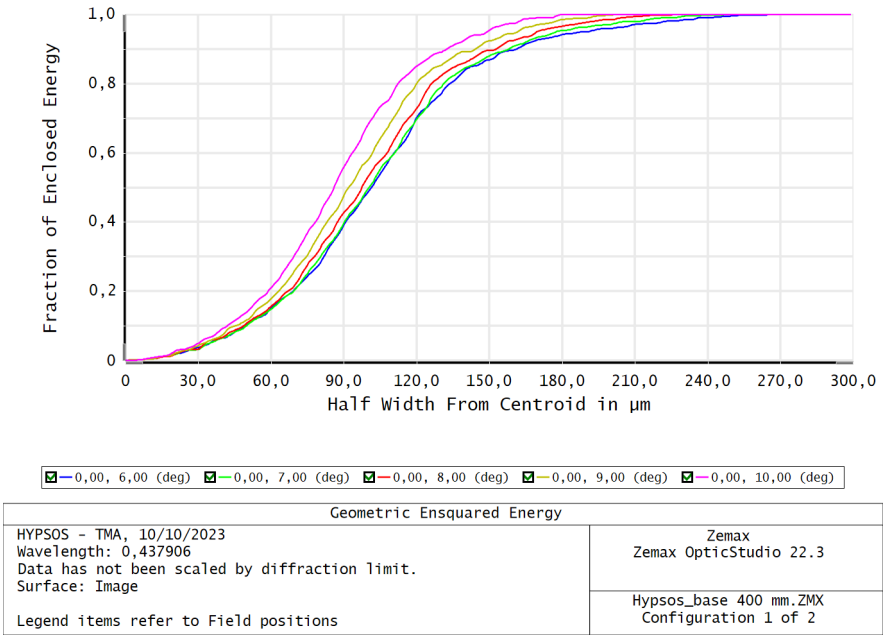

(a) Ensquared Energy Diagram for the first Channel, before adding the Zernike overlay.

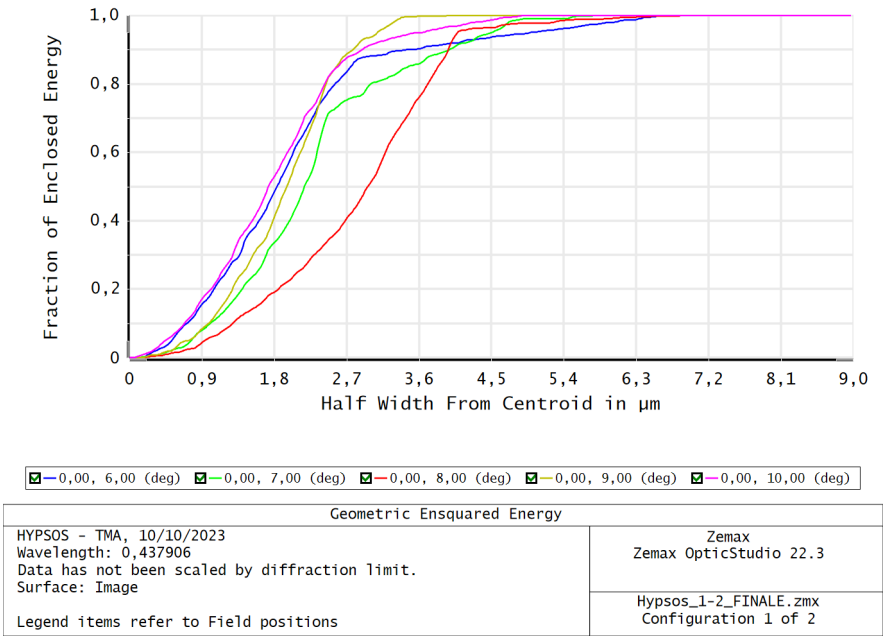

(b) Ensquared Energy Diagram for the first Channel after adding the Zernike overlay.

Figure 5.39: Ensquared Energy Diagrams for the first Channel, plotted for all the analysed field points at the same wavelength $\lambda = 0.437906\ \mu$m.

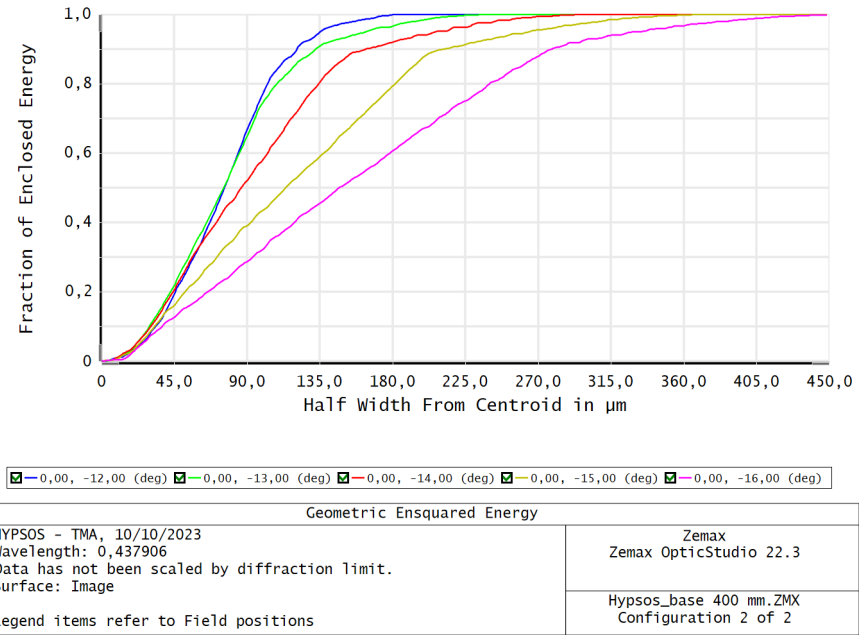

(a) Ensquared Energy Diagram for the second Channel, before adding the Zernike overlay.

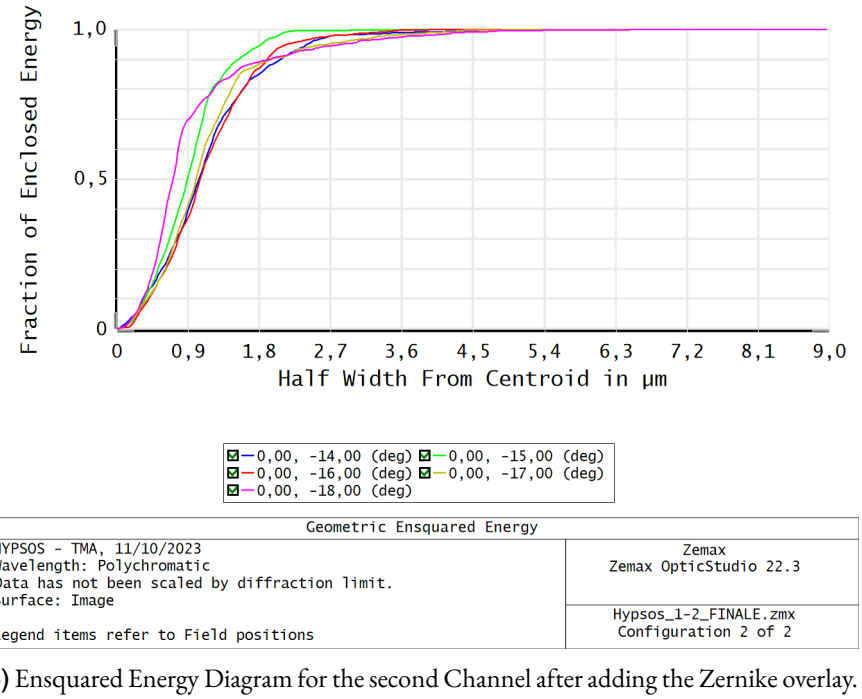

(b) Ensquared Energy Diagram for the second Channel after adding the Zernike overlay.

Figure 5.40: Ensquared Energy Diagrams for the second Channel, plotted for all the analysed field points at the same wavelength $\lambda = 0.437906$ μm.

Channel 2	Wavelength (μm)	Airy Radius (μm)	Resolution Δx (m/pixel)
-	0.4000	1.4640	1.2200
-	0.4379	1.6027	1.3356
-	0.5058	1.8512	1.5427
-	0.6088	2.2282	1.8568
-	0.7000	2.5620	2.1350
-	0.8000	2.9280	2.4400

Table 5.12: Airy disk radius and resolution as function of wavelength, for Channel 1 and Channel 2, with a focal length of 120 mm and a distance from the object of 100 km.

6

Conclusions

In this thesis work, the objective has been to showcase how the implementation of freeform optics in a given optical system can enable to meet stricter requirements than conventional optics, ultimately leading to excellent performances.

Part of the work has been devoted to the development of a camera capable of operating in both the visible and infrared wavelengths, starting from the VICESS camera layout. The Nodal Aberration Theory applied to freeform surfaces has constituted the backbone of the design, allowing the gradual introduction of Zernike coefficients suitable for correcting specific aberrations. This made it possible to increase the focal length and aperture of the system compared to the original design, allowing more light to pass through the instrument. The performance of the system has been temporarily reduced, but after optimising the freeform overlay, the system returned to being diffraction-limited like the original, but with the advantage of being able to accommodate a greater flux of photons.

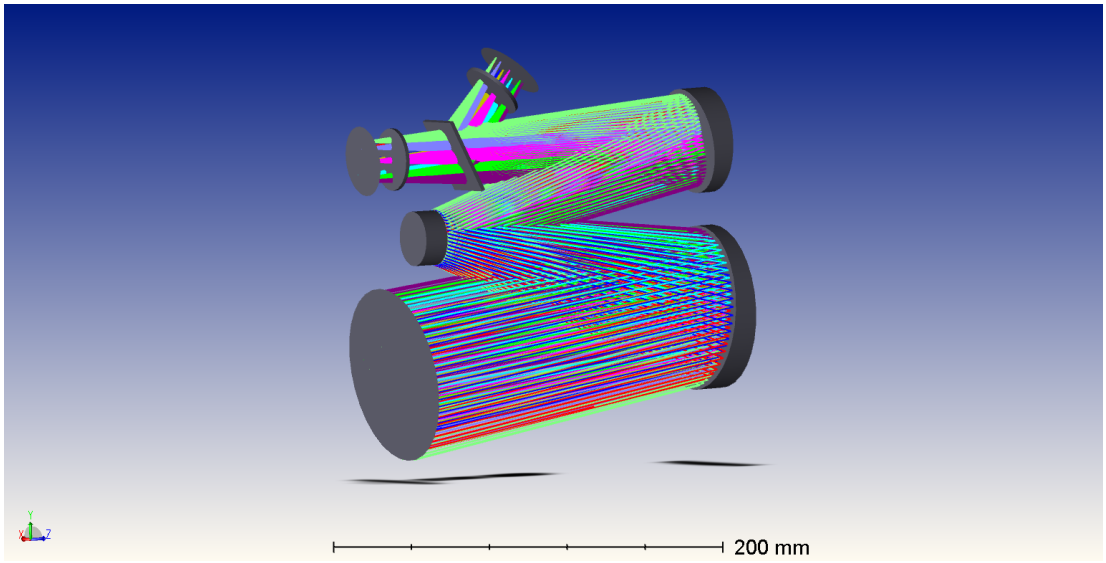

Figure 6.1: Shaded model of the VICESS-like instrument.

The second part of the work consisted in adapting the HYPSOS hyperspectral stereo-imaging system to new, more stringent specifications, rendering it suitable for a lunar mapping mission. The initial design included two entrance folding mirrors to collect the necessary light for the two stereo-camera channels, plus two Schmidt-Pechan field rotators to align both images on the same slit. In the ultimate design, the focal length was decreased and the aperture was increased. Additionally, the two Schmidt-Pechan prisms and one entrance folding mirror were removed, resulting in a significantly simpler, lighter and more compact, mirror-only design, without actually affecting the instrument's ability to focus the two beams in the same slit.

Again, as a result of the design changes, the performance deteriorated with respect to the original one, but the insertion of a freeform overlay in all the three mirrors allowed a return to optimum performance, albeit not at the diffraction limit.

In any case, it can be stated that the use of freeform optics yielded positive performance results for both instruments, which would have otherwise been impossible to achieve.

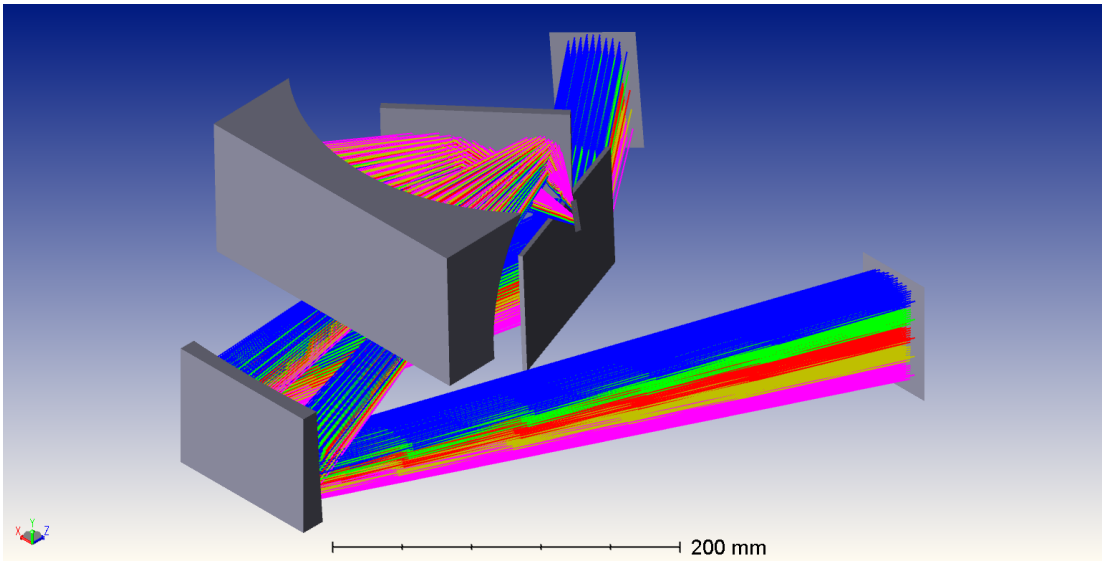

Figure 6.2: Shaded model of the HYPSOS-like instrument.

7

Appendix

7.1 Zernike polynomials: relationship with Seidel aberrations

The performance of an optical system can be characterized by the deformation of the wavefront emerging from the exit pupil relative to its reference sphere, that is, wavefront aberration. The wavefront aberration for a rotationally symmetric system can be expanded by a set of power series in the four variables (ρ, θ) (polar coordinates of the exit pupil) and $(r, \phi{=}0)$ (polar coordinates of an image point on the image plane) as:

$$\begin{aligned} W(\rho,\theta) &= \sum_{l,n,m} W_{lnm} r^l \rho^n (\cos\theta)^m = \\ &= W_{111} r\rho\cos\theta + W_{020}\rho^2 + W_{040}\rho^4 + \\ &+ W_{131} r\rho^3\cos\theta + W_{222} r^2\rho^2\cos\theta^2 + \\ &+ W_{220} r^2\rho^2 + W_{311}\rho\cos\theta + \ldots \end{aligned} \tag{7.1}$$

where l is a positive integer describing the dependence of a given term upon the distance of the image point from the axis; n and m are two positive integers determining the type of aberration. The first two terms in Equation 7.1 represent the transverse and longitudinal focal shifts, respectively. The remaining aberration terms constrained by the relation $l + n = 4$ are the well known primary or Seidel aberrations, which include the five monochromatic aberrations of spherical aberration (W_{040}), coma (W_{131}), astigmatism (W_{222}), field curvature (W_{220}), and distortion (W_{311}). These aberrations are sometimes called third-order aberrations when referring to ray aberration, which can be obtained as the derivative of wavefront aberration. For a fixed image point,r is a constant and can be absorbed into the coefficients. Assuming the relative aperture and the size of the field to be such that higher-order terms can be ignored, the expression of the wavefront aberration in Equation 7.1 reduces to:

$$\begin{aligned} W(\rho,\theta) = {} & W_{11}\rho\cos\theta + W_{20}\rho^2 + W_{40}\rho^4 + \\ & + W_{31}\rho^3\cos\theta + W_{22}\rho^2\cos\theta^2 + W_{220}r\rho^2. \end{aligned} \tag{7.2}$$

The wavefront aberration for a rotationally symmetric system can also be expanded by a set of Zernike series instead of power series. Assuming the first nine terms of Zernike circle polynomials are used for the expansion, the wavefront aberration can be written as:

$$\begin{aligned} W(\rho,\theta) = \sum_{j=0}^{8} a_j Z_j((\rho,\theta) = {} & a_0 + a_1\rho\cos\theta + a_2\rho\sin\theta + \\ & + a_3(2\rho^2 - 1) + + a_4\rho^2\cos 2\theta + a_5\rho^2\sin 2\theta + \\ & + a_6(3\rho^3 - 2\rho)\cos\theta + a_7(3\rho^3 - 2\rho)\sin\theta + \\ & + a_8(6\rho^4 - 6\rho^2 + 1). \end{aligned} \tag{7.3}$$

Equation 7.3 can be further rearranged as:

$$\begin{aligned} W(\rho,\theta) = {} & a_p + a_t\rho\cos(\theta - \phi_t) + a_d\rho^2 + a_a\rho^2\cos(\theta - \phi_a)^2 + \\ & + a_c\rho^3\cos(\theta - \phi_c) + a_s\rho^4. \end{aligned} \tag{7.4}$$

The expressions for the coefficients and phase angles are tabulated in Table 7.1:

Aberration	Coefficients	Phase angle
Piston	$a_p = a_0 - a_3 + a_8$	-
Tilt	$a_t = \sqrt{(a_1 - 2a_6)^2 + (a_2 - 2a_7)^2}$	$\phi_t = \text{atan}\,\frac{(a_2-2a_7)}{(a_1-2a_6)}$
Defocus	$a_d = (2a_3 - 6a_8 \pm \sqrt{a_4^2 + a_5^2})$	-
Astigmatism	$a_a = \pm\sqrt{a_4^2 + a_5^2}$	$\phi_a = \frac{1}{2}\,\text{atan}\,\frac{a_5}{a_4}$
Coma	$a_c = 3\sqrt{a_6^2 + a_7^2}$	$\phi_a = \text{atan}\,\frac{a_7}{a_6}$
Spherical	$a_s = 6a_8$	-

Table 7.1: Relationship between Zernike coefficients and Seidel aberrations [8].

The expansion in Equation 7.3 has a similar form to Equation 7.1, indicating that the coefficients of Seidel aberrations can be converted from Zernike expansion coefficients.

7.2 Zernike polynomials: wavefront fitting

A wavefront function W, defined over a unit circle, can be represented by the linear combination of finite terms of Zernike circle polynomials as [8]:

$$W(R\rho,\theta) = \sum_{j=0}^{J} a_j Z_j(\rho,\theta), \tag{7.5}$$

where R is the radius of the pupil, $0 \leq \rho \leq 1$, J is the maximum number of terms of the polynomials, a_j is the expansion coefficients, and Z_j is the j^{th} Zernike polynomial term. The equation can be equivalently expressed in Cartesian coordinates as:

$$W(x,y) = \sum_{j=0}^{J} a_j Z_j(x,y). \tag{7.6}$$

Written in discrete and matrix forms, Equation 7.6 becomes:

$$\mathbf{A}\vec{a} = \mathbf{W}, \tag{7.7}$$

where:

$$\mathbf{A} = \begin{bmatrix} Z_1(x_1,y_1) & Z_2(x_1,y_1) & \dots & Z_J(x_1,y_1) \\ Z_1(x_2,y_2) & Z_2(x_2,y_2) & \dots & Z_J(x_2,y_2) \\ \dots & \dots & \dots & \dots \\ Z_1(x_K,y_K) & Z_2(x_K,y_K) & \dots & Z_J(x_K,y_K) \end{bmatrix} \vec{a} = \begin{bmatrix} a_1 \\ a_2 \\ \dots \\ a_J \end{bmatrix} \mathbf{W} = \begin{bmatrix} W(x_1,y_1) \\ W(x_2,y_2) \\ \dots W(x_K,y_K) \end{bmatrix}. \tag{7.8}$$

K is the total number of data points within the unit circle. The vector solution, $\vec{a}$, can be obtained with the operations of matrix transposition and matrix inversion, as follows:

$$\mathbf{A}^T\mathbf{A}\vec{a} = \mathbf{A}^T\mathbf{W}\vec{a} = (\mathbf{A}^T\mathbf{A})^{-1}\mathbf{A}^T\mathbf{W}. \tag{7.9}$$

The Zernike-based wavefront fitting has several useful properties. First, the truncation of the expansion of a wavefront does not change the expansion coefficients, as they are independent from each other:

$$a_j = \frac{1}{\pi}\int_0^{2\pi}\int_0^1 W(\rho,\theta)Z_j\rho d\rho d\theta. \tag{7.10}$$

Second, all Zernike terms, except piston, have a mean value of zero and, therefore, the mean value of a wavefront equals the piston coefficient:

$$\bar{W}(\rho,\theta) = \frac{1}{\pi}\int_\Sigma W(\rho,\theta)d\rho d\theta = a_0. \tag{7.11}$$

Third, wavefront variance equals the sum of the square of each expansion coefficient, ex-

cluding the piston one:

$$\sigma^2 = \frac{1}{\pi}\int_0^{2\pi}\int_0^1 [W(\rho,\theta) - \bar{W}(\rho,\theta)]^2 d\rho d\theta = \\ = \bar{W^2} - (\bar{W})^2 = \sum_{j=1}^{\infty} a_j^2. \tag{7.12}$$

7.3 Tangential, sagittal and medial focal surfaces

Considering an optical system lens, the plane that contains the optical axis is called *meridional* or *tangential plane*. The plane perpendicular to the tangential plane is, instead, called *sagittal plane*. If an optical system is affected by the aberration of astigmatism, when an object point lies at a certain distance from the optical axis, the projection of the rays in the tangential and sagittal planes is different, therefore also the focal lengths in these two focal planes are different. If initially the section of the beam is circular, then it becomes elliptical, with the semi-major axis in the sagittal plane until it degenerates in a segment at the tangential focus. Then, the beam opens again, passing through the least confusion circle (or medial focus), and then again becomes a segment in the sagittal focus, perpendicular to the tangential one, as can be seen in Figure 7.1.

Astigmatism, however, is an aberration that intrinsically implies also a field curvature, therefore three focal surfaces can be defined, which are typically not plane: the tangential focal surface, where the tangential rays are focused, the sagittal focal surface, where the sagittal rays are focused, and the medial focal surface, where the circles of least confusion are located and which often represents the best compromise image location in an astigmatic system.

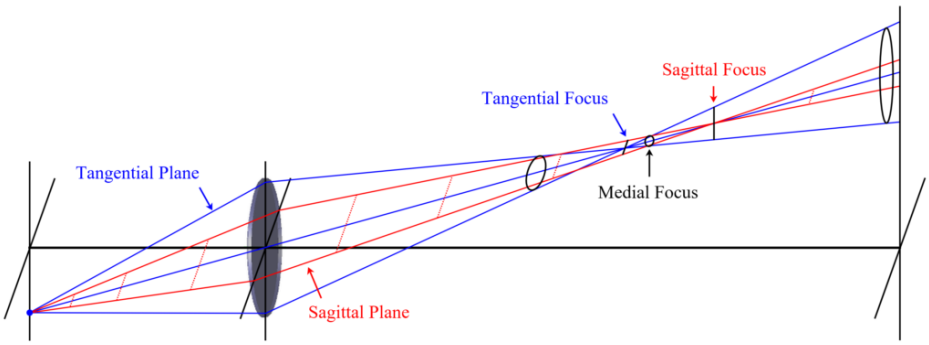

Figure 7.1: Tangential, sagittal and medial foci in an astigmatic optical lens [12].

References

[1] F. E. DeMeo and B. Carry, "Solar System evolution from compositional mapping of the asteroid belt," *Nature*, vol. 505, no. 7485, pp. 629–634, 2014.

[2] S. Dunst and P. Tomancak, "Imaging flies by fluorescence microscopy: principles, technologies, and applications," *Genetics*, vol. 211, no. 1, pp. 15–34, 2019.

[3] J. Sasián, *Introduction to Aberrations in Optical Imaging Systems*. Cambridge University Press, 2012, ch. Ray aberrations.

[4] H. González-Núñez, C. Vázquez-Vázquez, E. L. Lago, M. D. Mouriz, C. Montero-Orille, X. Prieto-Blanco, and R. De la Fuente, "Design, calibration and assembly of an Offner imaging spectrometer," in *Journal of Physics: Conference Series*, vol. 274, no. 1. IOP Publishing, 2011, p. 012106.

[5] G. Naletto, L. Agostini, G. Cremonese, E. Desirò, I. Dorgnach, C. Doria, M. Faccioni, R. La Grassa, F. Lazzarotto, L. Lessio *et al.*, "In-lab characterization of HYPSOS, a novel stereo hyperspectral observing system: first results," in *International Conference on Space Optics—ICSO 2022*, vol. 12777. SPIE, 2023, pp. 2292–2305.

[6] "What is a freeform optic?" http://centerfreeformoptics.org/what-is-freeform-optics/.

[7] A. Broemel, U. Lippmann, and H. Gross, "Freeform surface descriptions. Part I: Mathematical representations," *Advanced Optical Technologies*, vol. 6, no. 5, pp. 327–336, 2017.

[8] K. Niu and C. Tian, "Zernike polynomials and their applications," *Journal of Optics*, vol. 24, no. 12, p. 123001, nov 2022.

[9] K. Fuerschbach, J. P. Rolland, and K. P. Thompson, "Theory of aberration fields for general optical systems with freeform surfaces," *Optics express*, vol. 22, no. 22, pp. 26 585–26 606, 2014.

[10] K. Thompson, "Description of the third-order optical aberrations of near-circular pupil optical systems without symmetry," *J. Opt. Soc. Am. A*, vol. 22, no. 7, pp. 1389–1401, Jul 2005.

[11] K. Fuerschbach, *Freeform, φ-polynomial optical surfaces: optical design, fabrication and assembly*. University of Rochester, 2014.

[12] "Optical Aberrations," https://www.eckop.com/resources/optics/aberrations/.

[13] S. Magrin, "SINEO: Spectroscopic Investigation of Near Earth Objects," Ph.D. dissertation, University of Padova, 2006.

[14] "Why we explore," https://www.nasa.gov/exploration/whyweexplore/why_we_explore_main.html.

[15] L. G. Fiocco, "VIS-IR camera for the exploration of the solar system (VICESS)," Padova, September 2022.

[16] A. Cellino and A. Dell'Oro, "Minor bodies: small actors in Solar System's history," *Memorie della Societa Astronomica Italiana, v. 82, p. 300 (2011)*, vol. 82, p. 300, 2011.

[17] W. F.Bottke, "Understanding the Near-Earth object population: the 2004 perspective," *Comet/Asteroid Impacts and Human Society: An Interdisciplinary Approach*, pp. 175–187, 2007.

[18] "What is a Lagrange point?" https://science.nasa.gov/resource/what-is-a-lagrange-point/.

[19] "Comets," $https://solarsystem.nasa.gov/asteroids-comets-and-meteors/comets/overview/?page=0&per_page=40&order=name+asc&search=&condition_1=102%3Aparent_id&condition_2=comet%3Abody_type%3Ailike$.

[20] D. P. Cruikshank, "Triton, Pluto, Centaurs, and trans-neptunian bodies," *Space science reviews*, vol. 116, pp. 421–439, 2005.

[21] M. Nolan, P. Abell, E. Asphaug, C. D. d'Aubigny, T. Becker, M. Brozovic, M. Busch, R. Binzel, S. Chesley, R. T. Daly *et al.*, "Near-Earth Objects," *Bulletin of the AAS*, vol. 53, no. 4, 2021.

[22] "Different types of asteroids," https://astronomysource.com/different-types-of-asteroids/.

[23] N. Bhandari, "Planetary exploration: Scientific importance and future prospects," *Curr Sci*, vol. 94, 01 2008.

[24] H. E. Newsom and S. Ross Taylor, "Geochemical implications of the formation of the moon by a single giant impact," *Nature*, vol. 338, no. 6210, pp. 29–34, 1989.

[25] S. C. Solomon, "Mercury: the enigmatic innermost planet," *Earth and Planetary Science Letters*, vol. 216, no. 4, pp. 441–455, 2003.

[26] A. T. Basilevsky and J. W. Head, "The surface of Venus," *Reports on Progress in Physics*, vol. 66, no. 10, p. 1699, sep 2003.

[27] N. Mangold, D. Baratoux, O. Witasse, T. Encrenaz, and C. Sotin, "Mars: a small terrestrial planet," *The Astronomy and Astrophysics Review*, vol. 24, pp. 1–107, 2016.

[28] V. A. Krasnopolsky, J. P. Maillard, and T. C. Owen, "Detection of methane in the martian atmosphere: evidence for life?" *Icarus*, vol. 172, no. 2, pp. 537–547, 2004.

[29] G. D'Angelo and J. J. Lissauer, "Formation of giant planets," *arXiv preprint arXiv:1806.05649*, 2018.

[30] S. K. Atreya, M. H. Hofstadter, J. H. In, O. Mousis, K. Reh, and M. H. Wong, "Deep atmosphere composition, structure, origin, and exploration, with particular focus on critical in situ science at the icy giants," *Space Science Reviews*, vol. 216, pp. 1–31, 2020.

[31] J. Ye, L. Chen, X. Li, Q. Yuan, and Z. Gao, "Review of optical freeform surface representation technique and its application," *Optical Engineering*, vol. 56, no. 11, pp. 110 901–110 901, 2017.

[32] S. Kumar, Z. Tong, and X. Jiang, "Advances in the design and manufacturing of novel freeform optics," *International Journal of Extreme Manufacturing*, vol. 4, no. 3, p. 032004, jul 2022.

[33] F. Duerr and H. Thienpont, "Freeform imaging systems: Fermat's principle unlocks "first time right" design," *Light: Science & Applications*, vol. 10, no. 1, p. 95, 2021.

[34] M. Oleszko, "Analysis of freeform optical systems based on the decomposition of the total wave aberration into Zernike surface contributions," Ph.D. dissertation, Friedrich-Schiller-Universität, Jena, 2019.

[35] H. Hopkins, *Wave Theory of Aberrations*, ser. Monographs on the physics and chemistry of materials. Clarendon Press, 1950.

[36] . Buchroeder, Richard Alfred, "Tilted component optical systems," Ph.D. dissertation, The University of Arizona, 1976.

[37] K. P. Thompson, "Aberration fields in tilted and decentered optical systems," Ph.D. dissertation, The University of Arizona, 1980.

[38] J. Rogers, "Techniques and tools for obtaining symmetrical performance from tilted-component systems," *Optical Engineering - OPT ENG*, vol. 39, pp. 1776–1787, 07 2000.

[39] A. Bauer, E. M. Schiesser, and J. P. Rolland, "Starting geometry creation and design method for freeform optics," *Nature communications*, vol. 9, no. 1, p. 1756, 2018.

[40] C. Perron and B. Zanda, "Meteorites: samples of NEOs in the laboratory," *Comptes Rendus Physique*, vol. 6, no. 3, pp. 345–360, 2005.

Acknowledgments

At this moment, so special to me, it is not easy to condense into a few lines the thoughts and emotions, the feeling of years of life converging in a moment that I have been imagining since the first day of class at University.
I express my gratitude to Professor Giampiero Naletto and Dr. Maurizio Pajola for their kind-heartedness, helpfulness and patience throughout this work's various stages. Thank you for providing me with an opportunity to test myself.
I would like to express my sincere gratitude to my mother, father and Silvia for their unwavering support and belief in me. I extend my heartfelt thanks to my grandparents, who celebrate with me both in heaven and on Earth, and to my aunts and uncles, who are always a compass. I am grateful to my younger cousins, who still want to play with me, and to Arianna for being part of my life.
I think about the friendships forged with my 'Space Girls', Carmen and Samantha, Francesca and my fellow University companions. I am so pleased to have met you and to have walked this incredible, challenging yet gratifying journey with you.
Lastly, I would like to express my gratitude to Alessandro: there is no greater joy than reaching this significant accomplishment together.

In questo momento, così speciale per me, non è semplice condensare in poche righe i pensieri e le emozioni, la sensazione di anni di vita che convergono in un momento che immagino dal primo giorno di lezione all'Università.
Desidero ringraziare il Professor Giampiero Naletto e il Dottor Maurizio Pajola, per la gentilezza, la disponibilità e la pazienza che hanno avuto nel guidarmi in tutte le fasi di questo lavoro. Vi ringrazio per avermi dato la possibilità di mettermi alla prova.

Ringrazio di cuore mamma, papà e Silvia, per il supporto incondizionato e per non aver mai dubitato di me. Ringrazio i nonni, che festeggiano con me dal cielo e sulla Terra, ringrazio gli zii che sono sempre una bussola. Ringrazio i miei cuginetti, che ancora vogliono giocare con me, e Arianna per essere nella mia vita. Spero di avervi resi orgogliosi.
Penso alle mie "Space Girls", Carmen e Samantha, a Francesca e a tutti gli amici dell'Università. Sono così felice di avervi conosciuto e di aver condiviso con voi questo meraviglioso percorso, faticoso ma appagante.
Ringrazio, infine, Alessandro: la gioia più grande è essere arrivati a questo traguardo insieme.